



# *23rd Annual Student Design Competition*

## *Graduate Category*



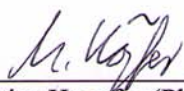
**Daniel Guggenheim School of Aerospace Engineering  
Georgia Institute of Technology  
Atlanta, Georgia 30332**

## Acknowledgements

We would like to recognize and thank the following individuals for their special assistance in the completion of this design project:

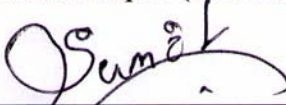
Dr. Daniel Schrage	Dr. Robert Loewy	Dr. JVR Prasad
Dr. Dimitri Mavris	Dr. Jimmy Tai	Dr. Sandeep Agarwal
Dr. Lakshmi Sankar	Dr. Amar Atre	Dr. Byung-Ho Ahn
Dr. Jou-Young Choi	Dr. Vitali Volovoi	Dr. David Eames
Dr. Eric N. Johnson	Dr. Mark Costello	Dr. Ilkay Yavrucuk
Dr. Suresh Kannan	Mr. Chang Chen	Mr. Russell Denney
Mr. Ian Stults	Mr. Blake Moore	Mr. Peter Hart
Mr. Patrick Biltgen	Mr. Han Gil Chae	Mr. Adeel Khalid
Mr. M. Emre Gündüz	Ms. Jieun Ku	Mr. William Briley
Mr. Roy Smolky	Mr. Todd Grossaint	CPT Andrew Bellocchio
Mr. Tom Hanson	Mr. Alex Moodie	Mr. Ludvic Baquie

## 2006 Georgia Tech Graduate Design Team




---

Matthias Hoepfer (PhD Student)



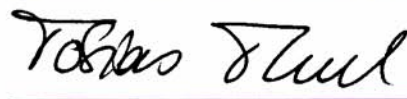
---

Sumit Mishra (PhD Student)



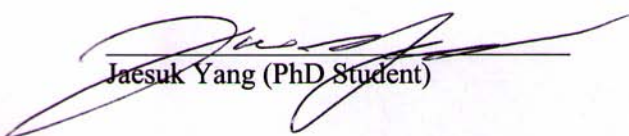
---

Apinut Sirojvisuth (Masters Student)




---

Tobias Theel (Masters Student)



---

Jaesuk Yang (PhD Student)



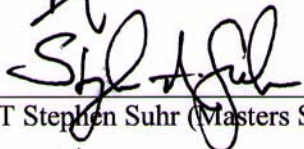
---

Bernard Laurendeau (Masters Student)



---

Kshitij Shrivastava (PhD Student)



---

CPT Stephen Suhr (Masters Student)



---

Lan Wu (PhD Student)

---

## Executive Summary

For a two-place turbine training helicopter to successfully enter today's challenging market, it must offer superior performance, handling qualities, and safety capability at a price competitive with that of the Robinson R-22, the current world sales leader in two-place piston training helicopters. In order to meet this formidable design challenge, the priority of this design effort was focused on the simplification of systems and subsystems for both the vehicle and the process by which it would be built. Therefore, an Integrated Product and Process Development (IPPD) methodology was used to drive the design solution.

For product development, the approach was centered on the heart or "core" of the helicopter – the main rotor system and the subsystems that make it function properly. As Tom Hanson describes in his *Hub Design Handbook*<sup>1</sup>, these subsystems can be classified as force transmittal, torque generation, and rotor control. Force transmittal allows the helicopter to effectively harness the lift and moments generated by the main rotor. Torque generation drives the main rotor by converting the work of the engine into the torque required for flight. Rotor control enables pilot inputs to be transmitted to the rotating rotor blades. Only through the simplification and efficient integration of these "core" elements could a successful design solution be achieved.

This training helicopter was developed out of a commitment to these fundamental design considerations. The Rambler incorporates an "Ideal Rotor," based on the Hanson elastic articulated (EA) rotor system, a new turboshaft engine and compact split-torque transmission, and a simplified flight control system – the integration of which achieves a synergistic effect in optimizing the vehicle's "core." The "Ideal Rotor" and split-torque transmission provide cost and safety enhancements through parts reduction and structural redundancy. Exceptional handling qualities can also be attributed to this rotor system design. The new turboshaft engine utilizes a simplified design approach to significantly improve its overall reliability, performance, and cost in comparison to existing turbine and piston alternatives. The simplified flight control system eliminates the need for hydraulic actuators, force-feel systems, or augmentation, except for the yaw axis – thus reducing the weight and complexity of this subsystem.

For process development, a Product Lifecycle Management (PLM) approach was used – capitalizing on the capabilities of state-of-the-art manufacturing analysis tools. By creating an integrated computer aided design and manufacturing (CAD-CAM) environment, the processes and resources required to produce the vehicle are optimized using virtual scenarios – thus improving the overall efficiency, quality, and cost of production.

Ultimately, the implementation of this IPPD methodology resulted in the development of a vehicle system solution that is far superior in performance, handling qualities, and safety to any training helicopter currently on the market.

---

## Table of Contents

<b>ACKNOWLEDGEMENTS .....</b>	<b>I</b>
<b>EXECUTIVE SUMMARY .....</b>	<b>II</b>
<b>TABLE OF CONTENTS .....</b>	<b>III</b>
<b>LIST OF FIGURES .....</b>	<b>VI</b>
<b>LIST OF TABLES .....</b>	<b>VIII</b>
<b>LIST OF SYMBOLS AND ABBREVIATIONS .....</b>	<b>IX</b>
<b>PROPOSAL REQUIREMENTS MATRIX .....</b>	<b>XII</b>
<b>TABLE OF PHYSICAL DATA.....</b>	<b>1</b>
<b>DIAGRAM SHEET 1 - THREE-VIEW DIAGRAM.....</b>	<b>2</b>
<b>DIAGRAM SHEET 2 - AIRCRAFT PROFILE .....</b>	<b>3</b>
<b>DIAGRAM SHEET 3 – ENGINE CENTERLINE SCHEMATIC.....</b>	<b>4</b>
<b>DIAGRAM SHEET 4 – DRIVE TRAIN SCHEMATIC .....</b>	<b>5</b>
<b>1 INTRODUCTION.....</b>	<b>6</b>
<b>2 REQUIREMENTS ANALYSIS.....</b>	<b>7</b>
2.1 TRAINING HELICOPTER MISSION ANALYSIS .....	7
2.2 TRAINING HELICOPTER MARKET RESEARCH .....	9
2.3 OVERALL DESIGN APPROACH TRADE STUDY .....	10
<b>3 PRELIMINARY VEHICLE SIZING AND PERFORMANCE .....</b>	<b>10</b>
3.1 VEHICLE CONFIGURATION SELECTION .....	10
3.1.1 Vehicle Sizing Methodology .....	10
3.2 VEHICLE PERFORMANCE .....	13
3.2.1 Aircraft Drag Estimation .....	13
3.2.2 Height-Velocity Diagram .....	14
3.2.3 Vehicle Performance Charts .....	14
3.3 VEHICLE WEIGHT AND BALANCE.....	16
3.3.1 Component Weight Analysis .....	16
3.3.2 Center of Gravity Envelope Estimation.....	17
<b>4 MAIN ROTOR AND HUB DESIGN .....</b>	<b>18</b>
4.1 HUB SELECTION TRADE STUDY .....	18
4.2 MAIN ROTOR BLADE DESIGN.....	20
4.2.1 Airfoil Selection.....	20
4.2.2 Blade Twist.....	21
4.2.3 Material Selection.....	21
4.2.4 Blade Section Properties.....	22
4.2.5 Fatigue Life Estimation .....	22
4.2.6 Manufacturing.....	23
4.4 HANSON “IDEAL ROTOR” HUB ANALYSIS .....	23
4.4.1 Modeling Methodology .....	23
4.4.2 Flexure Design.....	24

4.4.3 Static Droop Analysis .....	26
4.4.4 Quasi-Static Analysis.....	26
4.4.5 Auto-Trim Validation .....	27
4.4.6 Ground Resonance.....	28
4.4.7 Air Resonance.....	29
4.4.8 Rotor Noise Considerations .....	30
<b>5 TAIL ROTOR AND EMPENNAGE DESIGN .....</b>	<b>30</b>
5.1 CONFIGURATION TRADE STUDY .....	30
5.2 TAIL ROTOR SIZING .....	31
5.3 VERTICAL FIN.....	31
5.4 HORIZONTAL STABILIZER.....	31
5.5 EMPENNAGE .....	32
<b>6 PROPULSION SYSTEM DESIGN.....</b>	<b>32</b>
6.1 DESIGN SCOPE .....	32
6.2 PARAMETRIC CYCLE ANALYSIS .....	33
6.2.1 Turbine Cooling Trade Study .....	35
6.2.2 Parametric Cycle Analysis Conclusions .....	36
6.3 PERFORMANCE CYCLE ANALYSIS .....	36
6.3.1 Component Performance Maps .....	37
6.4 COMPONENT DESIGN CONSIDERATIONS .....	37
6.4.1 Compressor Configuration Selection.....	37
6.4.2 Centrifugal Compressor Design.....	38
6.4.3 Turbine Section Design .....	39
6.4.4 Combustion Section Design.....	41
6.4.5 Modular Gearbox Design .....	41
6.5 SPECIFICATIONS AND PERFORMANCE ANALYSIS .....	42
6.6 WEIGHT ANALYSIS .....	43
6.7 MANUFACTURING.....	43
6.8 FEDERAL AVIATION REGULATIONS (FAR) REQUIREMENTS.....	44
6.9 ADDITIONAL ENGINE DESIGN CONSIDERATIONS .....	45
6.9.1 Control System .....	45
6.9.2 Air Filtration System .....	45
6.10 TRANSMISSION DESIGN .....	46
6.10.1 Configuration Selection.....	46
6.10.2 Sizing and Analysis .....	47
6.10.3 Auxiliary Gearbox .....	49
<b>7 STRUCTURAL DESIGN.....</b>	<b>50</b>
7.1 STRUCTURAL DESIGN CRITERIA.....	50
7.2 FUSELAGE DESIGN.....	50
7.2.1 Configuration Selection .....	50
7.2.2 Composite Structure .....	51
7.2.3 Manufacturing.....	52
7.3 LANDING GEAR .....	53
7.3.1 Configuration Selection.....	53
7.3.2 Dimensions and Materials .....	53
7.3.3 Crashworthiness Analysis.....	53
7.3.4 Landing Gear Dampers.....	55

---

<b>8 STABILITY AND CONTROL ANALYSIS.....</b>	<b>56</b>
8.1 FLIGHT CONTROLS LAYOUT .....	56
8.2 FLIGHT CHARACTERISTICS .....	56
8.2.1 Helicopter Trim Solutions .....	56
8.2.2 Linear Control Root Locus Plots .....	59
8.2.3 FlightLab Modeling .....	61
8.3 HANDLING QUALITIES .....	63
8.4 FEDERAL AVIATION REGULATIONS (FAR) REQUIREMENTS .....	65
8.5 GEORGIA TECH UNIFIED SIMULATION TOOL (GUST) .....	65
<b>9 COCKPIT LAYOUT DESIGN.....</b>	<b>66</b>
9.1 HUMAN SIZE AND VISIBILITY CONSIDERATIONS .....	66
9.2 AIR CREW SEAT DESIGN .....	67
9.3 CONSOLE CONFIGURATION .....	67
<b>10 MANUFACTURING AND COST ANALYSIS .....</b>	<b>68</b>
10.1 PRODUCT LIFECYCLE MANAGEMENT (PLM).....	68
10.1.1 Virtual Engine Gearbox Assembly .....	69
10.2 COST ANALYSIS.....	69
10.2.1 Engine Cost Model .....	69
10.2.2 Recurring Cost .....	70
10.2.3 Direct Operating Cost (DOC) .....	71
10.2.4 Indirect Operating Cost.....	72
<b>11 SAFETY ANALYSIS AND AIRCRAFT CERTIFICATION .....</b>	<b>72</b>
11.1 SAFETY ANALYSIS .....	72
11.1.1 Functional Analysis .....	72
11.1.2 Functional Hazard Assessment.....	73
11.1.3 Preliminary System Safety Assessment (PSSA).....	73
11.2 CERTIFICATION PLAN .....	74
<b>12 CONCLUSION .....</b>	<b>75</b>
<b>APPENDIX A .....</b>	<b>A-1</b>
<b>APPENDIX B .....</b>	<b>B-1</b>
<b>APPENDIX C .....</b>	<b>C-1</b>
<b>REFERENCES.....</b>	<b>REF-1</b>

## List of Figures

Figure 1: Georgia Tech Preliminary Design Product and Process Development	6
Figure 2: Typical Mission Profile for Initial Rotary Wing Training (VFR Flight)	8
Figure 3: Typical Mission Profile for Advanced Rotary Wing Training (IFR Flight)	8
Figure 4: $R_f$ Methodology	11
Figure 5: $R_f$ Iteration Loop	11
Figure 6: Historical Weight Comparison	13
Figure 7: Height-Velocity Diagram Comparison	14
Figure 8: Rambler Performance Summary (SLS)	14
Figure 9: HOGE Altitude vs. Gross Weight	15
Figure 10: Payload vs. Range	15
Figure 11: Altitude vs. Maximum Continuous Speed	15
Figure 12: Weight and Balance Reference Lines	16
Figure 13: Estimated Center-of-Gravity Envelope	18
Figure 14: Hanson Hub Design	18
Figure 15: Steep Scale Pareto Chart	19
Figure 16: Conservative Scale Pareto Chart	19
Figure 17: Airfoil Power Requirements	20
Figure 18: Airfoil Rate of Climb Capability	20
Figure 19: Main Rotor Blade Cross-Section	21
Figure 20: Main Rotor Airfoil Mesh in ANSYS	22
Figure 21: Goodman Diagram for Kevlar 49/Epoxy	22
Figure 22: Goodman Diagram for S Glass/Epoxy	22
Figure 23: Simplified DYMORE Hub Model	24
Figure 24: Detailed DYMORE Hub Model	24
Figure 25: Standard Flexure Cross Section	24
Figure 26: Flexure Dimensions	25
Figure 27: Main Rotor Static Droop	26
Figure 28: Hanson Hub Fan Plot	27
Figure 29: Hanson Hub Feathering Auto-Trim	28
Figure 30: Ground Resonance Model	28
Figure 31: Ground Resonance Plot	29
Figure 32: Air Resonance Equations	29
Figure 33: Current Industry Trends for Key Turbine-Engine Design Parameters	33
Figure 34: "On-Design" Point Parametric Analysis	35
Figure 35: Turbine Cooling Technology Assessment	36
Figure 36: Turbine Cooling Trade Study	36
Figure 37: NEPP Engine Model	36
Figure 38: Centrifugal Compressor Performance Map	38
Figure 39: Blade Stress vs. Specific Strength	40
Figure 40: Turbine Material Selection Plot	40
Figure 41: High Pressure Turbine Performance Map	40
Figure 42: Power Turbine Performance Map	40
Figure 43: HP Available vs. Altitude (ISA)	42
Figure 44: HP Available vs. Altitude (ISA+20oC)	42
Figure 45: Fuel Flow vs. Altitude (TOP)	42
Figure 46: Fuel Flow vs. Altitude (MCP)	42
Figure 47: SFC vs. Altitude (TOP)	43
Figure 48: SFC vs. Altitude (MCP)	43

Figure 49: Inlet Barrier Filter (IBF) System on the MD 500	46
Figure 50: Hanson Transmission Gears	47
Figure 51: Actual Hanson Transmission	47
Figure 52: V-n Diagram	50
Figure 53: Static Analysis of Fuselage	50
Figure 54: Composite Fuselage Design	51
Figure 55: Keel Beam Detail	52
Figure 56: Primary Structural Load Paths	52
Figure 57: Solid Model of Skid Landing Gear	54
Figure 58: Beam Element Model of Skid Landing Gear	54
Figure 59: Level Landing	55
Figure 60: Landing on One Skid	55
Figure 61: Hanson Swashplate Controls	56
Figure 62: Rambler Flight Controls Connectivity	56
Figure 63: Longitudinal Forces and Moments	57
Figure 64: Lateral Forces and Moments	57
Figure 65: Collective Pitch ( $\theta_0$ ) Control Position Plots	57
Figure 66: Longitudinal Pitch ( $\theta_{1s}$ ) Control Position Plots	57
Figure 67: Lateral Pitch ( $\theta_{1c}$ ) Control Position Plots	58
Figure 68: Tail Rotor Collective ( $\theta_{r0}$ ) Control Position Plots	58
Figure 69: Body Pitch Attitude ( $\theta$ ) Plots	59
Figure 70: Lateral Modes (Decoupled)	60
Figure 71: Longitudinal Modes (Decoupled)	60
Figure 72: Dynamic Modes (Coupled)	61
Figure 73: Rambler Parameter Sweep Results	61
Figure 74: Robinson R-22 Parameter Sweep Results	61
Figure 75: Linearized Eigenvalues for Reduced Aircraft Models	62
Figure 76: Pitch and Roll Damping versus Pitch and Roll Control Sensitivity at Hover	63
Figure 77: Yaw Damping versus Yaw Control Sensitivity at Hover	63
Figure 78: Longitudinal Long Term Oscillation	64
Figure 79: Lateral Long Term Oscillation	64
Figure 80: Pitch Control Analysis Corresponding to MIL-8501 and MIL 83300	64
Figure 81: GUST Model Simulator Panel	66
Figure 82: Left Seat Reach	66
Figure 83: Right Seat Reach	66
Figure 84: Visibility Plot	66
Figure 85: Cockpit Seat Configuration	67
Figure 86: Single Screen EFIS (VFR Only)	67
Figure 87: Dual Screen EFIS (IFR)	67
Figure 88: DELMIA Software Portfolio	68
Figure 89: Engine Gearbox Assembly Process	69
Figure 90: Cost Structure of Cost Driving Systems	70
Figure 91: Functional flow Block Diagrams	73
Figure 92: Rambler FHA (Catastrophic)	73
Figure 93: Powerplant Certification Schedule	C-1
Figure 94: Aircraft Certification Schedule	C-1



---

## List of Tables

Table 1: $R_f$ Parameter Sweep Variables	12
Table 2: Equivalent Flat Plate Drag Estimation	13
Table 3: Light Helicopter Performance Comparison (SLS Conditions)	16
Table 4: Center-of-Gravity Calculations (Empty Configuration)	17
Table 5: Center-of-Gravity Envelope Loading Conditions	17
Table 6: Hub Selection TOPSIS Results (Conservative Scale)	19
Table 7: Span-wise Flexure Data	25
Table 8: Component Technology Level Assumptions	34
Table 9: Turbine Design Parameters	39
Table 10: Engine Component Weight Breakdown	43
Table 11: FAR Part 27 Engine Requirements	44
Table 12: FAR Part 33 Engine Requirements	45
Table 13: Transmission Gear Sizing	48
Table 14: Transmission Gear Stress (TO Power Rating)	49
Table 15: Auxiliary Gearbox Stress (TO Power)	49
Table 16: Limit Drop Test Results	55
Table 17: Stability and Control FAR Requirements	65
Table 18: Rambler Direct Operating Cost Breakdown (\$2006)	71
Table 19: DOC Comparison (\$2006)	72
Table 20: MIL-STD-1374 Group Weight Statement	A-1
Table 21: Recurring Cost Breakdown	B-1

---

## List of Symbols and Abbreviations

### Symbols:

$b$	Number of Blades
$c$	Chord
$C_d$	Drag Coefficient
$C_l$	Lift Coefficient
$f$	Flat Plate Drag Area
$L_v$	Dihedral Effect
$L_p$	Damping in Roll
$L_{\delta a}$	Roll Control Power
$M_u$	Speed Stability
$M_w$	Angle of Attack Stability
$M_q$	Pitch Damping
$M_{\delta c, \delta e}$	Cyclic Pitch control Effectiveness
$N_v$	Directional Stability
$N_r$	Yaw Damping
$N_{\delta p}$	Yaw Control Power
$R$	Radius
$T_4$	Turbine Inlet Temperature
$V_{DL}$	Design Limit Flight Speed
$V_H$	Design Maximum Level Flight Speed
$V_{NE}$	Never Exceed Flight Speed
$V_T$	Blade Tip Speed
$X_u$	Drag Damping
$X_w$	Drag due to Angle of Attack
$X_q$	Drag due to Pitch Rate
$X_{\delta c, \delta e}$	Drag due to Collective and Cyclic Control Displacements
$Y_v$	Sideward Damping
$Y_{\delta a}$	Side Force due to Cyclic Control
$Z_u$	Lift due to Velocity
$Z_w$	Heave Damping
$\alpha$	Angle of Attack
$\delta_a$	Lateral Cyclic Control
$\delta_c$	Collective Cyclic Control
$\delta_e$	Longitudinal Cyclic Control
$\delta_p$	Pedal Control
$\theta$	Body Pitch Attitude
$\theta_o$	Collective Pitch

---

$\theta_{tro}$	Tail Rotor Collective Pitch
$\theta_{ls}$	Longitudinal Pitch
$\theta_{lc}$	Lateral Pitch
$\sigma$	Solidity
$\omega$	Disk Loading

**Abbreviations:**

ADI	Attitude and Direction Indicator
AHP	Analytical Hierarchical Process
AHIP	Army Helicopter Improvement Program
AHS	American Helicopter Association
AI	Autorotation Index
BL	Butt Line
CAD	Computer Aided Design
CAM	Computer Aided Manufacturing
CFD	Computational Fluid Dynamics
CG	Center of Gravity
CNC	Computer Numerically Controlled
DFA	Design for Assembly
DFM	Design for Manufacture
DOC	Direct Operating Cost
EA	Elastic Articulated
ECU	Electronic Control Unit
EFIS	Electronic Flight Information System
EHSI	Electronic Horizontal Situation Indicator
FAA	Federal Aviation Administration
FADEC	Full-Authority Digital Engine Control
FAR	Federal Aviation Regulation
FBD	Free Body Diagrams
FFBD	Functional Flow Block Diagram
FHA	Functional Hazard Assessment
FOD	Foreign Object Damage/Debris
FS	Factor of Safety
FTA	Fault Tree Analysis
Gr/Ep	Graphite / Epoxy
GTPDP	Georgia Tech Preliminary Design Program
GUST	Georgia Tech Unified Simulation Tool
HIGE	Hover In-Ground Effect
HMA	Hydromechanical Metering Assembly
HOGE	Hover Out-of-Ground Effect

---

HPT	High Pressure Turbine
IBF	Inlet Barrier Filter
IFR	Instrument Flight Rules
IPPD	Integrated Product and Process Development
ISA	International Standard Atmosphere
ITU-LCH	Istanbul Technical University - Light Commercial Helicopter
Ke/Ep	Kevlar / Epoxy
MA	Markov Analysis
MADM	Multi-Attribute Decision Making
MCP	Maximum Continuous Power
NEPP	NASA Engine Performance Program
NOE	Nap-of-the-Earth
NTSB	National Transportation Safety Board
P4	Programmable Powder Preform Process
PART	Parametric Representation of Turbines
PDM	Product Data Management
PLM	Product Lifecycle Management
PSCP	Project Specific Certification Plan
PSP	Partnership for Safety Plan
PSSA	Preliminary System Safety Assessment
PT	Power Turbine
RBD	Reliability Block Diagrams
RFI	Request For Information
RFP	Request For Proposal
ROC	Rate of Climb
SCAS	Stability and Control Augmentation System
SFAR	Special Federal Aviation Regulation
SFC	Specific Fuel Consumption
SLS	Sea-Level Standard
SPN	Stochastic Petri Nets
STA	Station Line
TOP	Take-off Power
TOPSIS	Technique for Ordered Preference by Similarity to Ideal Solution
TRL	Technology Readiness Level
TURBN	Turbine Preliminary Design Program
UTS	Ultimate Tensile Strength
VABS	Variational Asymptotic Blade Section
VARTM	Vacuum Assisted Resin Transfer Molding
VFR	Visual Flight Rules
VTOL	Vertical Take-off and Landing
WL	Water Line

## Proposal Requirements Matrix

	Status	Section
<b>General Vehicle Requirements</b>		
Two-seat training helicopter	✓	3.1
Conceptually design a new turbine engine, as follows: - Low acquisition cost - Efficient to operate	✓	11.4 6.5
Initial Operational Capability in year 2012	✓	12.2
Aircraft must meet the safety and reliability standards of the Federal Aviation Administration's certification process as described in FAR Part 27	✓	12.2
Students should experience a positive habit transfer for future aircraft applications	✓	3.1
<b>Mission Profile Requirements</b>		
Aircraft must be capable of lifting the following payload: - Crew of two 90 kg people - 20 kg of miscellaneous equipment	✓	3.1.1
Aircraft must have enough fuel to sustain hover out of ground effect (HOGE) for 2 hours at 6,000 feet altitude on a ISA +20° C day	✓	3.1.1
Aircraft should be capable of operating in a wide range of environments: - Extreme temperature conditions - High altitude conditions - High winds and turbulence	✓	6.5 8.3
Aircraft design should accommodate beginner through advanced flight training	✓	2.1
<b>Performance Capability Requirements</b>		
Continuous HOGE at 6,000 feet and 74° F	✓	3.1.1
Maximum airspeed superior to current piston engine training helicopters	✓	3.2.1
Good autorotational capability	✓	3.2.2
Excellent handling qualities to ensure safe instructor pilot control margin	✓	8.2
Aircraft crashworthiness should exceed federal standards due to its mission as a training helicopter	✓	7.3.3
<b>Cost Requirements</b>		
Reduced acquisition cost is the highest priority consideration: - Innovative manufacturing cost reduction techniques - Cost must be competitive with current training helicopters	✓	10.1 11.3

## Table of Physical Data

<b>VEHICLE DATA:</b>		
<u>Property</u>		<u>Units</u>
Design Gross Weight	1353	lb
Maximum Gross Weight	1454	lb
Empty Weight	800	lb
Fuel:		
- Tank Capacity	18.8	gal
- Weight	114	lb
Useful Load	554	lb

<b>PERFORMANCE SUMMARY</b>			
<u>Category</u>	<u>SLS</u>	<u>6,000ft/ISA+20</u>	<u>Units</u>
Maximum Forward Airspeed	118	116	kts
Maximum Range	187	210	NM
Maximum Range Airspeed	85	90	kts
Maximum Endurance	2.75	2.9	HR
Maximum Endurance Airspeed	45	50	kts
Maximum Vertical Rate of Climb	2240	1520	ft/min
Maximum VROC Airspeed	45	50	kts
Maximum Hover VROC	2150	1050	ft/min

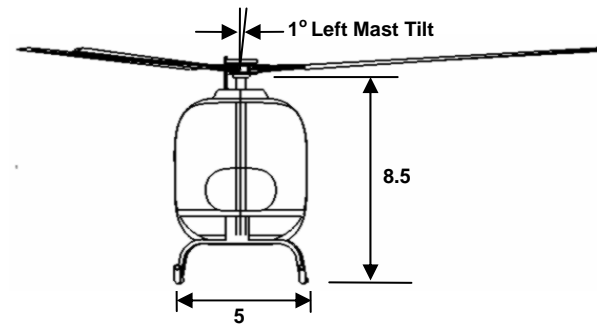
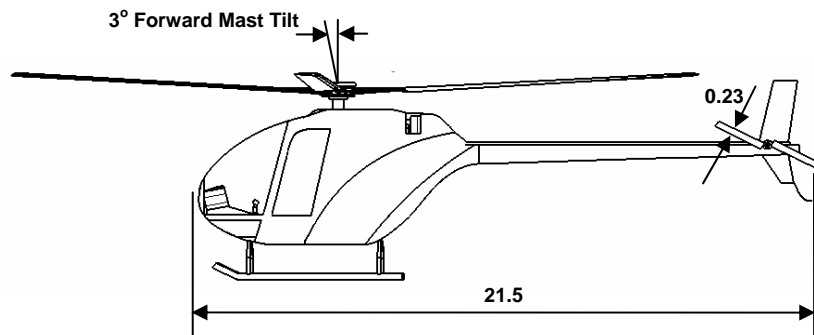
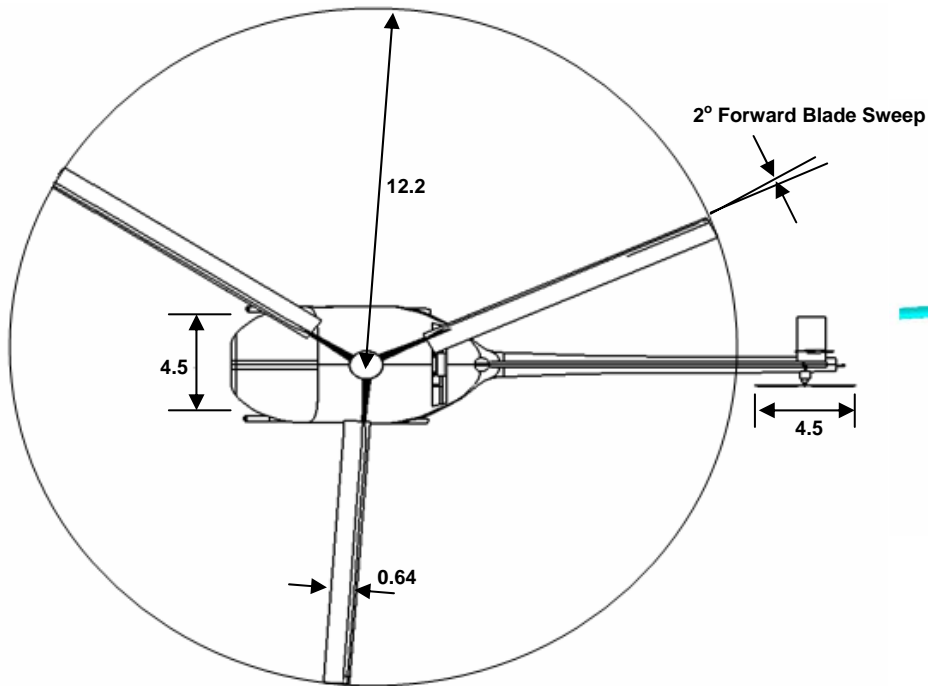
<b>MAIN ROTOR DATA:</b>		
<u>Property</u>		<u>Units</u>
Radius	12.2	ft
Chord	0.64	ft
Number of Blades	3	
Solidity	0.05	
Disc Loading	2.9	lb/ft <sup>2</sup>
Twist [deg.]	-10	deg
Tip Speed [ft/s]	650	ft/sec
Shaft RPM	509	RPM
Mast Tilt:		
- Forward	3	deg
- Left	1	deg
Airfoil	VR-7 OT	

<b>TAIL ROTOR DATA:</b>		
<u>Property</u>		<u>Units</u>
Radius	2.25	ft
Chord	0.23	ft
Number of Blades	2	
Solidity	0.064	
Tip Speed	700	ft/sec
Shaft RPM	3032	RPM
Airfoil	VR-7 OT	

<b>ENGINE DATA:</b>		
<u>Rating</u>	<u>SHp</u>	<u>SFC (lb/HP/hr)</u>
Takeoff Power (5 min)	184	0.49
Maximum Continuous Power	152	0.51
Cruise:		
Cruise A (90%)	137	0.52
Cruise B (75%)	114	0.54

<b>TRANSMISSION DATA:</b>	
<u>Rating</u>	<u>SHp</u>
Takeoff Power (5 min)	203
Maximum Continuous Power	168

# Diagram Sheet 1 - Three-View Diagram



*All dimensions are in feet*

## Diagram Sheet 2 - Aircraft Profile

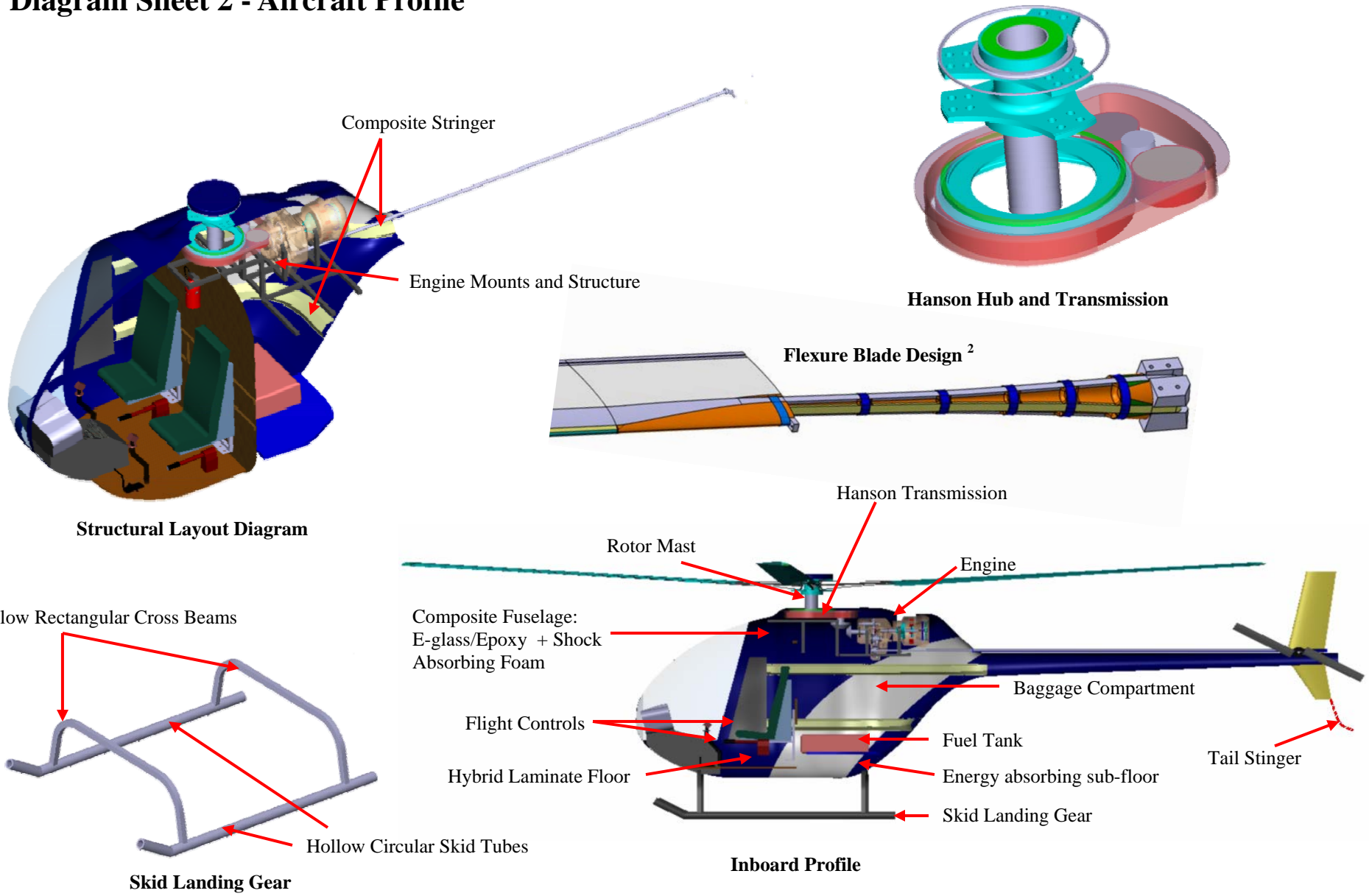
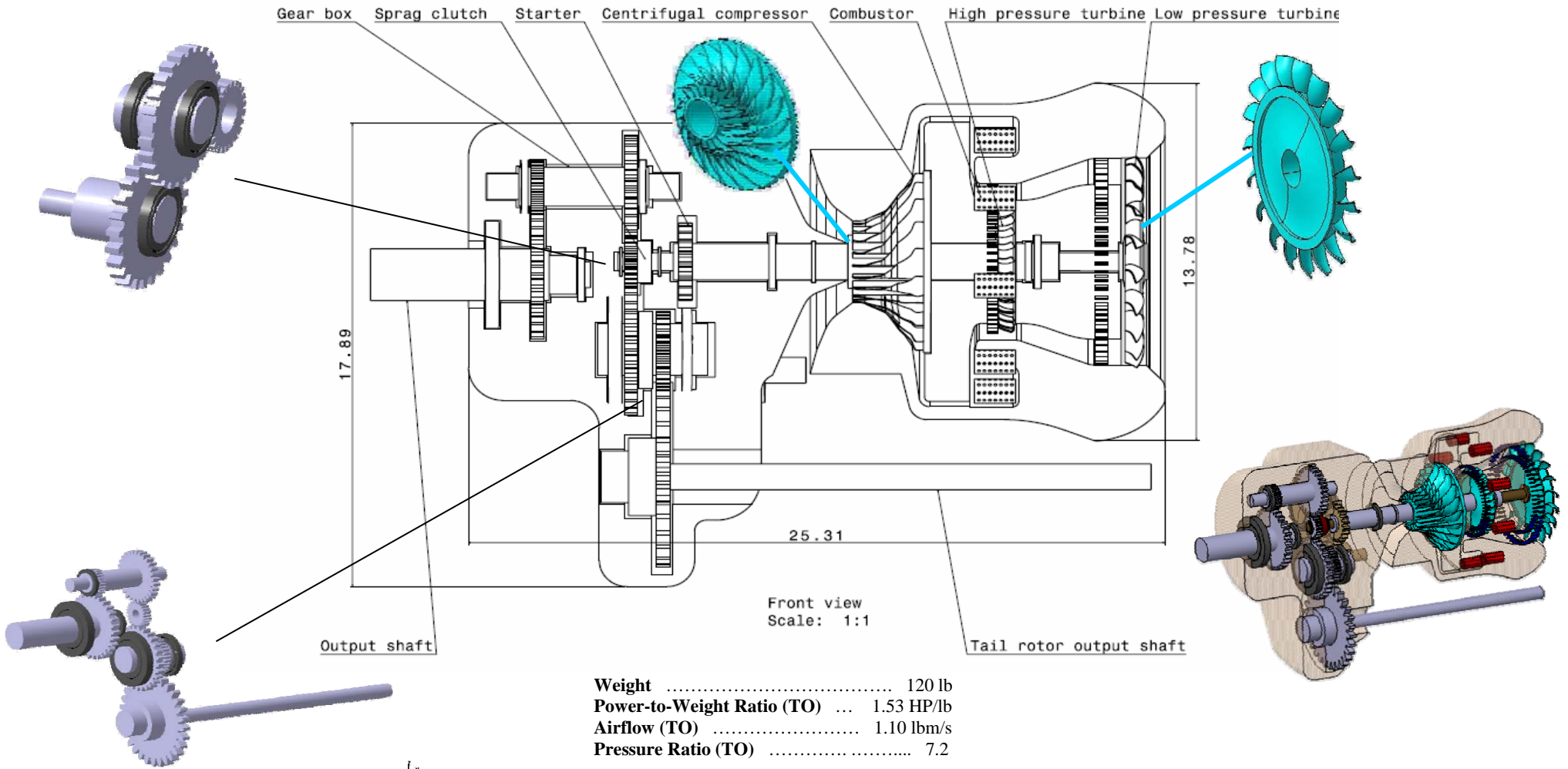


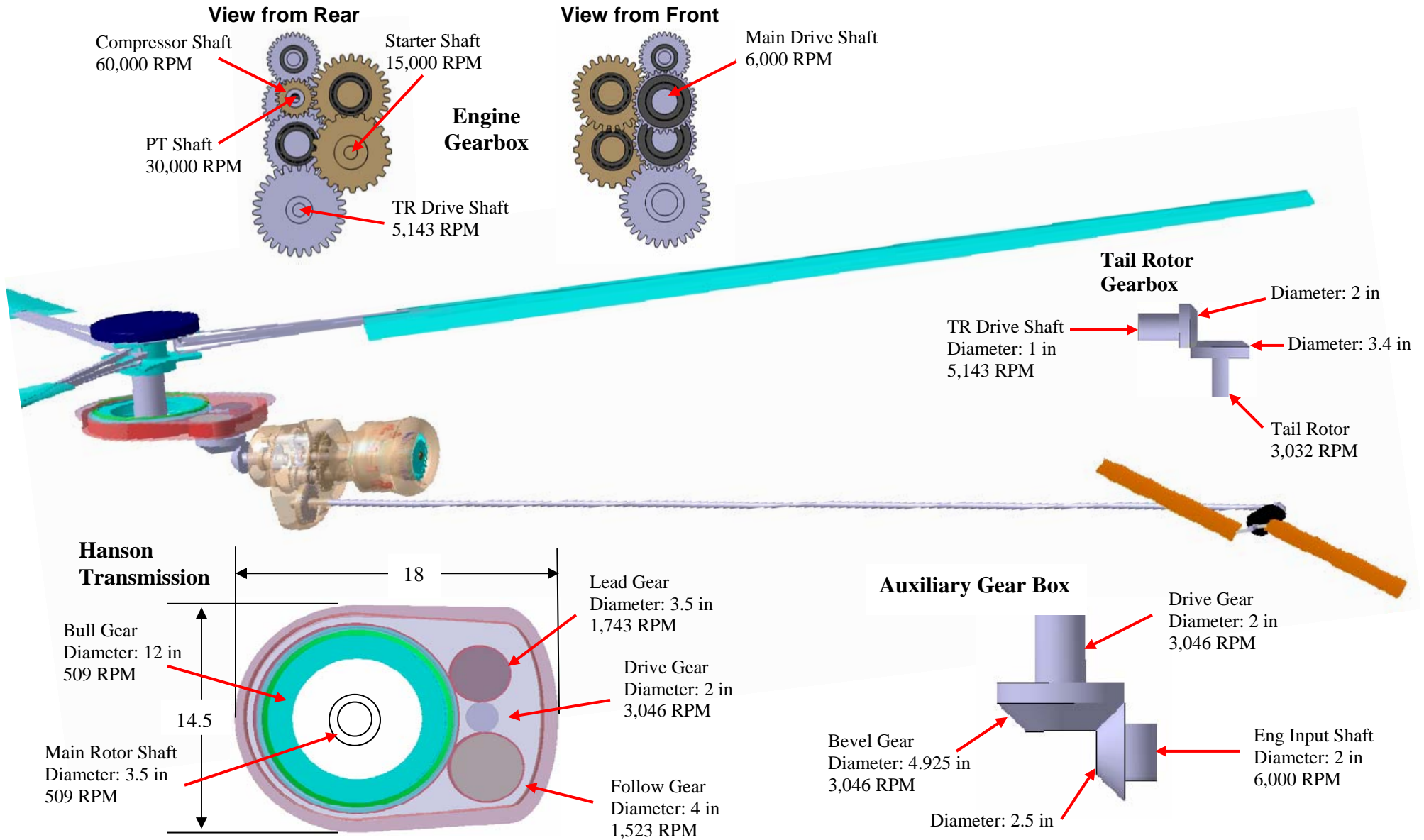


## Diagram Sheet 3 – Engine Centerline Schematic



All dimensions are in inches

## Diagram Sheet 4 – Drive Train Schematic



# 1 Introduction

In response to the 23<sup>rd</sup> Annual Student Design Competition sponsored by the American Helicopter Society (AHS) International and Bell Helicopter, this graduate student report describes the preliminary design of a two-place turbine training helicopter, with emphasis on cost efficiency and innovative manufacturing techniques. An integrated product and process development (IPPD) methodology was used in order to conduct parallel analysis and achieve effective synthesis of numerous product and process design disciplines. Figure 1 depicts graphically the IPPD process consisting of three design loops: Conceptual Design, Preliminary Design, and Process Design. An initial Product Data Management (PDM) loop is identified, as well. While aerospace and automotive companies are aggressively pursuing the full integration of computer aided design (CAD), computer aided manufacturing (CAM), and Product Data Management through Product Lifecycle Management (PLM), this team has taken a less aggressive approach, while still identifying the need for such integration.

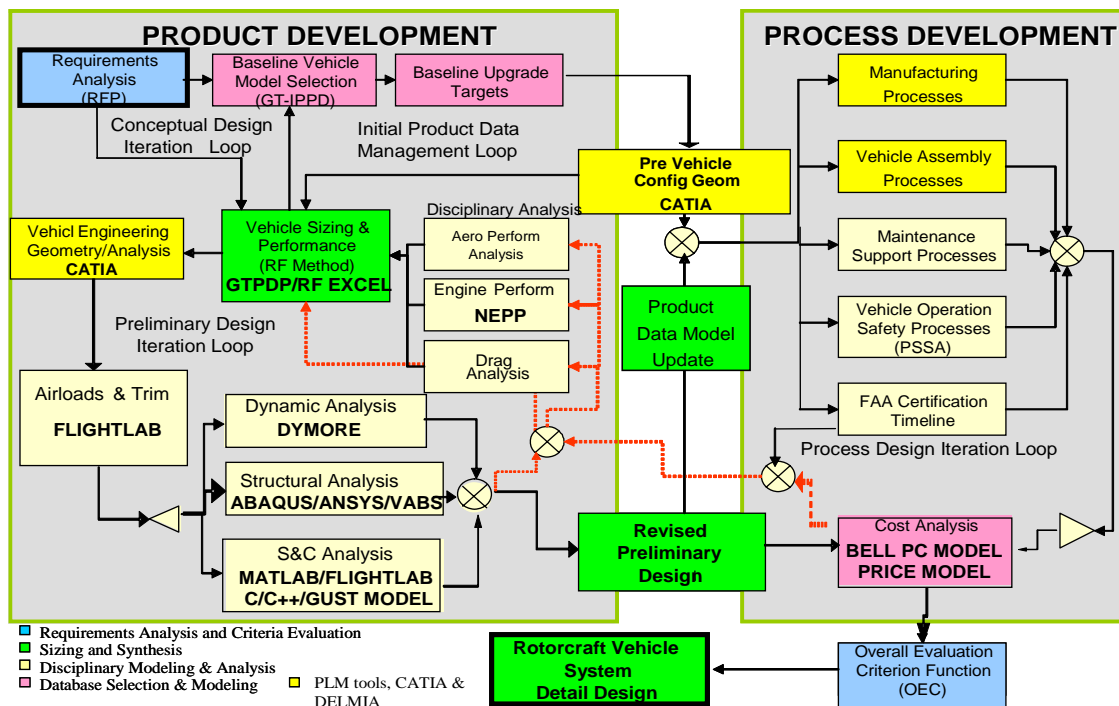


Figure 1: Georgia Tech Preliminary Design Product and Process Development<sup>3</sup>

Initially, the team developed a conceptual design baseline vehicle using the performance requirements stipulated in the request for proposal (RFP). This was followed by preliminary design which provided more detailed analysis in multiple disciplines to identify the necessary baseline vehicle modifications. These included aerodynamic performance optimization, structural design, analysis, and material selection, CAD modeling, helicopter stability and control analysis, dynamic analysis, propulsion

system design, helicopter training industry research, and cost analysis. The team has also addressed the influence of the manufacturing processes required for the design. Based on concepts of Design for Manufacture and Design for Assembly (DFM/DFA), the goals of this proposal can be summarized as reducing the cost and manufacturing cycle times while improving product quality and value.<sup>4</sup> To achieve these results, DELMIA, a state-of-the-art CAM tool, was used in conjunction with CATIA V5, a state-of-the-art CAD tool, for integrated design and manufacturing, especially for the new turboshaft engine. It was through the delicate balance of such product and process demands that the team could efficiently achieve a design solution that ultimately satisfied the customer's needs.

## **2 Requirements Analysis**

In today's helicopter market, *"it is apparent that there is a gulf between the operating characteristics of current light piston training helicopters and the fleet of turbine helicopters currently operating in commercial service."*<sup>5</sup> Specifically, this gulf exists in terms of performance, handling qualities, and cost. Piston engine helicopters lack the operational performance capabilities of turbine engine helicopters, but they dominate over the latter in procurement cost and operating efficiency. Therefore, the objective of this design is to close this gap in the light helicopter market by focusing on minimizing the acquisition cost primarily through incorporating a new conceptually designed, low-cost turbine engine.

The performance requirements are specified for the training helicopter with emphasis on hovering capability. The rotorcraft must be capable of lifting two 90 kg people, 20 kg of miscellaneous equipment, and enough fuel to hover out of ground effect (HOGE) for two hours at 6,000 feet altitude on an ISA +20°C day. After submitting a formal Request For Information (RFI), it was determined that this HOGE requirement only represents a sizing condition and does not imply a typical 2 hour mission profile. Additionally, a variety of training mission applications from initial rotary-wing certification to advanced training and maneuvers is desired. The autorotational capability and environmental durability of the aircraft must also be emphasized. While there is no specific maximum airspeed requirement, the aircraft should achieve performance better than piston engine trainer helicopters currently in service.

### **2.1 Training Helicopter Mission Analysis**

There are multiple variables to consider in designing this training helicopter as per the RFP. However, other than the subtle flight characteristics specific to a particular helicopter, the developmental training of new helicopter pilots follows a relatively standard procedure. The process is based on the progression of flight skills through constant increase of the level of difficulty of each flight maneuver as a

direct function of the safety comfort level of both the instructor pilot and the trainee. Typically, this process begins as a combination of academic ground training on the aerodynamics and systems of the helicopter and hands-on initial flight training involving start-up, hover in-ground-effect (HIGE), and straight-and-level flight procedures. The flight maneuvers then progress to include autorotation procedures, both in hover and at altitude conditions, and hover out-of-ground-effect (HOGE) procedures. Hovering flight dominates the initial helicopter training sessions because of the inherent difficulty in mastering this basic maneuver. Figure 2 shows a typical mission profile for an initial rotary wing training flight. Based on a trainee's level of skill progression, advanced flight maneuvers such as maximum performance takeoff procedures, flight under simulated instrument flight rules (IFR) conditions, and advanced autorotation techniques such as autorotation with turn and autorotation with zero ground run will be performed. Figure 3 shows a typical mission profile for advanced training based on an instrument flight session. Longer range requirements were included to represent flights to multiple regional airfields often used by instructor pilots to practice operations within various airspace regulatory conditions. Consideration was also given to the potential military application of this training helicopter design. However, during the initial training stages, there is no significant difference between the requirements of civilian and military applications. It is only during advanced training where the military shifts its focus to combat skills such as low-level, nap-of-the-earth (NOE) flight and weapons employment.

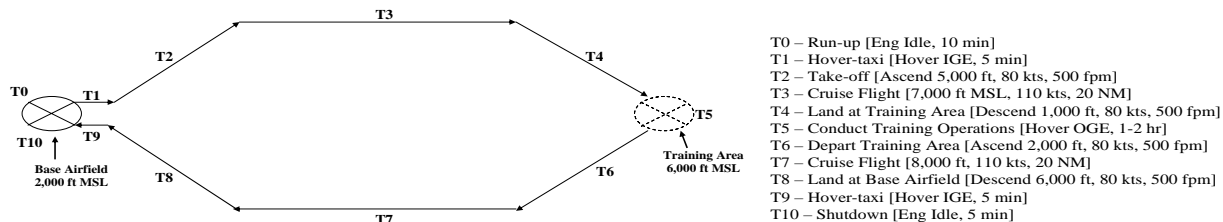


**Figure 2: Typical Mission Profile for Initial Rotary Wing Training (VFR Flight)**

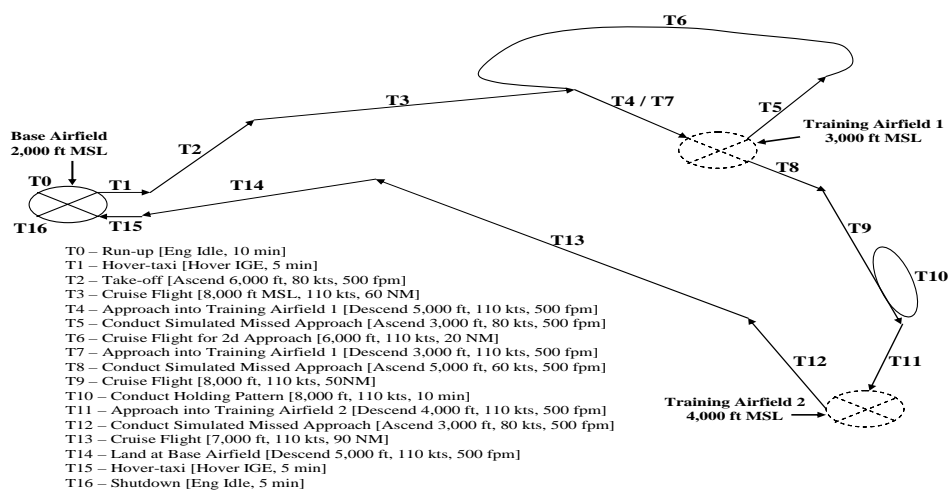


**Figure 3: Typical Mission Profile for Advanced Rotary Wing Training (IFR Flight)**

---

## 2.2 Training Helicopter Market Research

Market research was conducted by working with a local helicopter training company, *Air Atlanta, Inc.*, which operates throughout the metro Atlanta area. This company uses a combination of two Robinson R-22 helicopters and two Robinson R-44 helicopters to conduct training flights, aerial tours, and charter services. An interview was conducted with the owner, Mr. Blake Moore, in order to gain insight into key aspects of the training helicopter industry. During the interview, Mr. Moore stated, “[the Robinson R-22] is not a bad helicopter until something goes wrong.” He highlighted the following design limitations that could be improved:<sup>6</sup>

- limited autorotational capability due to a low inertia rotor system
- challenging power management at high altitudes, gross weights, and temperatures
- poor flight control design (“T-bar” configuration and non-adjustable pedals)
- potential mast bumping constraints during “low-G” pushover maneuvers
- narrow cabin width

In 1995, the Federal Aviation Administration (FAA) regulated special training requirements for the Robinson R-22 and R-44. These additional pilot training requirements came about because of a number of R-22 mast separation accidents in the early 1990s and remain in effect today under *SFAR 73 – Robinson R-22/R-44 Special Training and Experience Requirements*. Georgia Tech conducted an independent modeling and simulation assessment of the R-22 for the FAA in its Flight Simulation Laboratory in 1994-1995 to examine these concerns. The National Transportation Safety Board (NTSB) also participated in reviewing this assessment and made several recommendations in *NTSB Special Investigation Report – 96/03*, which led to the issuing of SFAR 73. One of the recommendations was to develop simulators, like that created by Georgia Tech, for use by small helicopter companies and operators that do not have the resources to develop them on their own. Therefore, included with this proposal is a description of the Rambler training helicopter simulator, modeled with the Georgia Tech Unified Simulation Tool (GUST), for use in the development and fielding of the Rambler.

Mr. Moore also pointed out that the Robinson R-22 makes up for its performance shortcomings due to its low acquisition cost and direct operating cost (DOC). Specifically, he deemed direct operating cost as the most important benchmark within the training helicopter business model and placed acquisition cost as a secondary priority. In his company, each aircraft is sold well before its overhaul requirements are due, thereby offsetting some of the financial burden of a high initial purchase price. In response to the need for a new turbine engine training helicopter – he emphatically responded “yes”, but also emphasized a purchase price under \$300,000 to make it a competitive alternative to the piston engine training helicopters currently on the market.<sup>6</sup>

## ***2.3 Overall Design Approach Trade Study***

During the conceptual design loop of the IPPD methodology, the team conducted a trade study related to the benefits of creating an entirely new vehicle design versus using a derivative of an existing design. Using the Technique for Ordered Preference by Similarity to the Ideal Solution (TOPSIS), a multi-attribute decision making (MADM) tool, the team quantitatively and qualitatively evaluated the benefits of creating a completely new design versus creating a major or minor derivative of an existing design. The evaluation was based on manufacturing cost, direct operating cost, autorotational capability, hover efficiency, maximum airspeed, static stability, flight handling qualities, cockpit design, crashworthiness, and certification timeline. Based on the RFP, which stated that non-recurring development cost need not be considered, the benefits of the new design option were superior. Thus, the primary direction of this preliminary design process was firmly established.

# **3 Preliminary Vehicle Sizing and Performance**

## ***3.1 Vehicle Configuration Selection***

The initial aircraft configuration was based on the design of a conventional single main rotor helicopter with a traditional tail rotor anti-torque system and a skid landing gear. This configuration was selected for two main reasons: simplicity of design and training effectiveness. Because the emphasis for this design was on acquisition cost, a conventional design approach was considered appropriate. Additionally, due to the mission of this helicopter as a trainer, there was a distinct advantage in remaining conventional and limiting the design space. This would establish a training environment that promoted a positive student pilot habit transfer to larger, more sophisticated rotary-wing aircraft.

### **3.1.1 Vehicle Sizing Methodology**

The  $R_f$  Method, a preliminary sizing and performance technique used to design and evaluate vertical take-off and landing (VTOL) and conventional fixed wing aircraft, was used for this proposal. It uses a fuel balance, or  $R_f$ , approach to determine an optimized gross weight solution for a given vehicle sizing condition. Figure 4 shows the  $R_f$  Method, consisting of two design loops to determine vehicle power loading and vehicle gross weight. The power loading loop produces a ratio of power available and power required while the gross weight loop produces a ratio of fuel available and fuel required (Figure 5). By iterating on both loops, an optimized solution for minimum gross weight and required installed power can be achieved when the fuel available equals the fuel required and the power available equals the power required.

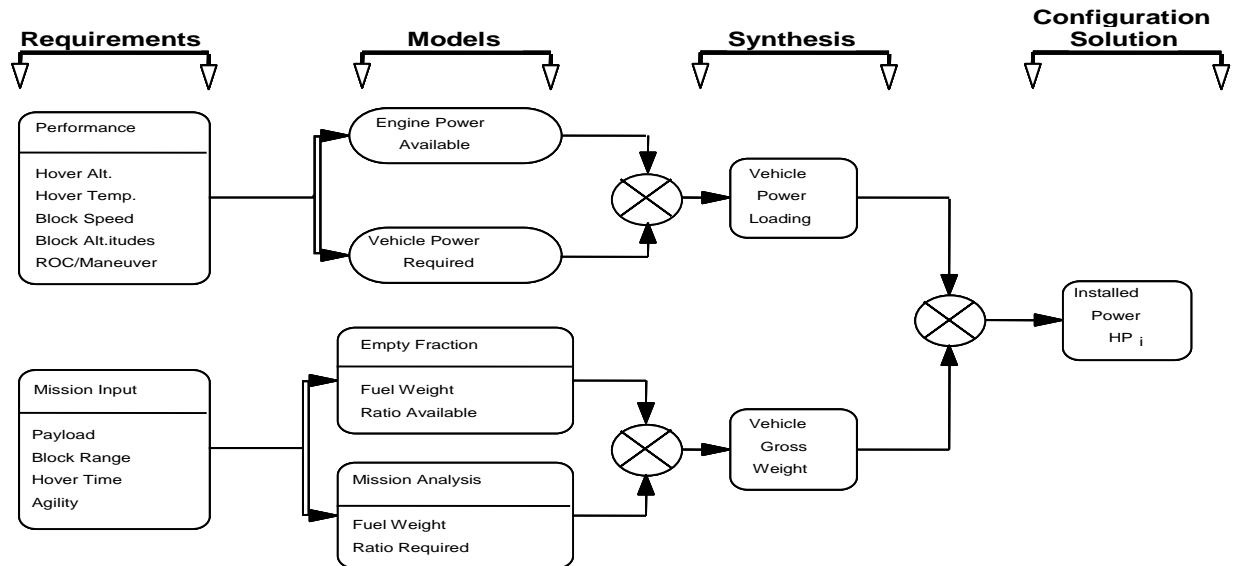


Figure 4:  $R_f$  Methodology <sup>7</sup>

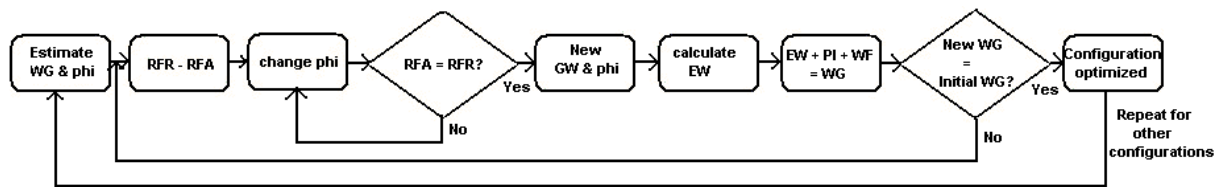


Figure 5:  $R_f$  Iteration Loop

Two separate sizing and performance applications – the Georgia Tech Preliminary Design Program (GTPDP) and an  $R_f$  Excel code written exclusively by a member of this team, were used for initial vehicle sizing synthesis. Although GTPDP has well-established accuracy and is sufficient for preliminary design, it represents a “black box” program in which the user only has access to the input and output executable files. As a result, the self-created  $R_f$  Excel Program was used as its coding was completely transparent and could be tailored to meet the project requirements. GTPDP was used as a calibration tool to provide the correlation required to certify the accuracy of the results of the  $R_f$  Excel Program. The sizing conditions explicitly stated in the RFP can be summarized as listed below:

- hover out of ground effect (HOGE) for 2 hrs at 6000 ft and ISA+20°C atmospheric conditions
- support a payload capability of 2 persons weighing 90 kg each and 20 kg of miscellaneous equipment for this hover out of ground effect requirement
- achieve forward airspeeds greater than piston-engine training helicopters

Based on these requirements, parametric studies were conducted to investigate the effects of changing several key design parameters – main rotor tip speed ( $V_T$ ), main rotor solidity ( $\sigma$ ), and disk loading ( $\omega$ ), as shown in Table 1.



**Table 1: R<sub>f</sub> Parameter Sweep Variables**

<b>Variable</b>	<b>Sweep Range</b>	<b>Step Interval</b>	<b>Units</b>
Disk Loading	2 - 10	1	lb/ft <sup>2</sup>
MR Tip Speed	600 - 800	50	ft/s
MR Solidity	0.025 - 0.050	0.005	

For each possible combination of these values, the R<sub>f</sub> loop was evaluated and the resultant gross weight was calculated. The optimum combination of these variables was selected based on the overall minimum gross weight solution. This result indicated the vehicle's overall size and general performance capabilities, in addition to the geometric characteristics of many other key parameters such as the main rotor radius (R), chord (c), number of blades (b), etc. The results of this sizing estimate were generally dependant on two main factors: the engine performance model and the weight breakdown equations. The engine model influenced the overall vehicle performance and its specific fuel consumption rate (SFC) determined the amount of fuel required by the vehicle for its mission. Therefore, a dependent engine-vehicle design relationship was developed that required several iterations for optimization. This iterative loop began with a theoretical engine model and resulted in a vehicle power requirement that drove the engine design. The new engine model was then integrated with the vehicle sizing for the next design loop. This process continued until a convergence was reached and a competitive vehicle design was achieved.

The second major factor in determining the minimum gross weight solution was the usage of empirical weight breakdown equations. Several different weight calculation methods are listed below:

- HESCOMP weight equations
- HESCOMP weight equations, calibrated to fit to Robinson R-22
- Weight fractions as presented in the Hiller 1100 sizing report
- Empty weight / gross weight ratio <sup>7</sup>
- Historical empty weight / gross weight data comparison
- Modified historical empty weight / gross weight data comparison
- Modified historical empty weight / gross weight data comparison, turbine-engine helicopters only
- Prouty's weight breakdown <sup>8</sup>

Most of these weight equations were insufficient in properly estimating the component weights of such a light helicopter. For instance, the HESCOMP equations, even when calibrated to the R-22, failed to provide reasonable results and seemed better suited for larger scale aircraft applications. Hence, the formulas presented in Prouty's textbook were used as a more realistic component weight estimation tool

for this small scale vehicle. Figure 6 below shows a graphical representation of the final empty weight / gross weight ratio,  $\phi$ , for this design in a comparison to historical data.

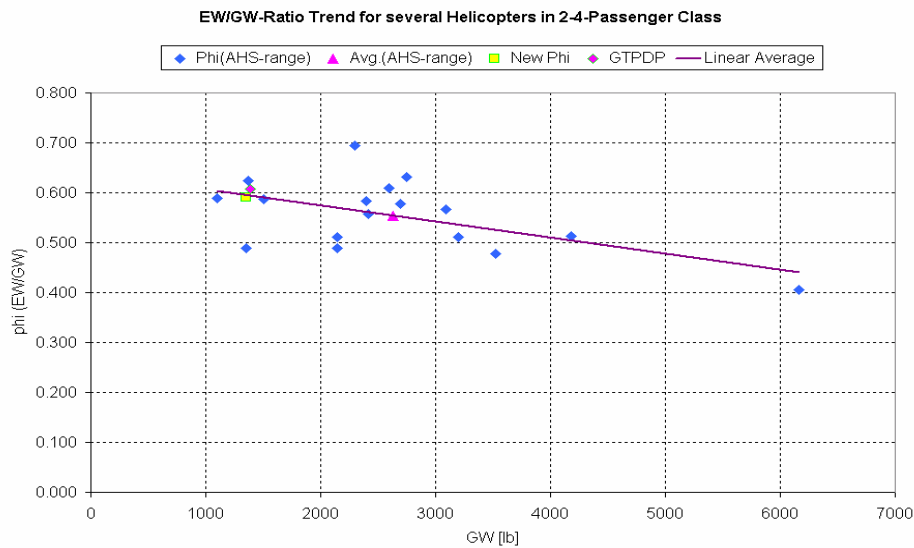


**Figure 6: Historical Weight Comparison**

## 3.2 Vehicle Performance

### 3.2.1 Aircraft Drag Estimation

A study of the influence of parasite drag on the vehicle, in particular, the airframe drag, was conducted in order to address the forward speed requirement. A drag build-up methodology was used to generate an accurate estimation of the equivalent flat plate drag area ( $f$ ) of the vehicle. In order to sum the drag contributions of the different sections of the vehicle, a code was programmed to perform these calculations and the resulting drag breakdown can be seen in Table 2.<sup>9</sup> The results are comparable with other small helicopters such as the Hiller 1100, now known as the FH1100, which has a value of 6.84 ft<sup>2</sup>.

**Table 2: Equivalent Flat Plate Drag Estimation**

<b>Vehicle Section</b>	<b>Drag Area [ft<sup>2</sup>]</b>
Fuselage	1.97
Tailboom	0.39
Engine Nacelles	0.44
Rotor Pylon and Transmission Fairing	0.33
Horizontal Tail	0.23
Vertical Tail	0.22
Landing Gear	1.31
Main Rotor Hub and Mast	2.04
Tail Rotor Hub and Mast	0.36
<b>Total:</b>	<b>7.29</b>

### 3.2.2 Height-Velocity Diagram

The height-velocity (H-V) diagram provides a measure of the vehicle's autorotational capability by indicating the "avoid" area for flight operations in which a safe autorotational landing is unlikely. The larger this area, the more limited the aircraft is in operating safely at lower airspeeds and altitudes. In an emergency situation, there will be insufficient rotor inertia to safely arrest the aircraft's rate of descent. Figure 7 shows an H-V Diagram for both the Rambler and the R-22.<sup>8</sup>

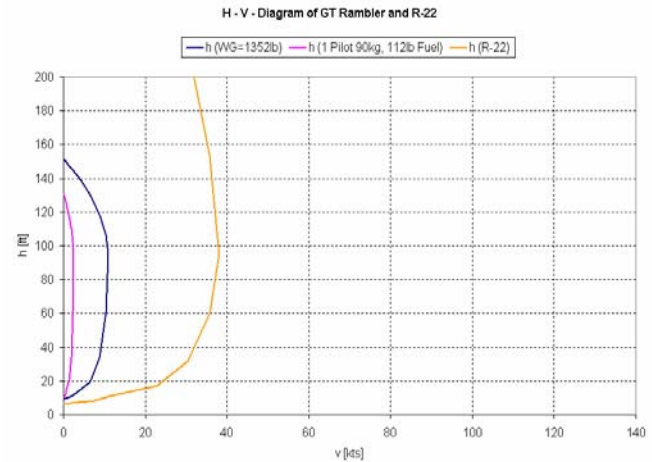


**Figure 7: Height-Velocity Diagram Comparison**

The diagram indicates that the Rambler, in both a heavy and lightweight configuration, has a significantly smaller "avoid" area than that of the Robison R-22 – demonstrating an important safety advantage.

### 3.2.3 Vehicle Performance Charts

Figures 8-11 were generated using the results of the  $R_f$  Excel preliminary sizing and performance tool and are representative of the Rambler's final design configuration.

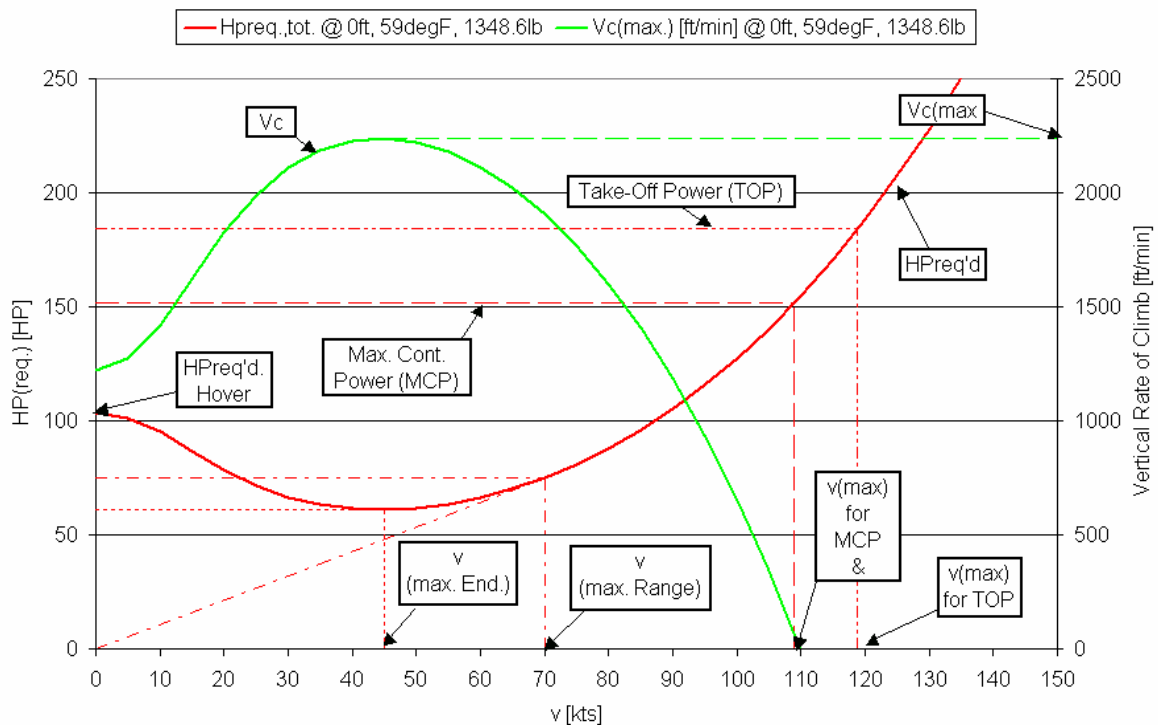


**Figure 8: Rambler Performance Summary (SLS)**

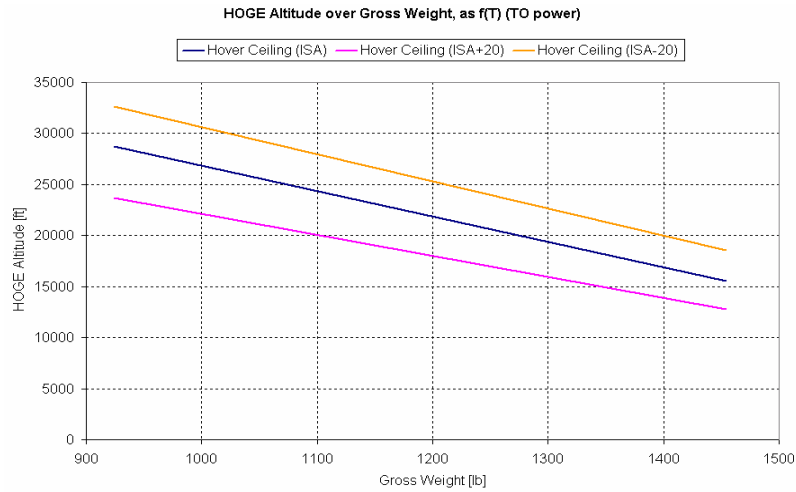


**Figure 9: HOGE Altitude vs. Gross Weight**

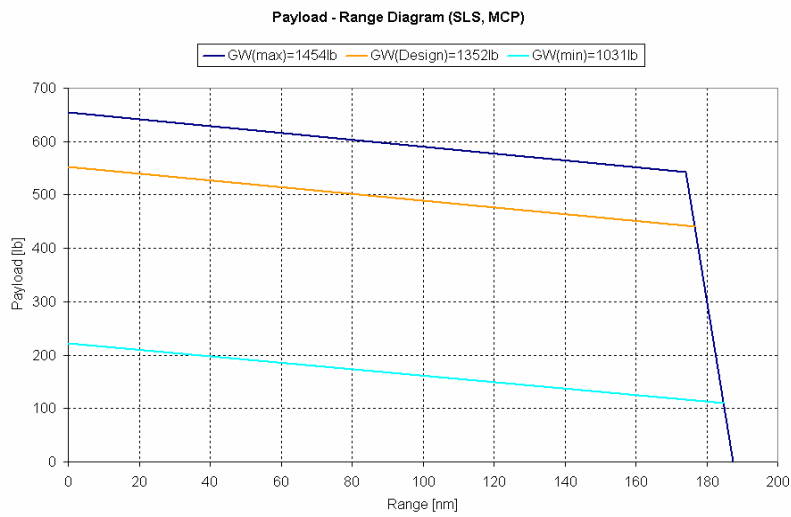


**Figure 10: Payload vs. Range**

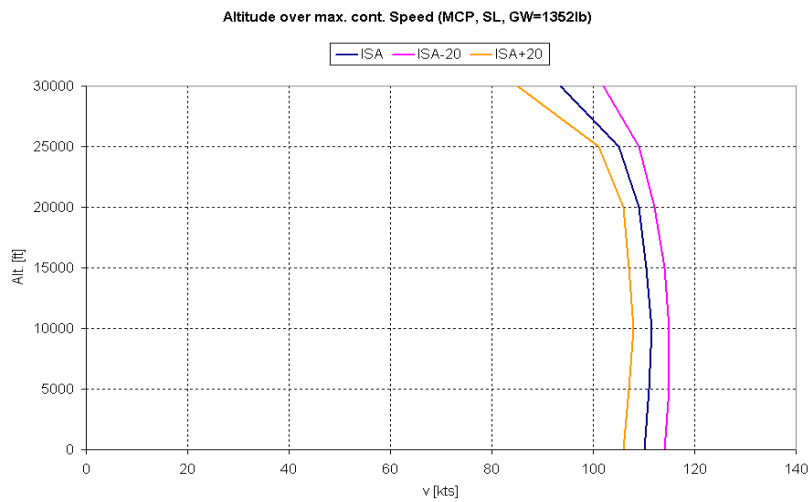


**Figure 11: Altitude vs. Maximum Continuous Speed**

Table 3 provides a performance comparison between the Rambler and other 2-place piston training helicopters. Across the competition, the Rambler clearly demonstrates superior flight speed, hover, and rate of climb capability. With respect to useful load and range, the Rambler outperforms the Robinson R-22 while remaining competitive with the significantly larger Schweizer 300C and Bell 47.

**Table 3: Light Helicopter Performance Comparison (SLS Conditions)**

<b>Aircraft</b>	<b>Gross Weight [lb]</b>	<b>Useful Load [lb]</b>	<b>Maximum Cruise Speed [kts]</b>	<b>Range [nm]</b>	<b>HOGE Ceiling [ft]</b>	<b>Rate of Climb [ft/min]</b>
Rambler	1353	554	108	187	18000	2240
Robinson R-22	1370	515	96	173	5200	1200
Schweizer 300C	2050	950	86	233	8600	990
Bell 47	2950	1050	80	214	12700	860

### 3.3 Vehicle Weight and Balance

#### 3.3.1 Component Weight Analysis

Component weight estimation and their influence on the lateral and longitudinal centers of gravity (CG) were performed using Prouty’s weight equations supplemented by a CATIA model and the R<sub>f</sub> Excel preliminary sizing tool. For the engine, the component weight was estimated using material density and volume in conjunction with CATIA (See Section 6.6) because a detailed model of the engine’s internal structure had been developed. Results matched well with those provided by GTPDP, as well as, with the historical trends. The CATIA model was used in determining the CG for each component based on the reference lines – Station line (STA), Water line (WL), and Butt line (BL) – shown in Figure 12.

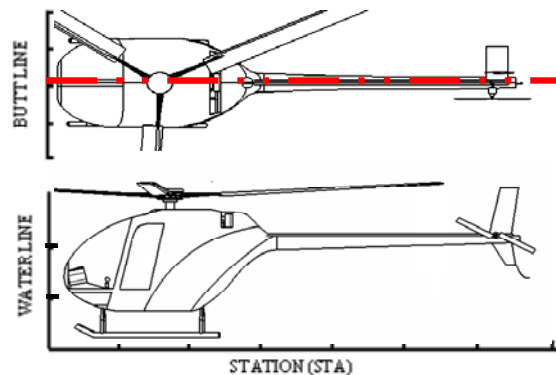


**Figure 12: Weight and Balance Reference Lines**

For maximum aircraft maneuverability, the overall vehicle center-of-gravity is located along the hub center of the rotor system. Taking the propulsion system, drive train, and fuel tank into account, the solution depicted on Diagram Sheet 2 was chosen. The fuel cell was located near the longitudinal CG in order to minimize the effects of fuel consumption throughout a given flight. Using the estimated component weights and component locations from the CATIA model, the moments along the nose station line, butt line, and water line along with an empty vehicle CG were calculated as shown in Table 3. A weight Statement in accordance with MIL-STD-1374 (now SAWE RP 7) for a standard loading condition is shown in APPENDIX A.

**Table 4: Center-of-Gravity Calculations (Empty Configuration)**

COMPONENTS WEIGHT	WEIGHT (lb)	NOSE STATION (in.)	MOMENTS (lb-in.)	BUTTLINE STATION (in.)	MOMENTS (lb-in.)	WATERLINE STATION (in.)	MOMENT (lb-in.)
BLADE MASS	68.0	66.17	4,499.36	0.00	0.00	78.32	5,325.62
HUB AND HINGE	33.4	66.17	2,209.98	0.00	0.00	78.32	2,615.82
HORIZONTAL STABILIZER	1.7	236.98	399.77	-14.00	-23.62	50.27	84.81
VERTICAL STABILIZER	3.6	236.98	852.72	-4.00	-14.39	53.27	191.69
TAIL ROTOR	4.5	236.98	1,074.76	11.04	50.05	50.27	228.00
FUSELAGE	198.5	68.35	13,566.77	0.00	0.00	34.80	6,908.34
LANDING GEAR	103.5	54.05	5,595.69	0.00	0.00	-8.38	-867.98
ENGINE INSTALLATION	120.0	94.83	11,379.36	0.00	0.00	60.22	7,226.04
PROPULSION SUBSYSTEM	33.7	94.83	3,196.56	0.00	0.00	60.22	2,029.86
FUEL SYSTEM	4.3	85.09	367.41	0.00	0.00	14.73	63.58
DRIVE SYSTEM	85.0	70.89	6,025.57	-0.52	-43.78	69.79	5,932.32
COCKPIT CONTROL	13.0	65.54	850.43	0.00	0.00	17.20	223.20
SYSTEM CONTROL	10.2	33.57	340.73	0.00	0.00	17.20	174.60
INSTRUMENT	5.2	17.63	91.39	0.00	0.00	19.19	99.44
ELECTRICAL	60.0	17.63	1,057.98	0.00	0.00	19.19	1,151.10
AVIONICS	30.0	17.63	528.99	0.00	0.00	19.19	575.55
FURNISHINGS AND EQUIPMENT	8.9	46.72	415.09	0.00	0.00	24.77	220.09
AIR COND. & ANTI-ICE	10.8	69.05	747.18	0.00	0.00	27.20	294.33
MANUFACTURING VARIATION	5.4	66.17	357.99	0.00	0.00	78.32	423.73
<b>EMPTY WEIGHT</b>	<b>799.7</b>	<b>66.97</b>	<b>53,557.74</b>	<b>-0.04</b>	<b>-31.74</b>	<b>41.14</b>	<b>32,900.15</b>

### 3.3.2 Center of Gravity Envelope Estimation

The center of gravity envelope is determined using test flights to analyze the vehicle's flight handling characteristics at various loading conditions. An estimate of this envelope was developed using the extreme loading configurations shown in Table 4. Each case was evaluated at maximum and minimum fuel loading condition. Figure 13 shows the longitudinal and lateral limits of the CG envelope and the associated CG travel for each fuel loading condition.

**Table 5: Center-of-Gravity Envelope Loading Conditions**

Case Study	Loading Condition	CG Limitation
1	1 pilot (110 lb)	Aft
2	1 pilot (250 lb)	Lateral
3	2 pilots (250 lb ea.) and payload (45 lb)	Forward

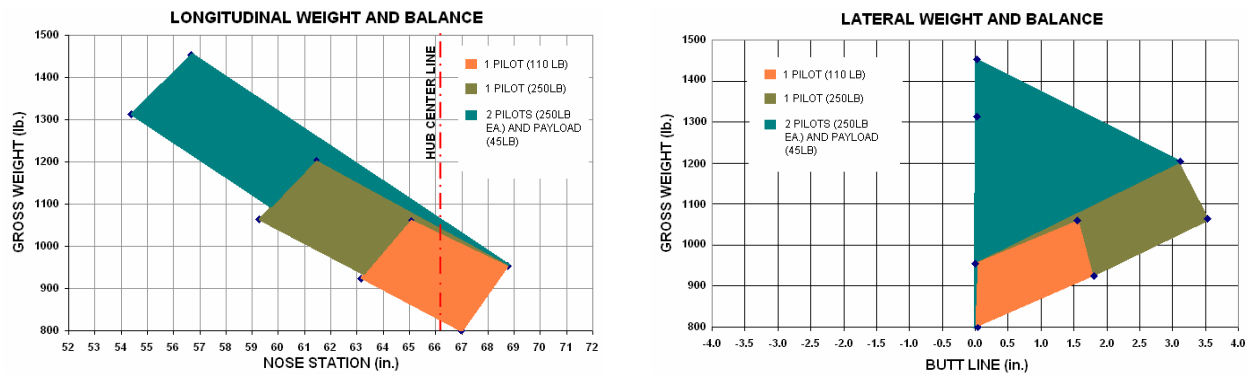


Figure 13: Estimated Center of Gravity Envelope

## 4 Main Rotor and Hub Design

Two baseline vehicles – each identical except for its hub design – were considered for analysis during the beginning stages of this design. A two-bladed teetering hub and a three-bladed Hanson bearingless hub were evaluated. Final selection was done based on qualitative and quantitative TOPSIS analysis.

### 4.1 Hub Selection Trade Study

While the two-bladed teetering hub system offered a simple and well-proven design solution, the Hanson hub represented an essential element of the “ideal rotor” (Section 4.4) and presented a unique opportunity in that its benefits were highly appealing, but difficult to prove. The historical precedence for the Hanson hub design was a successful flight on an auto-giro by Tom Hanson in 1970.<sup>1</sup> Over the past few years, Georgia Tech has participated in a joint research effort with the Istanbul Technical University (ITU-LCH) to investigate the qualities of this hub design for a light commercial helicopter. The team has used some of this historical data and research to evaluate the use of the Hanson hub design on a small training helicopter.

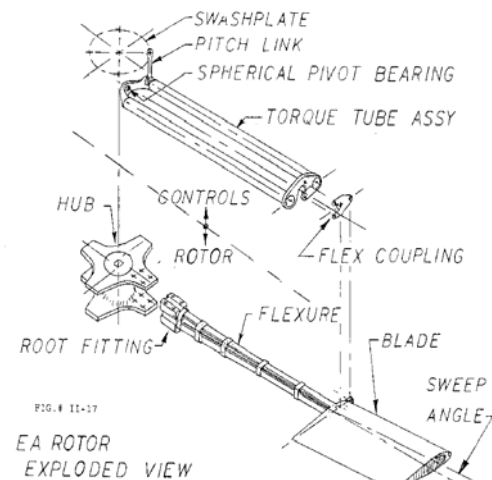
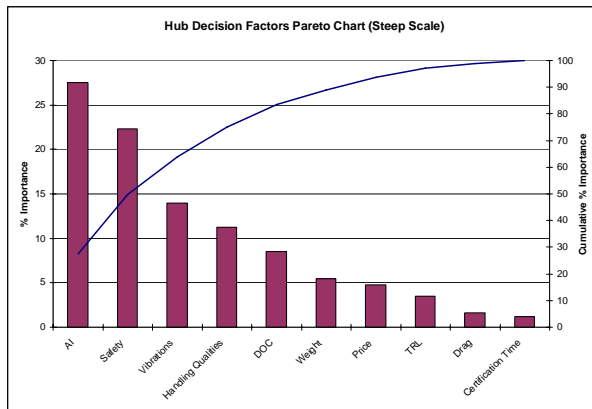


Figure 14: Hanson Hub Design<sup>1</sup>

The Hanson hub is based on a flexure design which uses a series of straps integrated into the blade structure to achieve “elastic articulation” – eliminating the need for the usual flapping, feathering, and lead-lag bearings.<sup>1</sup> Control inputs are provided to each blade through a combination of two torque-

tubes which provide structural redundancy. The flight controls are located within a non-rotating mast and operate through a swashplate above the rotor system (See Figure 61); this arrangement helps to protect the flight controls which are typically fragile. Figure 14 shows the design taken from Hanson’s Handbook.

The following list of decision factors was considered and evaluated using a comparison of the two baseline vehicle configurations: production cost, direct operating cost (DOC), drag, aircraft handling qualities, vehicle empty weight, autorotation index (AI), technology readiness level (TRL), safety characteristics, certification timeline, and vibrations. These factors were prioritized through an analytical hierarchical process (AHP) of pairwise comparisons using two different scoring scales. Figures 15 and 16 show the Pareto charts and results of this prioritization exercise.



**Figure 15: Steep Scale Pareto Chart**

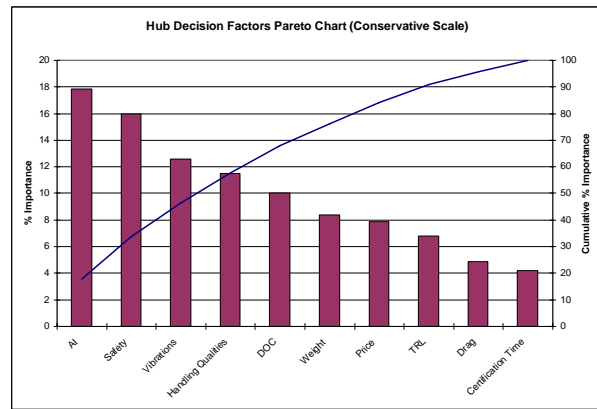


**Figure 16: Conservative Scale Pareto Chart**

Figure 15 shows that the first four categories of AI, safety, vibrations, and handling qualities account for 75% of the total factor importance; whereas, on the conservative scale, it is not until the sixth category that the 75% total is reached. These prioritization percentages were used as the weighting factors for a normalized matrix of raw data. From this result, the alternative that exhibited the closest similarity to the ideal solution was identified. Table 5 shows the final results for using the conservative scale – indicating that the 3-bladed Hanson hub design is better by 24%. For the steep scale, it was better by over 46%.

**Table 6: Hub Selection TOPSIS Results (Conservative Scale)**

Units		2-Bladed Teetering Hub			3-Bladed Hanson Hub				
Cost	\$	0.0785	1	207,364	0.6776	0.0532	225,064	0.7354	0.0577
DOC	\$	0.1003	1	164.22	0.6970	0.0699	168.97	0.7171	0.0719
Weight	lb	0.0838	1	800	0.6901	0.0578	839	0.7237	0.0607
Handling Qualities	C-H Level	0.1148	1	2	0.8944	0.1027	1	0.4472	0.0514
Drag	ft <sup>2</sup>	0.0490	1	1.95	0.6243	0.0306	2.44	0.7812	0.0382
AI		0.1785	h	36.4	0.7679	0.1370	30.4	0.6405	0.1143
TRL	Level	0.0680	h	9	0.8321	0.0566	6	0.5547	0.0377
Safety	Failure Rate	0.1597	1	1.61E-06	0.8752	0.1398	8.90E-07	0.4838	0.0773
Certification Time	yr	0.0419	1	0	0.0000	0.0000	2	1.0000	0.0419
Vibrations	per rev	0.1255	h	1	0.5981	0.0751	1.34	0.8014	0.1006
					0.0848		0.0521		
					0.0521		0.0848		
					<b>0.3806</b>		<b>0.6194</b>		



The total vehicle cost and DOC for each configuration were compared using preliminary results from the Bell Cost Model.<sup>10</sup> Vehicle empty weight comparisons were made using the R<sub>f</sub> Excel preliminary sizing tool. For the handling qualities, a qualitative assessment of the appropriate Cooper-Harper rating was used with the Hanson hub performing better than the less-responsive teetering system. Drag estimates for each hub design were based on historical percentages presented in Leishman's textbook and the autorotation index (AI) was calculated using the Sikorsky method in Equation 1:

$$AI = \frac{I_R \Omega^2}{2W \omega} \quad \text{Equation 1}^{11}$$

TRL was used to account for the design risk associated with the Hanson hub design; therefore, a lower value of 6 was assigned to indicate that only a design prototype or model has been successfully demonstrated in a relevant environment. Although the safety category represents a broad scope of considerations, the hub system failure rate was used as the best quantifiable indicator. Historical failure rates were used to assess the teetering system and fault tree analysis (FTA) was used to estimate the failure rate of the Hanson hub system. For the certification timeline, an additional two years were estimated for the Hanson design to account for the necessary ground and flight testing requirements. Finally, the vibrations factor was designed to capture the vibratory advantage of using a three-bladed Hanson design. The metric for this category used a comparison of the flap-wise frequency placement and number of blades for each rotor system.

## 4.2 Main Rotor Blade Design

### 4.2.1 Airfoil Selection

A trade study of the performance capabilities of numerous potential airfoil sections was conducted for selecting the main rotor airfoil. Using GTPDP to compare power requirements and rate of climb (ROC) performance for each airfoil, the graphs shown in Figures 17 and 18 were generated.

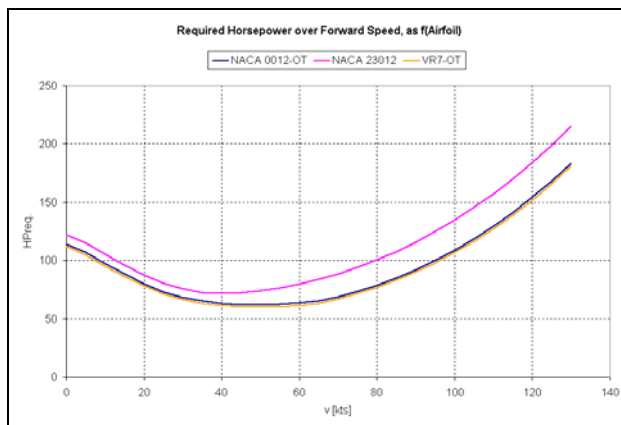


Figure 17: Airfoil Power Requirements

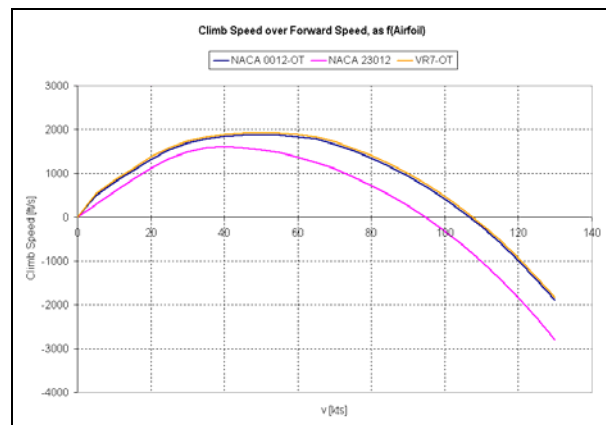


Figure 18: Airfoil Rate of Climb Capability

Of the airfoils available in the public domain, the VR-7 airfoil demonstrates the best overall performance across the entire spectrum of potential forward airspeeds for the Rambler. While a more advanced airfoil design may achieve better performance, this design effort was limited to the non-proprietary airfoil data available at Georgia Tech.

## 4.2.2 Blade Twist

In hover, high negative blade twist causes more uniform inflow across the blade – helping to reduce induced power and improve the figure of merit. Forward flight performance and vibratory loads limit this negative blade twist to a maximum of approximately 15° before performance losses result from the reduced angle of attack at the tip of the advancing blade.<sup>11</sup> Therefore, a main rotor blade negative linear twist of 10° was selected as the best compromise between maximizing the Rambler’s hover performance without significantly impacting its forward flight capability.

## 4.2.3 Material Selection

A composite main rotor blade structure was developed to integrate with the Hanson hub design. Initially, the use of self-healing composites to increase the safety and damage tolerance capability of the main rotor was explored; however, it was deemed unfeasible due to cost limitations. The final selection of main rotor materials was based largely on the previous research conducted at Georgia Tech as part of the ITU-LCH Program. Figure 19 depicts the Rambler’s main rotor blade section structural design.

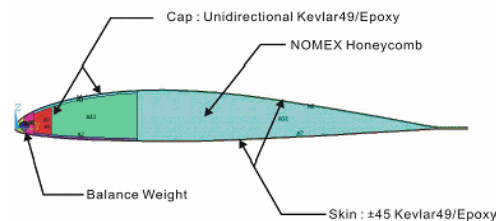


**Figure 19: Main Rotor Blade Cross-Section**<sup>2</sup>

Graphite/Epoxy (Gr/Ep) and Kevlar/Epoxy (Ke/Ep) were considered for the blade skin, and the latter was selected for its lighter weight characteristics. Ke/Ep also has good impact resistance which is important considering that blade damage due to impact is common. S-Glass/Epoxy was selected over Gr/Ep for the blade spar as it provides the required strength and stiffness while being less expensive. Nomex Honeycomb structures were used in the aft section of the blade for countering shear forces. A brass balance weight was used at the leading edge tip for mass balance. The material lay-up plies for the skin were calculated based on maximum stress failure criterion as shown in Equation 2:

$$N = E \cdot \epsilon \cdot n \cdot t_p \quad \text{Equation 2}$$

where  $N$  is the Critical Stress Resultant,  $E$  is the fiber Young's Modulus,  $\epsilon$  is the allowable strain,  $t_p$  is the thickness per ply, and  $n$  is the number of plies. For the Ke/Ep skin, four 4S plies were required, hence the laminate lay-up was selected as  $[45/-45]_s$ .

#### 4.2.4 Blade Section Properties

The Variational Asymptotic Blade Section (VABS) program, a code developed by Dr. Dewey Hodges at Georgia Tech, was used to compute the sectional geometric and material properties of the main rotor blade. A CATIA model of the airfoil was imported into ANSYS, a commercial finite element analysis tool, and meshed using three node linear triangle elements as depicted in Figure 20.

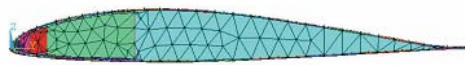


Figure 20: Main Rotor Airfoil Mesh in ANSYS

The composite laminate layer orientations and associated material properties were input into VABS and the mass and stiffness matrices were computed according to DYMORE convention. These properties were used for the DYMORE model for rotor blade and hub static and dynamic analyses (See Section 4.4).

#### 4.2.5 Fatigue Life Estimation

The main rotor blade was designed for infinite life – using 10,000 hours as the cycle criteria. Since there are multiple components and materials in the main rotor blade design, the fatigue life estimation was focused on the two key materials, Kevlar 49/Epoxy and Glass/Epoxy. Using material properties, reliability, surface finish and shape factors, and a factor of safety (FS) of 1.5, the alternating and mean cyclic stresses were calculated as shown in the Goodman Diagrams (Figures 21 and 22).

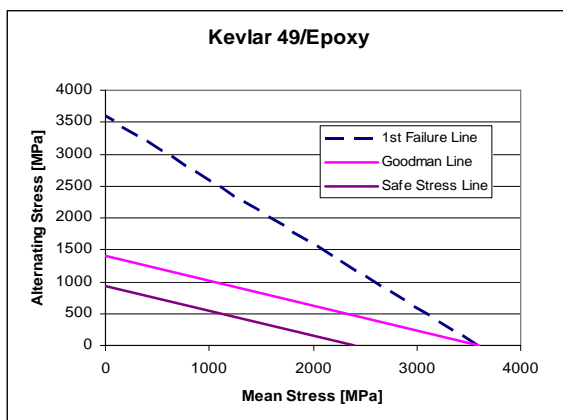


Figure 21: Goodman Diagram for Kevlar 49/Epoxy

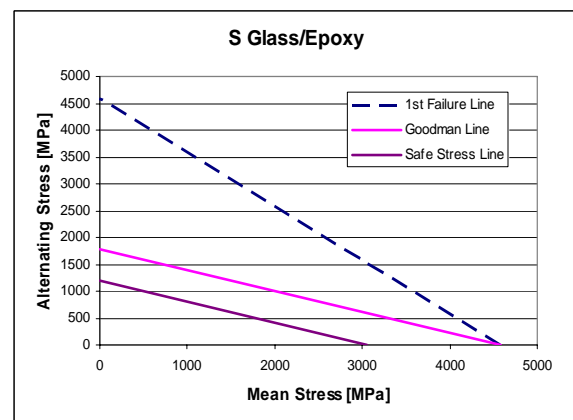


Figure 22: Goodman Diagram for S Glass/Epoxy

The Goodman Diagrams indicate the combinations of mean stress and alternating stress that satisfy the requirements of infinite fatigue life design. Each stress combination must remain inside of the safe stress line, which was calculated based on the maximum stress failure criterion. In the next iteration of the design, a usage spectrum, predicted loads from FlightLab<sup>12</sup>, and vibratory stresses from DYMORE will be used to verify the blade's infinite life.

#### **4.2.6 Manufacturing**

The blade will be manufactured in two halves. The upper and lower halves will be made out of Kevlar/Epoxy composite using vacuum assisted resin transfer molding (VARTM) – a composite manufacturing process in which dry fibers are laid on a tool and vacuum sealed, then resin is drawn into the component with a vacuum pump. The two sections will then be bonded together with the honeycomb structure placed at the aft section of the airfoil. The S-glass/epoxy spars will be manufactured by means of a specialized tool that would allow the composite material to be wrapped around it. The composites would then cure in an autoclave, or pressurized oven.

### **4.4 Hanson “Ideal Rotor” Hub Analysis**

In his *Hub Design Handbook*, Tom Hanson articulates the opportunity to design and build an “ideal rotor” exhibiting the following qualities:<sup>1</sup>

- Simplification of design
- Multiple load paths
- High ratio of ultimate tensile strength to blade centrifugal force
- Minimum number of structural joints
- Ability to maintain controlled flight after serious damage
- Principal blade natural frequencies below their respective forcing frequencies
- Stability about the feathering axis
- Minimum rotor noise by reducing  $V_T$
- Improved handling qualities

Tom Hanson demonstrated some these qualities during the 1960s through wind tunnel testing at NASA Langley, as well as, with his own whirl stand and three-bladed flying auto-giro. The dynamic analysis presented throughout the rest of this section is aimed at providing the necessary justification for such qualities, with the exception of the improved handling qualities addressed in Section 8.

#### **4.4.1 Modeling Methodology**

The DYMORE program, developed by Dr. Oliver Bauchau at Georgia Tech, was used for dynamic analysis to investigate the natural frequencies and perturbation response behavior of the rotor system. The model depicted in the Figure 23 was based on research conducted at Georgia Tech for the

ITU-LCH Program. Although this model depicts a traditional swashplate configuration, the actual swashplate is a “spider-type” design located above the rotor system. However, this modeling discrepancy is irrelevant because the mass properties and other physical constraints for the pitch links and swashplate were not input into the DYMORE program. As shown in Figure 24, the rotor blades are rigidly attached to the flexure beams with a  $2^\circ$  forward sweep angle to provide the aerodynamic auto-trim capability.

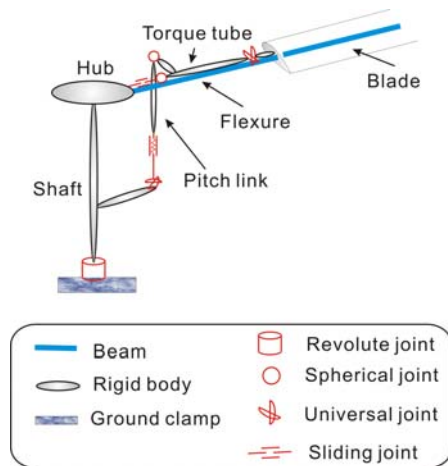


**Figure 23: Simplified DYMORE Hub Model <sup>2</sup>**



**Figure 24: Detailed DYMORE Hub Model**

A universal joint is used to connect each torque tube assembly to the root of the blade to allow for blade feathering. Each blade is modeled using four cubic beam elements in order to generate the inertial and elastic couplings that result from the use of composite materials and a forward sweep angle. A blade twist of  $-10^\circ$  and the aerodynamic properties of the VR-7 airfoil are also included in the model. At each time step in the DYMORE simulation, the aerodynamic loads acting on the blade beam elements are computed based on the simple lifting line theory.

#### 4.4.2 Flexure Design

The key element in Hanson’s hub design is the flexure design – a combination of elastic straps that allow the blade to experience lead-lag and flapping motions without hinges. The flexure consists of a core and four flex straps. The straps are configured to decouple the lead-lag and flapping motions, while the torque tubes are designed to provide blade feathering input. The material selected for the straps is Kevlar 49/Epoxy because it has a higher stiffness while still maintaining superior structural damping characteristics when compared with other composites. Figure 25 provides a cross sectional view of the flexure.

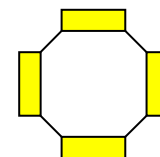


**Figure 25: Standard Flexure Cross Section**

A virtual flapping hinge offset of 10% of the rotor radius was used to enable a more responsive system with better handling qualities and provide sufficient damping to potentially eliminate the need for lead-lag dampers. With a hub radius of 4% of the rotor radius, the other 6% consisted of flexure strap structure. The inner 20% of the rotor disk will not produce beneficial lift, but since the rotational velocity in this region is relatively low, the loss in lift is minimal. Using the flexure design calculations described in Hanson’s report, the initial cross-sectional size, or cap size, was determined so that the geometric and mass properties could be used to calculate the radius of gyration and mass moment of inertia. Table 7 lists the material properties as a function of radial location.

**Table 7: Span-wise Flexure Data**

Radial Location	Flapwise	Chordwise	Torsion	Axial	Shear
4%	3,801,129	3,801,129	230,542	5,500,000	166,790
5%	3,194,004	3,194,004	193,719	5,500,000	166,790
6%	2,639,673	2,639,673	160,099	5,500,000	166,790
7%	2,138,135	2,138,135	129,680	5,500,000	166,790
8%	1,689,391	1,689,391	102,463	5,500,000	166,790
9%	1,293,440	1,293,440	78,448	5,500,000	166,790
10%	950,282	950,282	57,635	5,500,000	166,790
20%	1,580,661	1,580,661	68,910	5,500,000	166,790
	EI	EI	GJ	EA	GA

Although a single dimension, either chord-wise or flap-wise, can overlap within the flexure design, it is not an ideal configuration. Therefore, a standard cross section was selected with no overlap condition as demonstrated in the graph of the flexure dimensions shown as a function of radial location (Figure 26). The red line indicates where an overlap condition would occur.

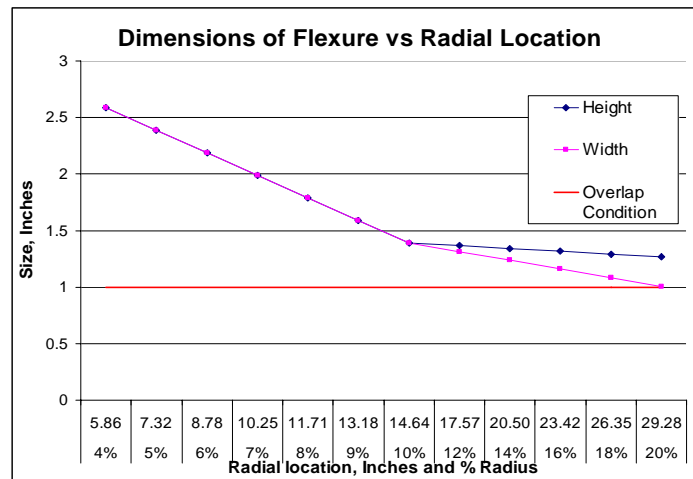


**Figure 26: Flexure Dimensions**

This design accounts for several of qualities, namely, design simplification, structural redundancy, high blade strength ratio, and a reduction in the number of structural joints. By eliminating the need for flapping and lead-lag hinges, the design saves weight, reduces maintenance, and decreases

the overall complexity of the rotor hub. The only structural joint required is where the blade connects to the hub, which uses a series of four attachment bolts to allow for easy blade removal and the potential for blade folding capability. In terms of safety and damage tolerance, the Hanson hub achieves structural redundancy in that the simultaneous failure of up to two flexure straps will not result in the loss of a blade. The use of composite materials also offers inherent structural redundancy because the multiple fiber orientations help prevent propagation of damage.<sup>13</sup> The dual torque tube provides a redundant means to transmit feathering inputs to the blade. The high strength ratio of flexure design is exhibited by the high ultimate tensile strength of composites in comparison with the relatively low centrifugal force of the rotor system.

#### 4.4.3 Static Droop Analysis

As a result of the inherent stiffness in the flexure design, the need for a static droop stop can also be eliminated – further simplifying the hub configuration. In order to verify this, a static droop analysis was conducted using the slow application of gravity in DYMORE. Figure 27 demonstrates a blade static droop of approximately 8 inches at its tip, an acceptable value for this design.

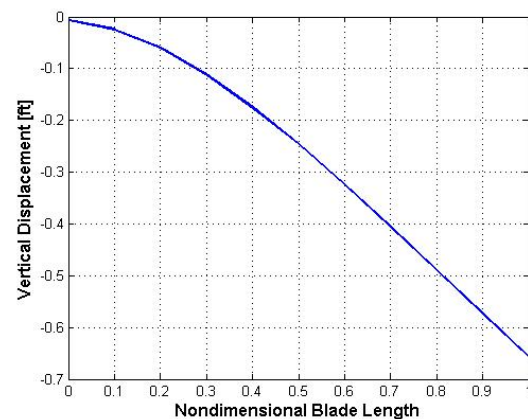
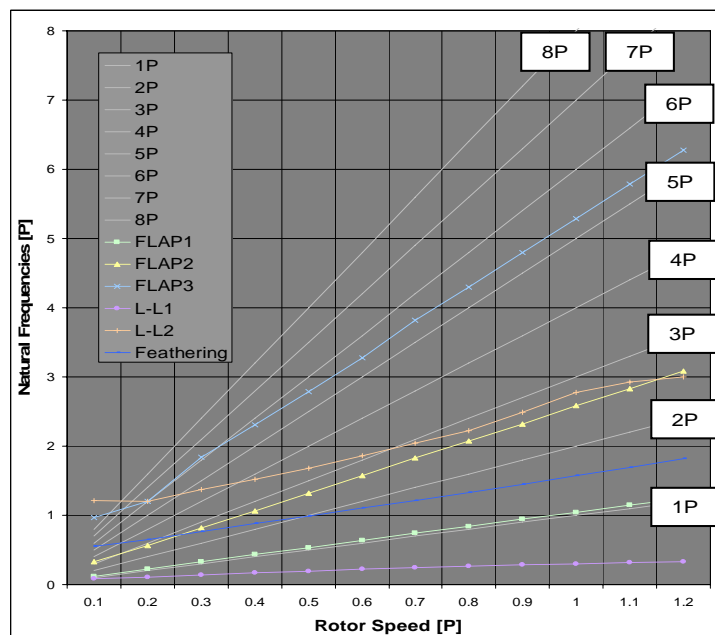


Figure 27: Main Rotor Static Droop

#### 4.4.4 Quasi-Static Analysis

The vibratory characteristics can be evaluated using DYMORE. The natural frequencies of the rotor system can be determined using a quasi-static case in which the velocity schedule in DYMORE is set to have each individual fraction of rotor speed occurring at a specific time. The in-plane motion of the blade takes place at multiples of the rotor’s rotational velocity. The vibratory excitation frequencies occur as a direct function of the number of blades on the rotor. The vibrations at rotational speeds of one minus and one plus the number of blades must be considered. Because the Rambler has a 3-bladed rotor system, the important frequencies considered are the forcing functions that occur at 1P, 2P, 4P, and multiples of 3P, where P is the per revolution frequency. The fan plot without air properties included (Figure 28) shows that Rambler has no adverse modes near 95% and 105% of the operating RPM as stipulated by FAR 27.1509. The fan plot also demonstrates several key qualities of Rambler’s hub design. The soft-in-plane characteristics of the first lead-lag mode have a frequency well below 0.5P; therefore, the potential

for air resonance has been eliminated. The principle blade natural frequencies are below their forcing frequencies, so that in the case of structural damage, further complications resulting from a destructive resonance situation will be avoided. Finally, the proximity of the first feathering mode to 1P eliminates the need for hydraulic powered flight control augmentation because the swashplate inputs require a 1P oscillation.<sup>1</sup> The convergence of first feathering mode to the one per rev with forward blade sweep is demonstrated in the proof of auto-trim functionality where air properties associated with VR-7 airfoil were included. Throughout most of the operating RPM, the blade forcing frequencies are not close to the aforementioned frequencies of 1P, 2P, 4P and multiples of 3P, which shows that Hanson hub design should help to eliminate the need for vibration absorbers.



**Figure 28: Hanson Hub Fan Plot**

#### 4.4.5 Auto-Trim Validation

As described in his award-winning paper and presentation at the 1997 AHS Forum, another advantage of the Hanson hub is its inherent stability about the feathering axis – allowing the system to better handle aerodynamic disturbances such as gusts.<sup>14</sup> This stability increases the damage tolerance of the rotor system because in the event of a broken pitch link, the blade will maintain a flat pitch setting throughout the emergency landing scenario. This “auto-trim” capability occurs as a result of the unique coupling of the flapping and feathering frequency due to the 2° of forward sweep in the blade. This configuration creates a matched flapping and feathering mode where the inter-modal coupling produces a nose down blade reaction to an upward aerodynamic disturbance. By incorporating the Hanson design to the main rotor, Rambler provides improved pilot handling capability because feathering axis (cyclic



control) is in phase with the rotor speed, and meets FAR 27.161 on trim control, where Rambler will “trim any steady longitudinal, lateral, and collective forces to zero in level flight at any appropriate speed.”

An analysis of auto-trim capability was first conducted by placing 50 lb-ft moment at the tip of the blade along the feathering axis during the static analysis of DYMORE to be used as the initial conditions for dynamic analysis. The auto-trim capability about the feathering axis has been demonstrated by running the analysis of a single-bladed model. Figure 29 shows that disturbance about the feathering axis returns to the trim condition of zero radians. The auto-trim capability of the Hanson rotor design is further explained in the analysis of the ITU-LCH program, which demonstrated the blade’s natural tendency to dampen an aerodynamic disturbance in both the flapping and feathering modes, respectively.<sup>2</sup>

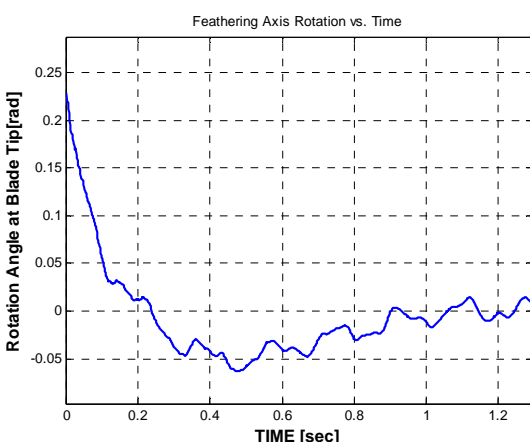


**Figure 29: Hanson Hub Feathering Auto-trim**

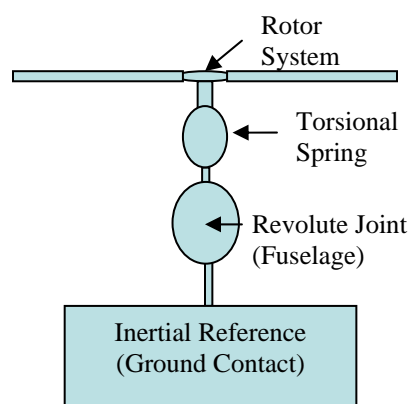


**Figure 30: Ground Resonance Model**

#### 4.4.6 Ground Resonance

Because the Hanson hub uses a soft-in-plane rotor system, the potential for ground and air resonance must be examined. Ground resonance is a destructive coupling of the natural frequencies of the vehicle body with the rotor in-plane frequencies. A ground resonance model was created in DYMORE to verify that Rambler is free from this condition. As depicted in Figure 30, the Rambler’s combined fuselage and landing gear properties were modeled using a torsional spring with an equivalent torsional stiffness of the roll and pitch axis of the vehicle.

Using a finite element model of the skid landing gear modeled in ABAQUS (See Section 7.3.3), the rotational stiffness of the landing gear was extracted using linearized moment versus rotation output. A linear static analysis was conducted and a pitching and rolling moment of 2 lb-in was applied. The right skid landing gear was prescribed a pinned boundary condition and the left skid was prescribed a Z-

symmetric boundary condition with one displacement and two rotations along the appropriate directions prescribed as zero. An equivalent torsional spring constant was determined and the model was then connected to the inertial frame so that its relative motion could be observed. DYMORE model results in Figure 31 show that the regressive lead-lag mode intersects the body roll mode at 1.18P when the frequencies coalesce, which indicates that Rambler is free of a ground resonance condition within its normal operating limits from 0 to 1.18P. This meets the FAR 27.1509 by covering all operating rotor speeds up to and including 1.05 times the operating RPM. Also, the high equivalent hinge offset of the Rambler, similar to that of the BO-105, provides substantial damping and demonstrates that additional lead-lag dampers are not required.

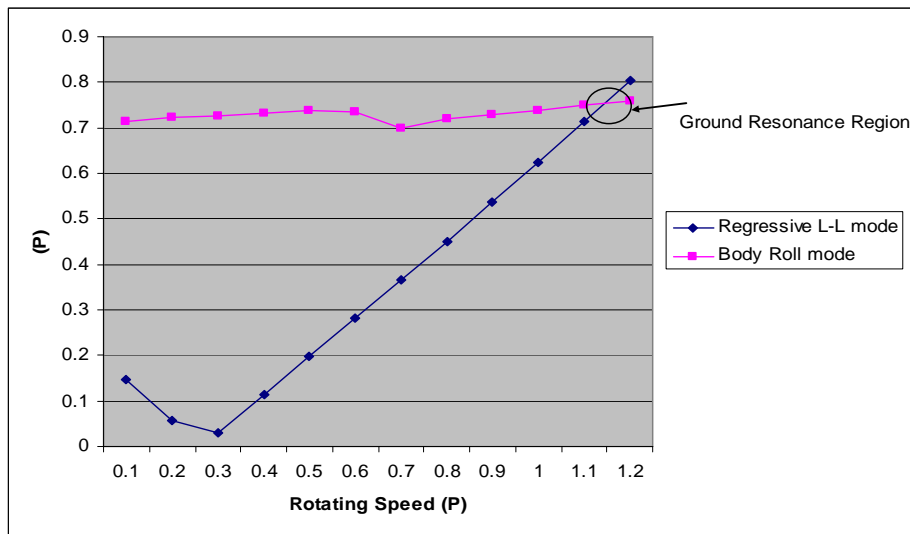


Figure 31: Ground Resonance Plot

#### 4.4.7 Air Resonance

As previously mentioned, the potential for air resonance is virtually eliminated when the lead-lag frequency is well below 0.5P. In order to provide further justification, an air resonance model was developed to calculate the angular momentum of the vehicle that results from in-plane rotor excitations during flight. At the instant that the disturbance is applied, it is assumed that the centrifugal force of each rotor blade momentarily acts parallel to surface reference frame. Making a small angle assumption and using the mass properties and dimensions of the Rambler's rotor, the angular momentum equation was solved for the angular velocity. The results indicate that air resonance condition was likely

$$\begin{aligned}
 I_p \ddot{\theta} &= -mgl \sin \theta - 2\overline{M}\overline{R}\Omega^2 \overline{R} \sin \theta & \frac{M}{\theta} &= k(\Omega) \\
 I_p \ddot{\theta} + mgl \sin \theta + 2\overline{M}\overline{R}\Omega^2 \overline{R} \sin \theta &= 0 & \frac{mgl + k\theta}{I_p} & \\
 I_p \ddot{\theta} + (mgl + 2\overline{M}\overline{R}\Omega^2 \overline{R})\theta &= 0 & \overline{R} &= 0.6R \\
 \omega^2 &= \frac{mgl + 2\overline{M}(\overline{R})^2 \Omega^2}{ml^2} & &
 \end{aligned}$$

**Figure 32: Air Resonance Equations**

---

to occur at 1.24P – a value outside of the normal operating envelope of the Rambler. If the need for lead-lag dampers can be removed, then a significant recurring cost for current helicopters would be eliminated.

#### **4.4.8 Rotor Noise Considerations**

As a training helicopter that is expected to operate in close proximity to the local populace, the minimization of rotor noise was considered as an important design goal. Because the main rotor tip speed is a critical factor in determining the operational noise level of a given helicopter, a conservative value of 650 fps was selected. Although a higher tip speed of 750 fps was the optimum value for aircraft performance as indicated by the preliminary sizing tool, a speed of 650 fps was evaluated as an acceptable compromise for the sake of overall rotor noise. At tip speeds lower than this value, the vehicle's performance suffered too greatly to justify the noise advantages. Specifically, the reduced blade lift coefficient needed for hover flight and the reduced blade inertia necessary for safe autorotation became limiting factors. In addition to the noise advantages, reducing the tip speed to 650 fps also has the advantage of keeping the advancing blade outside of the range of the critical Mach number for the airfoil, reducing the potential for shocks waves on the airfoil surface and the associated power increase required to compensate for the drastic increase in sectional drag.

## **5 Tail Rotor and Empennage Design**

### ***5.1 Configuration Trade Study***

A conventional tail rotor anti-torque system was selected for this design for its overall simplicity and to maintain “typical” flight characteristics in the yaw mode to support its role as an effective training tool. During initial sizing, an optimization code was included to examine the benefits of using an un-symmetric airfoil design and a canted tail rotor configuration. While neither of these considerations caused a significant impact on the overall vehicle weight, they did demonstrate an influence on vehicle performance. For airfoil selection, the main consideration was production of maximum thrust due to stringent hover requirements. During hover operations, the tail rotor must operate at a high power setting in order to counteract the main rotor torque and also provide complete heading control. Therefore, a symmetric airfoil design would have to operate at a higher angle of attack ( $\alpha$ ) in order to produce the necessary thrust. A cambered airfoil, however, needs less angle of attack, and modern designs have lower drag coefficients ( $C_d$ ) and higher maximum lift coefficients ( $C_l$ ) than symmetric airfoils. This results in the potential for higher tail rotor thrust and less power required as compared to a symmetric airfoil. Therefore, the VR-7 airfoil section was used for the tail rotor.

---

A canted design was also considered for the tail rotor in order to take advantage of the additional lift offered by the thrust angles of such a configuration. Because of the sine-cosine relationship, there is potential for a significant gain in vertical lift without losing heading control thrust. One major disadvantage of this is a coupled pitching moment that results when the pilot applies yaw control input. Specifically, for left pedal applications, the nose would pitch down; whereas for right pedal applications, the nose would pitch up. This is unacceptable for any training helicopter, and although the flight controls could be rigged to compensate for this effect, it would only be trimmed for a single airspeed condition unless an electronic augmentation system was incorporated thus adding to cost and complexity. Therefore, a canted tail rotor configuration was not selected.

## ***5.2 Tail Rotor Sizing***

The dimensions of the Rambler's tail rotor were initially calculated using the  $R_f$  Excel preliminary sizing tool and GTPDP to include sideward flight up to 35 knots. The length of the tailboom was based on the assumption it was 20% longer than the main rotor radius. These initial estimates were then examined using stability and control analysis in Section 8 of this report.

## ***5.3 Vertical Fin***

The vertical fin offloads the tail rotor in forward flight, providing better directional stability. For the Rambler design, the dimensions of the vertical fin were based on representative aircraft from this weight class. It is attached directly to the tailboom on the right side of the aircraft, opposite the tail rotor, and it provides the mounting structure to support the loads of the horizontal stabilizer. The Rambler's vertical fin also includes a "tail stinger" attachment to prevent the tail rotor from striking the ground during in-ground-effect hover operations and low-level deceleration maneuvers. Stability and control characteristics were also included in sizing the vertical tail.

## ***5.4 Horizontal Stabilizer***

The location of the horizontal stabilizer and its effect on Rambler's overall pitch stability was the source of much consideration. Three potential mounting options were investigated: along the tailboom within the rotor radius, along the tailboom outside the rotor radius and on the vertical fin. The first option can cause significant reduction in hover performance due to download effects associated with its location under the rotor wake. This location also has a shorter moment arm requiring the aerodynamic surface to be larger, thus, heavier. An advantage, however, is that the vehicle does not experience sudden changes in download caused by wake impingement because the stabilizer is within the rotor wake from hover into forward flight.<sup>11</sup> The second option, offers performance advantages in hover because the download effect

---

is avoided and the longer moment arm allows reduction in size. The drawback of this is that sudden changes in downloading due to the main rotor downwash can occur when the vehicle transitions from hover to forward flight and vice versa. In a training helicopter, this potentially dangerous flight characteristic is unacceptable. The last option offered advantages of the longest moment arm and thus, a lightweight configuration. Its location at the extreme end of the tailboom eliminates the potential for sudden download effects at all transitional flight speeds. Although attaching the stabilizer to the vertical fin requires its structure to be stronger, this was considered acceptable. Therefore, this option was selected as the best alternative for the Rambler, closely resembling the configuration used on the Robinson R-22.

## ***5.5 Empennage***

The design of the Rambler's tailboom was centered on providing a structure capable of supporting the loads of the tail rotor, horizontal stabilizer, and vertical fin. A composite structure was selected for the tailboom for weight savings and better integration with the composite fuselage structure. The tail rotor drive shaft was located on top of the main tailboom structure and protected from debris by a simple sheet metal cover – offering unlimited access to the tail rotor drive shaft and hanger bearings for maintenance operations and preflight inspections.

## **6 Propulsion System Design**

See the Table of Physical Data for performance ratings and Diagram Sheet 3 for a detailed centerline schematic of the engine.

### ***6.1 Design Scope***

In order “to penetrate the piston engine market, it was necessary to convince airframers that the turbine engine's higher cost and lower fuel economy would be offset by its ability to provide greater airspeed, altitude and payload capability, higher reliability and longer TBO.”<sup>15</sup> The challenge of this propulsion system design lies in developing a turbine engine that maintains its performance advantages over piston engines while reducing manufacturing cost, thus making it a viable alternative. However, this goal of achieving a significant reduction in manufacturing cost is further complicated by the challenges of producing the turbomachinery required to efficiently operate the thermodynamic cycle. The manufacturing tolerances of compressor and turbine blades are critical in influencing the component's overall efficiency due to tip loss factors and secondary flows. As the size of the engine is reduced photographically, the tip clearances on rotating components do not scale with the same relative reduction ratio.<sup>16</sup> Additionally, material thickness requirements become a limiting condition because as component

sizes get smaller, the associated materials must maintain a minimum thickness level. To gain insight into the current level of technology for small turboshaft engines, an examination of the current trends in industry was conducted for four key turbine engine design parameters depicted in Figure 33.

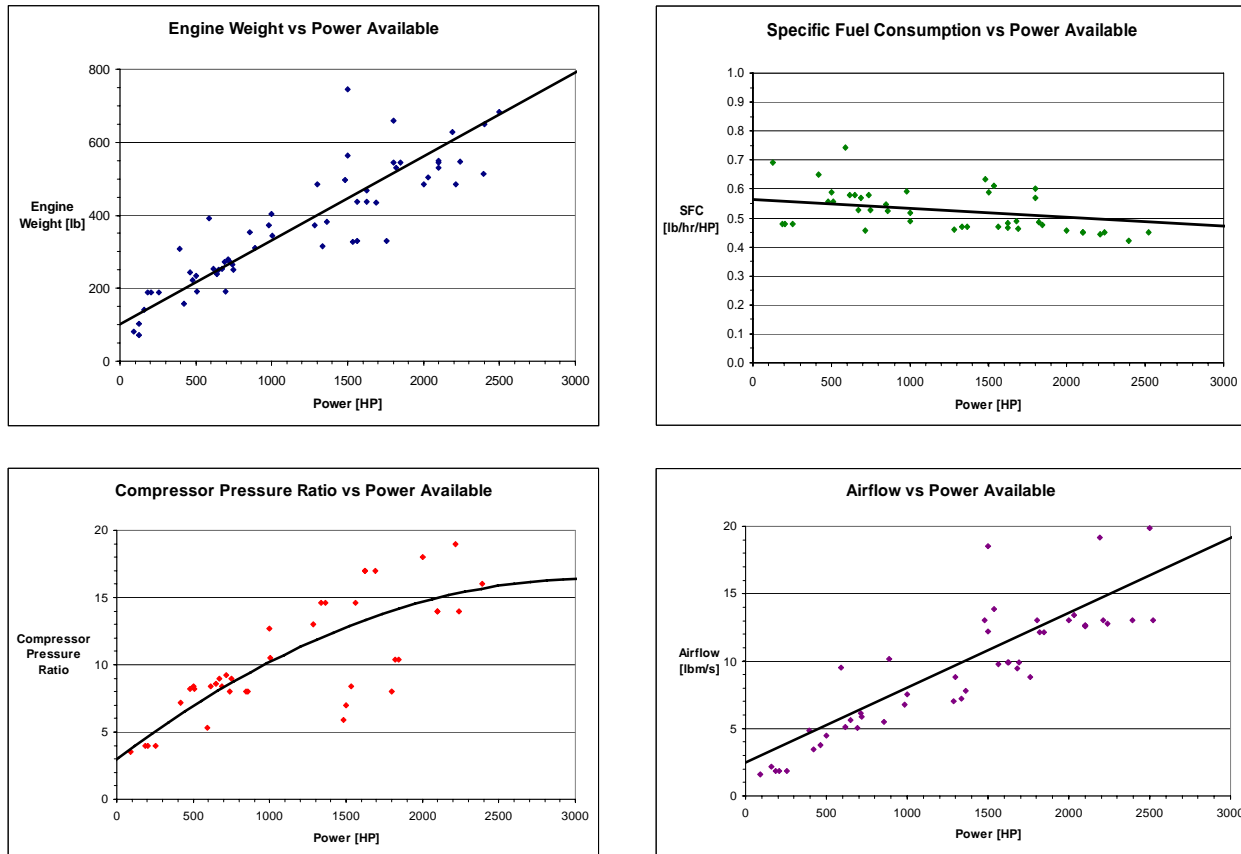


**Figure 33: Current Industry Trends for Key Turbine-Engine Design Parameters**

These graphs are based on the data available from the 2005 Outlook and Specification Report for Gas Turbine Engines in *Aviation Week and Space Technology*.<sup>17</sup> Based on these trends, realistic starting point estimates for the values of engine weight, specific fuel consumption, compressor pressure ratio, and airflow, could be generated as a function of the power available.

## 6.2 Parametric Cycle Analysis

In beginning this engine design process, “the object of parametric cycle analysis is to obtain estimates of the performance parameters in terms of design limitations, the flight conditions, and design choices.”<sup>18</sup> At this stage the engine is considered to be a “rubber” engine whose size and performance characteristics are scaleable to meet the mission requirements.<sup>18</sup> The “on-design” point for a given engine typically represents the point in its operational envelope that either is most demanding, most prevalent, or both – and, therefore, is the most important point to be optimized. The “on-design” point was selected as

the requirement to HOGE at an altitude of 6,000 feet with ISA+20°C atmospheric conditions for up to 2 hours. Not only does this represent an extremely demanding flight condition for any small helicopter, but the time requirement forces the engine to operate at or below its maximum continuous power setting. After selecting the “on-design” point, the engine was modeled as a simple two-spool turboshaft – this free power turbine design provides increased operational flexibility in allowing separate optimization of both the shaft speeds of the compressor and the power turbine.<sup>19</sup> This improves the overall efficiency of the dual-spool design over its single-spool counterpart; and, because it is commonly used on helicopter engines, the impact on manufacturing cost for the added design complexity is minimal.

Initially, a “back-of-the-envelope” approach was adopted to investigate the ideal Brayton Cycle. An Excel code was written to study the effects of varying compressor pressure ratio, airflow, and turbine inlet temperature (T4) on engine efficiency and work output. A key result from analyzing these simplified equations was to identify that it is impossible to simultaneously maximize specific power output and thermal efficiency of an engine as each occurs at a different pressure ratio.<sup>19</sup> The “on-design” point was then evaluated using GasTurb 10, a more sophisticated engine software. It was used for numerous parametric studies in evaluating the “real” Brayton Cycle, incorporating non-ideal component efficiencies to realistically model actual engine performance. Conservative values for the appropriate component polytropic efficiencies and pressure losses of the compressor, combustor, and turbine sections were based on an assumption of level 3 technology (years 1985-2005), as depicted in Table 7:

**Table 8: Component Technology Level Assumptions<sup>18</sup>**

Component	Figure of Merit	Type	Level of Technology			
			1	2	3	4
Compressor	$e_c$		0.8	0.84	<b>0.88</b>	0.9
Burner	$\pi_b$		0.9	0.92	<b>0.94</b>	0.96
	$\eta_b$		0.88	0.94	<b>0.99</b>	0.995
Turbine	$e_t$	Uncooled	0.8	0.85	<b>0.89</b>	0.91
		Cooled		0.83	0.87	0.89

Using these values, a parametric study was performed to determine the optimum settings for compressor pressure ratio and T4. The results of this analysis are shown in Figure 34. The carpet plot above depicts the simultaneous effects of increasing the pressure ratio from 2:1 to 10:1 and increasing T4 from 2000°R to 2700°R on engine SFC and work output. The trends show that increases in both reduce engine SFC and increase work output. It is also apparent that there is a point of diminishing returns for each increasing factor. Specifically, at pressure ratios above 7:1 and temperatures above 2400°R, the relative reduction in engine SFC begins to reduce. In terms of shaft power output, the higher pressure

ratios considered provide minimal benefit, whereas, higher T4 clearly have an advantage in terms of extracting more work from a given flow.

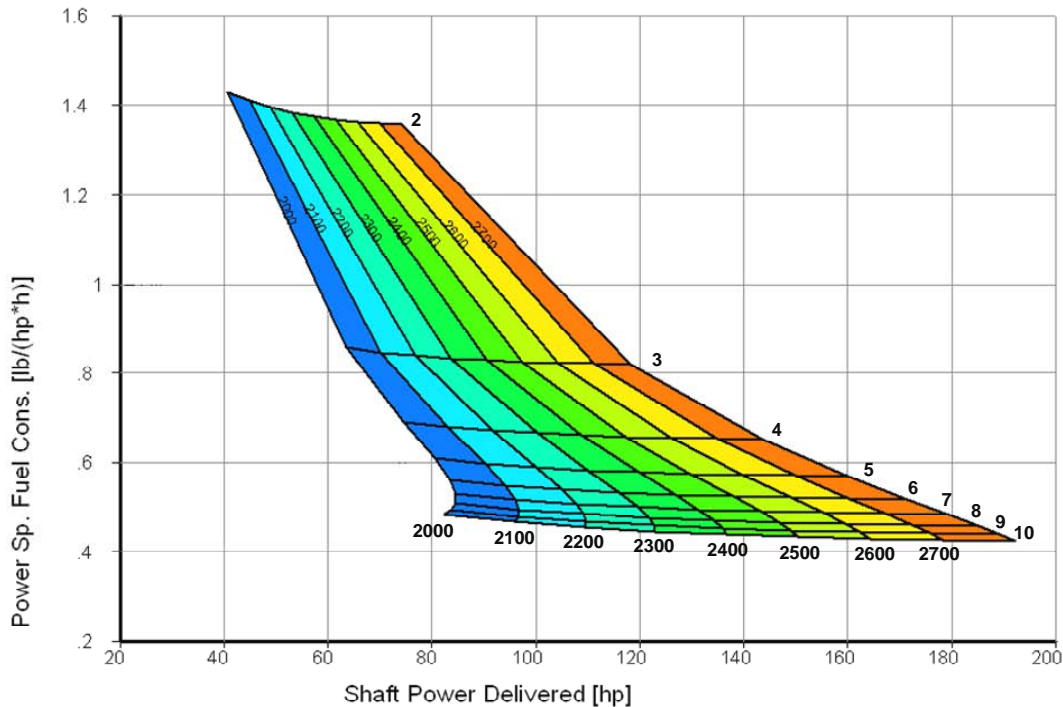


**Figure 34: “On-Design” Point Parametric Analysis**

### 6.2.1 Turbine Cooling Trade Study

The benefits of increasing T4 do not come without penalty as at temperatures above 2300°R, (1278°K) the turbine blades require cooling airflow to maintain material integrity. Figure 35 demonstrates the relationship between T4 and required turbine cooling as a function of the current level of technology. A trade study was conducted to determine if the benefits of increasing T4 above 2300°R are worth the increased design complexity required to cool the turbine blades. Since the power output requirements for a small training helicopter are relatively less important than its overall operating efficiency, SFC was used for evaluation. In order to calculate the percentage of bleed air required to effectively cool the turbine blades at a given temperature, an Excel code was written to evaluate the turbine cooling algorithm described in the NASA Technical Memorandum 81453.<sup>20</sup> Figure 36 shows the effect of increasing T4 from 2300°R to 2900°R on engine SFC. It was concluded that reduction in SFC, less than 0.01 lb/HP/hr, did not outweigh the added manufacturing cost for providing cooling air to the turbine blades. The added cost would be compounded by the small size of the turbine blades required for this specific engine design.



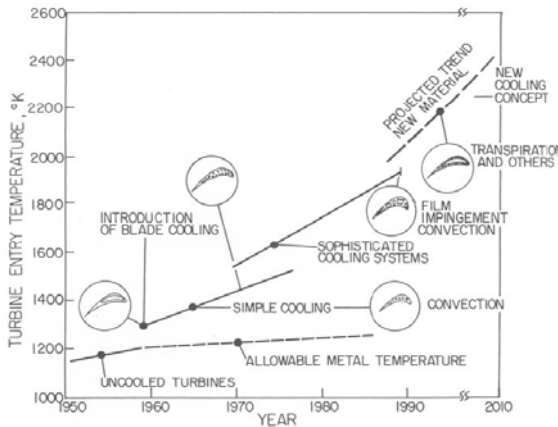


Figure 35: Turbine Cooling Technology Assessment <sup>21</sup>

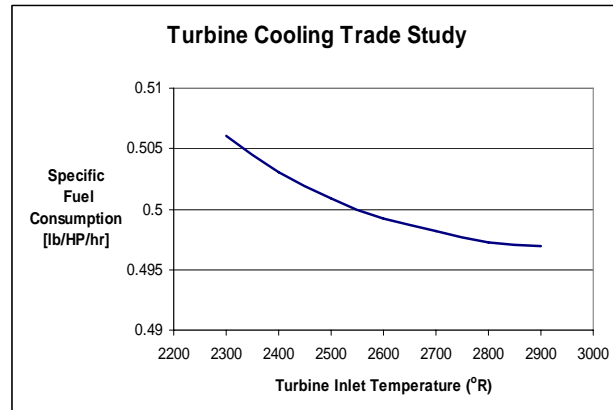


Figure 36: Turbine Cooling Trade Study

## 6.2.2 Parametric Cycle Analysis Conclusions

Optimizing the engine “on-design” performance was an iterative process based on the helicopter’s varying aerodynamic performance. The baseline vehicle design was continually being updated and refined to reflect the analysis completed by each individual design discipline. Ultimately, a power required value of 120 HP was determined as the necessary engine output. Given the maximum T4 as 2300°R and the component efficiencies described in Table 1, the optimization feature of GasTurb 10 was used to determine the optimum settings for airflow (1.04 lbm/s) and pressure ratio (6.5:1) that would minimize the engine’s SFC with an output of 120 HP.

## 6.3 Performance Cycle Analysis

In order to achieve greater accuracy and detail than offered by the GasTurb 10 program for the “off-design” performance, a model using the NASA Engine Performance Program (NEPP) was developed. NEPP, originally developed and used as the primary aircraft engine analysis tool at NASA-Lewis Research Center, utilizes a FORTRAN code to calculate 1-dimensional, steady-state thermodynamic performance for gas turbine engines.<sup>22</sup> Figure 37 depicts the initial model used in NEPP.

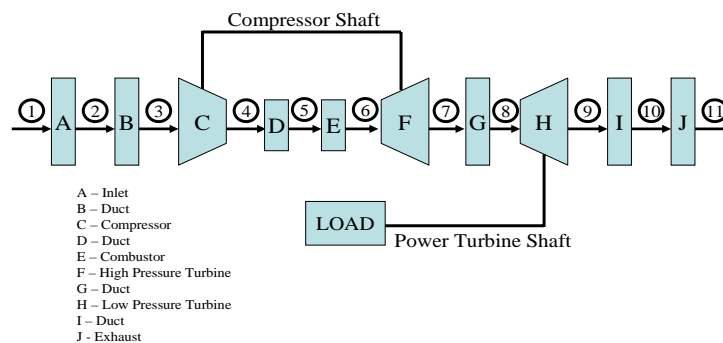


Figure 37: NEPP Engine Model

As the figure demonstrates, the NEPP model consists of a series of components linked by station properties that describe the flow properties at the entrance and exit of every component. The individual properties of each physical component are included in the input code – this code also ensures that the engine is properly arranged to model the desired flowpath. The NEPP input file includes non-physical components which are used to “control, optimize, limit, and schedule engine variables.”<sup>22</sup> The user can define the appropriate engine flight conditions for the specific “off-design” points being evaluated. Typically, these inputs consist of a series of changing altitude, airspeed, and throttle settings in order to capture the engine’s performance characteristics throughout its entire operational, or flight, envelope.

The flight envelope for this training helicopter was an airspeed ranging from hover to Mach 0.2 (132 knots at SLS) and an altitude ranging from sea-level to 12,000 feet. 12,000 feet was selected as a reasonable maximum altitude for a small training helicopter because the effects of reduced oxygen at altitudes any higher can begin to impair a pilot’s responsiveness. FAA Regulations stipulate that all aircraft crewmembers operating above 14,000 feet altitude, or above 12,500 feet altitude for a period of more than 30 minutes, must have supplemental oxygen available. The NEPP model did not support the evaluation of negative airspeeds to simulate rearward flight and therefore these flight conditions were not considered part of the operational flight envelope. Although a rearward flight profile up to 20-30 knots is possible in a small training helicopter, its influence on engine performance was assumed to be negligible.

### **6.3.1 Component Performance Maps**

In addition to establishing the flight envelope, the “off-design” analysis in NEPP also required the use of “maps” to better describe the thermodynamic performance of each individual component over its actual range of operation.<sup>18</sup> For the conceptual level of detail required on this project, a collection of various tools and methods was used to produce a set of approximated component maps for the compressor and turbine sections only. The details of these maps will be covered later in this report. For this analysis, a constant level of combustion efficiency and pressure loss were considered adequate.

## ***6.4 Component Design Considerations***

### **6.4.1 Compressor Configuration Selection**

An examination of preliminary compressor and turbine component design was undertaken with the intent of providing a “feasibility” check for the parameters used throughout the engine cycle analysis. Since the engine cycle analysis revealed that the optimum compressor pressure ratio for this application was 6.5:1 at the “on-design” point, consideration had to be given to determining the optimum compressor configuration that would achieve such results and maintain design simplicity. Although axial compressors

show better efficiency when compared to centrifugal compressors, at mass flow rates below 3 lbm/s, the latter is more efficient due to its lower sensitivity to effects of blade tip clearance.<sup>16</sup> In engines with extremely low mass flow rates, axial compressors also exhibit another problem with manufacturability of the last compressor stages as the blade tips can become too short.<sup>19</sup> Therefore, a single-stage centrifugal compressor configuration was selected in order to take advantage of the relative increased efficiency and overall design simplicity. As per a discussion with Dr. David Eames of Rolls-Royce North America on compressor design, the assumption that a single-stage radial compressor can achieve a 6.5:1 pressure ratio was considered reasonable.

### 6.4.2 Centrifugal Compressor Design

In order to determine the geometric and performance characteristics of a centrifugal compressor, an Excel code was written to mirror the sample problem calculations and techniques described in *Introduction to Turbomachinery*.<sup>23</sup> An iterative process of solving the entrance velocity triangle by guessing the inlet Mach number at the tip,  $M_{1t}$ , and then continuously calculating a new value for  $M_{1t}$  until the two converge, was used. The exit velocity triangle was calculated using the same iterative process for the exit Mach number,  $M_{3t}$ . The Wiesner correlation was also used to estimate the exit slip factor,  $\sigma$ , defined as the ratio of exit swirl velocity to the rotor speed, as shown in Equation 3:

$$\sigma = 1 - \frac{\sqrt{\cos(\beta_{b2})}}{Z^{0.7}} \quad \text{Equation 3}$$

where  $\beta_{2b} = 0$  for high speed impellers and  $Z$  is defined as the number of blades.<sup>23</sup> By using the exit dimensions and flow conditions of the axial compressor as the entrance conditions for the centrifugal compressor, a preliminary design that would meet the necessary stage pressure ratio requirements was determined. A conservative polytropic efficiency of 85% was assumed to account for the increased losses associated with turbomachinery of this size. Figure 38 shows the component map used for the centrifugal compressor, depicting efficiency and pressure ratio as a function of corrected flow and corrected speed.

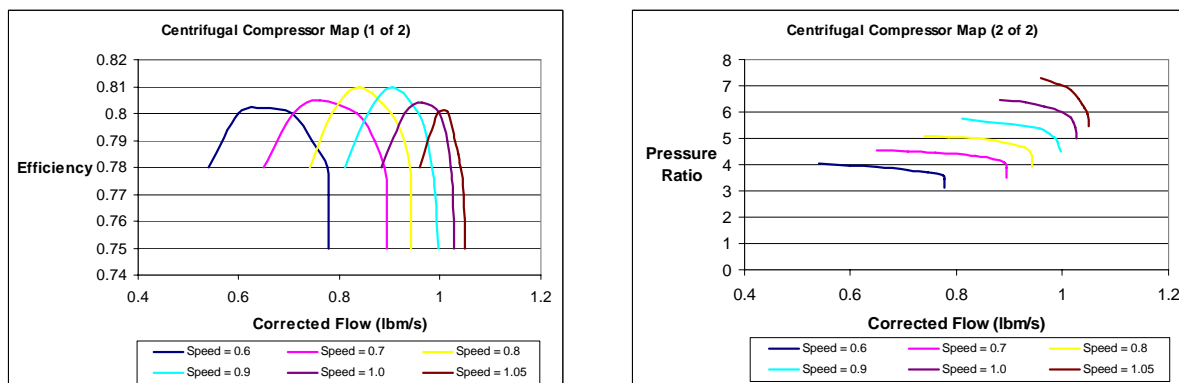


Figure 38: Centrifugal Compressor Performance Map

### 6.4.3 Turbine Section Design

Using Turbine Preliminary Design Program (TURBN), a program within Mattingly's *Aircraft Engine Design* textbook software suite, initial sizing and performance characteristics for both the high pressure and power turbines were completed. The engine output data from NEPP provided the required input. The following assumptions were made: two-dimensional flow, constant axial velocity, constant mean radius, adiabatic flow in the rotor and stator and calorically perfect gas.<sup>18</sup> The assumption of 89% polytropic efficiency was made for both turbines based on the reference in Table 1 of this report. Table 8 summarizes the results for this single stage high pressure and single stage low pressure turbine design. The material selection for the both turbine disks was based on an analysis of the blade stress factor,  $AN^2$ , and their shaft speeds. For the high pressure turbine, a shaft speed of 60,000 RPM was selected in order to achieve a design balance between the competing demands of compressor performance and maximum turbine blade stress. At speeds higher than 60,000 RPM the high pressure turbine blade stress increases to a level that exceeds its uncooled material limitations.

**Table 9: Turbine Design Parameters**

		HPT	LPT	Units
Stage Efficiency	$\eta_s$	0.900	0.882	
Stage Pressure Ratio	$\pi_s$	2.40	1.29	
Inlet Temperature	$T_4$	2300	1922	$^{\circ}R$
Hub Radius	$r_h$	1.86	3.60	in
Tip Radius	$r_t$	2.14	3.90	in
Hub-to-Tip Ratio	$r_h/r_t$	0.87	0.92	
Reaction	$^{\circ}R_c$	0.54	0.55	
Loading Coefficient	$\psi$	2.57	2.79	
Flow Coefficient	$\phi$	1.01	1.07	
Blade Stress Factor	$AN^2$	8.00E+09	4.34E+09	$in^2 RPM^2$
Material		DS Superalloy	Nickel Alloy	

For the low pressure turbine, a shaft speed of 30,000 RPM was selected as the optimum value for balancing the demands of material selection and turbine performance. This slower speed allows the use of less expensive materials while maintaining a high level of stage efficiency. Figure 39 demonstrates the relationship between the blade stress factor,  $AN^2$ , and material specific strength for the high pressure and low pressure turbines at an assumed taper ratio of 1.0. The graph indicates that the required specific strength is approximately 700  $psi/(slugs/ft^3)$  for the high pressure turbine and 400  $psi/(slugs/ft^3)$  for the low pressure turbine. These values were used on the graph in Figure 40 to determine the turbine materials required to meet the high temperature demands. This plot shows that the high pressure turbine should be constructed from "Material 5" which refers to a single-crystal or directionally solidified (DS) superalloy

and the low pressure, or power, turbine should be constructed from “Material 3” which refers to a wrought nickel alloy.

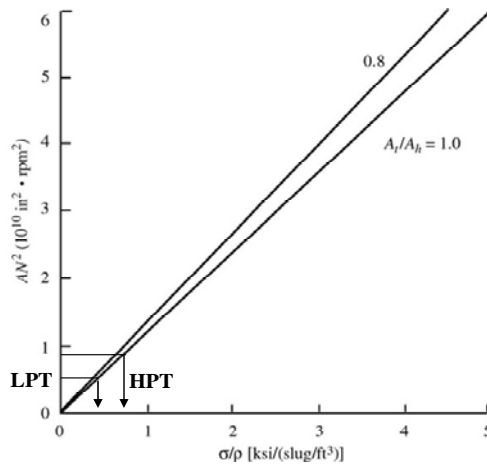


Figure 39: Blade Stress vs. Specific Strength<sup>18</sup>

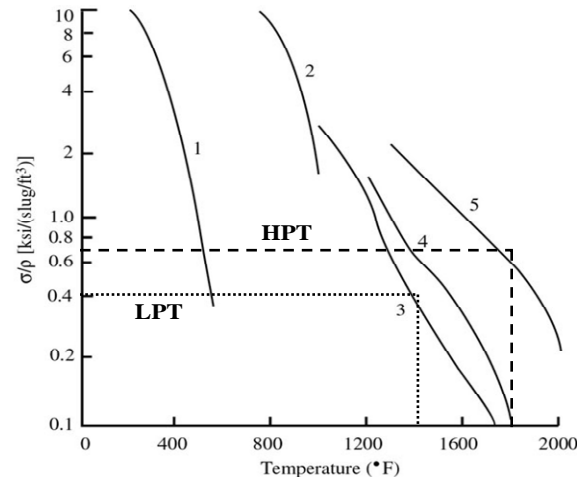


Figure 40: Turbine Material Selection Plot<sup>18</sup>

For the turbine performance map, the parameters typically used are total pressure ratio, corrected mass flow rate, corrected engine speed, and adiabatic efficiency. A combination of tools was used to generate both the high pressure turbine (HPT) and power turbine (PT) maps for this project. GasTurb 10 was used to produce the scaled turbine maps; however, instead of manually converting this graphical output into the format needed for NEPP, a NASA program known as the Extended Parametric Representation of Turbines (PART) was used to produce the maps in the proper NEPP format using the input data from GasTurb 10.<sup>24</sup> Figures 41 and 42 show turbine performance maps for the HPT and PT.

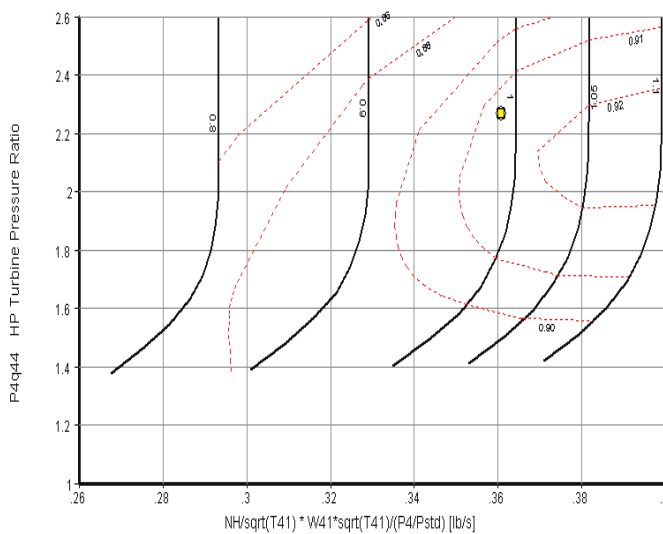


Figure 41: High Pressure Turbine Performance Map

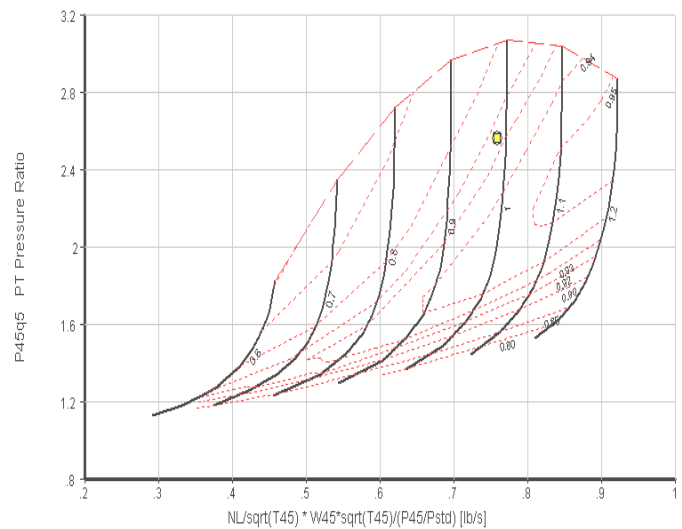


Figure 42: Power Turbine Performance Map

Using these inputs into NEPP, the performance cycle analysis was conducted iteratively with the vehicle sizing and performance code. Both the  $R_f$  Excel program and GTPDP incorporated an engine model to more accurately predict the fuel and power requirements at changing altitudes. This model was refined and updated to reflect the changing engine performance characteristics until a final solution was achieved that most effectively satisfied the performance requirements with the lowest SFC.

#### **6.4.4 Combustion Section Design**

A reverse-flow cannular combustor design was selected for this engine configuration. This design provided the most efficient optimization of space within the engine's core. The increased frontal area required for the centrifugal compressor stage allowed the reverse-flow cannular combustor to be located outside of the high pressure turbine's radius. For a preliminary sizing estimate, the dimensions of an existing combustor design were linearly reduced in order to determine the appropriate scale for this engine application.<sup>25</sup> The technology level assumptions of a combustor efficiency of 99% and a combustion pressure drop of 6%, described in Table 1 of this report, were used within the NEPP model.

#### **6.4.5 Modular Gearbox Design**

A modular approach was used in the design of the engine gearbox in order to capitalize on increased marketability. Two separate gearbox configurations, turboshaft and turboprop, are designed to provide greater flexibility in using the engine for both rotary-wing and fixed-wing applications. The turboshaft engine gearbox provides a 5:1 reduction ratio for the main drive shaft and a 5.8:1 reduction ratio for the tail rotor drive shaft. This gearbox configuration extends below the engine core to provide clearance for the tail rotor drive shaft (See Diagram Sheets 2 and 4). The turboprop gearbox does not include the gear reduction for tail rotor driveshaft and, therefore, maintains a smaller cross-sectional size better suited for fixed-wing applications.

The material selected for the gears is case hardened steel or VASCO X2M. It exhibits high strength, high hardness, high temperature capability, while maintaining light weight properties relative to other steels.<sup>26</sup> An additional gear reduction ratio of 4:1 was included in the engine gearbox for the starter configuration and was connected to the compressor shaft. Through the use of a starter-generator and battery power, the compressor can be operated during the engine starting sequence to initially provide the necessary air compression for successful combustion.

In order to meet autorotational requirements inherent to any helicopter gear train design, a freewheeling unit with a sprag clutch was also incorporated into the connection between the power turbine shaft and the engine gearbox. This component "provides the means to disconnect the power train from a failed or secured engine."<sup>27</sup> The engine drives an outer gear ring which engages an inner gear ring

connected to the rest of the engine gearbox during normal powered operation. In the event of an engine failure, the outer gear ring will stop, allowing the inner gear ring to continue rotating. This mechanical design allows both the main rotor and tail rotor to continue in autorotation following an engine failure.

## 6.5 Specifications and Performance Analysis

Using the maximum continuous power (MCP) setting for sea-level standard conditions of 152 HP calculated using NEPP, it was necessary to establish an estimated value for the 5-minute maximum takeoff power requirement as stipulated in Federal Aviation Regulation (FAR) Part 27. Equation 4 was used to estimate this short duration power:

$$HP_{SD} = HP_{NR} (1 + 0.252 e^{-0.0173t}) \quad \text{Equation 4}$$

where  $HP_{NR}$  refers to normal rated power (replaced by MCP) and  $t$  is the time in minutes.<sup>7</sup> Based on these results, the NEPP model was updated to reflect the increased throttle settings required to generate the increased power demand by allowing the turbine inlet temperature to increase from 2300°R at the MCP setting to 2450°R for the 5-minute takeoff power setting. Figures 43-48 depict the overall engine performance throughout its full operational envelope and at varying atmospheric conditions:

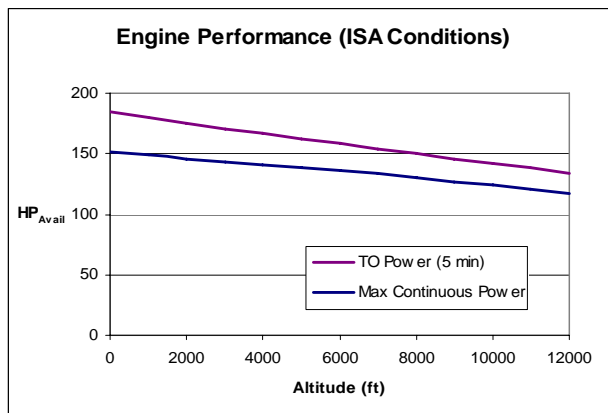


Figure 43: HP Available vs. Altitude (ISA)

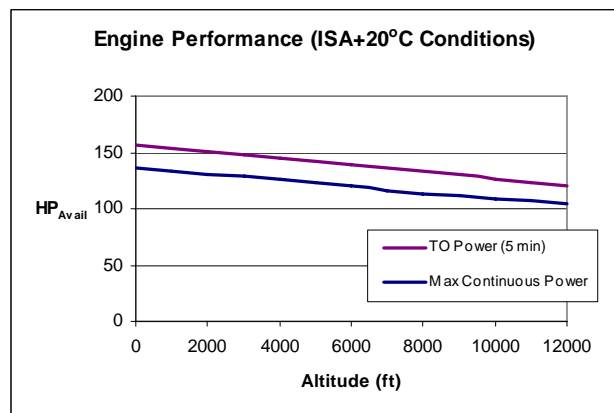


Figure 44: HP Available vs. Altitude (ISA+20°C)

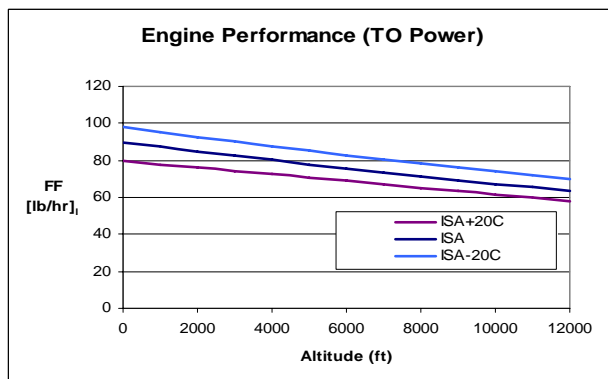


Figure 45: Fuel Flow vs. Altitude (TOP)

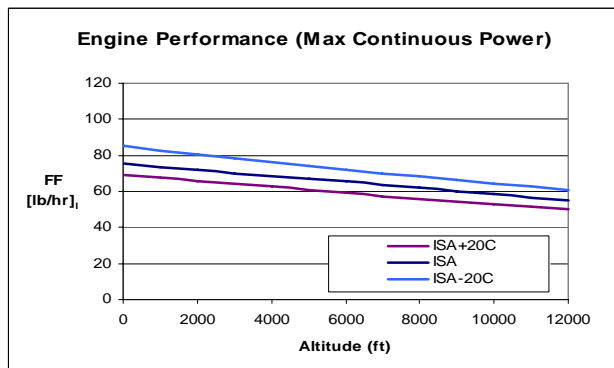


Figure 46: Fuel Flow vs. Altitude (MCP)

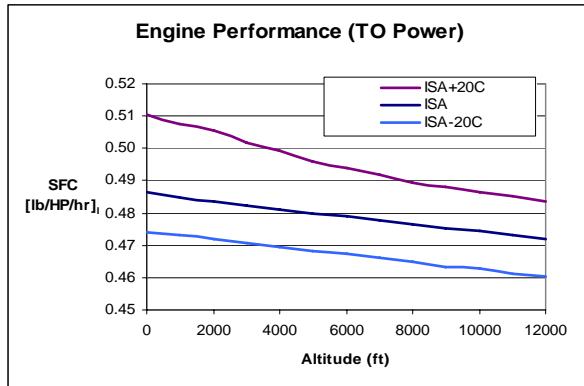


Figure 47: SFC vs. Altitude (TOP)

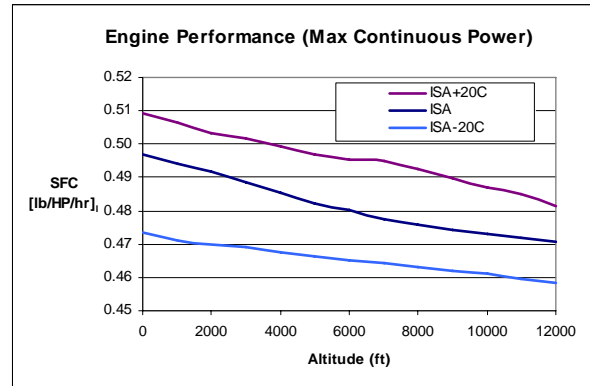


Figure 48: SFC vs. Altitude (MCP)

## 6.6 Weight Analysis

CATIA was used to determine the specific volume of each major engine component. These values were then evaluated as a function of their material density to determine an estimated weight breakdown. Table 9 summarizes the results of this analysis.

Table 10: Engine Component Weight Breakdown

Component	Volume (in <sup>3</sup> )	Density (lb/in <sup>3</sup> )	Weight (lb)
Compressor	35.20	0.170	6.0
Combustor	18.60	0.283	5.3
High Pressure Turbine	12.97	0.298	3.9
Low Pressure Turbine	24.06	0.298	7.2
Compressor Shaft	11.88	0.298	3.5
Power Turbine Shaft	7.58	0.276	2.1
Gearbox	220.96	0.283 / 0.098	51.9
Housing	141.99	0.283	40.2
<b>Total Weight</b>			<b>120.0</b>

## 6.7 Manufacturing

The small sizes of the engine's rotating components require the use of state-of-the-art manufacturing technologies in order to achieve the close material tolerances needed for high efficiency. For the centrifugal compressor, a Computer Numerically Controlled (CNC) five-axis milling machine will be used to precisely machine its complex geometry. The tool path programs which define the intricacies of the cutting motions are easily generated using a suite of CAD/CAM software. As future improvements are made in the aerodynamic design of the radial compressor using computational fluid dynamics (CFD) analysis, the five-axis milling machine can immediately update its tool paths to capture



the design upgrades without an engineering compromise for manufacturability. This integration between the design and manufacturing steps increases both process efficiency and component efficiency.

The turbine section of the engine will utilize directional solidification to produce the high pressure turbine blades with a vacuum chamber casting process. By closely controlling the temperature of the casting process, directional solidification results in a turbine airfoil composed of columnar grains along its spanwise axis. This grain alignment strengthens the blade and effectively eliminates the potential for destructive intergranular crack initiation.<sup>28</sup> Although more expensive to manufacture, the structural benefits offset this cost by reducing the long term maintenance requirements of the engine's turbine section. Directionally solidified superalloys exhibit increased ductility and fatigue life which will lengthen the time between overhaul (TBO) for the entire engine. For the low pressure turbine, which experiences lower relative temperatures, an integrally cast turbine wheel and blades will be used in order to reduce part count, manufacturing time, and overall complexity.

## 6.8 Federal Aviation Regulations (FAR) Requirements

A new engine design is subject to the Code of Federal Regulations, Title 14 – Aeronautics and Space, Chapter 1 – Federal Aviation Administration, Subchapter C – Aircraft, Part 27 – Airworthiness Standards: Normal Category Rotorcraft and Part 33 – Airworthiness Standards: Aircraft Engines. Beginning with Part 27, this regulation lists numerous requirements in Subpart E – Powerplant, Table 10 highlights those that are applicable at this conceptual level of engine design:

**Table 11: FAR Part 27 Engine Requirements**

Para.	Title	Summary
27.907	Engine Vibration	Engine and rotor drive system must be free from excessive vibrations – Transmission mounted with dampers to eliminate excessive vibrations due to the rotor
27.917	Rotor Drive System Design	Engine must automatically disengage from rotor drive system for autorotational capability – Freewheeling unit installed in engine gearbox
27.1091	Air Induction	Inlets must supply the engine with the required air during all operating conditions and minimize the ingestion of debris – Screened engine cowling and inlet barrier filters surround the engine inlet
27.1093	Induction System Icing Prevention	Engine must be capable of operating at all power settings without accumulating ice on the inlet detrimental to engine operation – Engine anti-ice system uses bleed air from the compressor to heat the walls of the engine
27.1141	Powerplant Controls: General	No single point failure in any powerplant control system can cause the loss of a powerplant function necessary for safety – FADEC engine control has an analog backup mode
27.1191	Firewalls	Engine must be isolated from personnel compartments, structures, controls, and rotor mechanisms by a firewall or shroud – Engine compartment is isolated

For Part 33, this regulation is more focused on the specific testing and evaluation requirements used during the certification process of a new aircraft engine. Table 11 summarizes the applicable

requirements from Part 33 for this engine design; testing requirements will be addressed in the certification section of the report.

**Table 12: FAR Part 33 Engine Requirements**

Para.	Title	Summary
33.7	Engine Ratings and Operating Limits	Established relating to horsepower, RPM, gas temperature, and time for MCP and TOP – See engine specifications
33.15	Materials	Suitability and durability must be based on experience or testing – Material selection based on historical experience
33.66	Bleed Air System	If the engine anti-icing can be controlled, a means to indicate its functioning is required – Pilot display light will illuminate when system is active
33.75	Safety Analysis	No probable engine malfunction or improper operation can result in a fire, engine burst, loads greater than ultimate loads, or loss of engine shut down capability
33.76	Bird Ingestion	Not applicable due to the inlet design on this aircraft

## ***6.9 Additional Engine Design Considerations***

### **6.9.1 Control System**

The engine control system used for this design is the Full-Authority Digital Engine Control (FADEC). This system, which is a mainstream component on most new helicopters with turboshaft engines, provides a number of important advantages over more conventional control systems. The system “consists of a digital electronic control unit (ECU), a hydromechanical metering assembly (HMA), which includes a fuel pump and metering section, plus the wiring harnesses that connect the ECU and the HMA to sensors on the engine and airframe.”<sup>29</sup> As a training helicopter, the simplicity of operation of FADEC is its biggest selling point. It provides automatic engine starting capability which virtually eliminates the problems of hot starts and ignition failures common with inexperienced pilots. FADEC is much more responsive to pilot power demands – “the collective can be moved as fast as is physically possible without risking a stall, surge, or damage to the transmission.”<sup>29</sup> This is essential in a training aircraft so that instructor pilots can take immediate corrective actions, without the threat of an over-torque condition. FADEC offers the maintenance benefit of an engine health monitoring system that can monitor and record engine flight data, cycles, and vibration information.

### **6.9.2 Air Filtration System**

The air induction system used for this engine is the Inlet Barrier Filter (IBF) system which offers several performance and maintenance advantages over more traditional particle separator designs. The IBF system is currently in use on light helicopters such as the Bell 206 and MD500. It uses replaceable/reusable filters with a 15 cycle service life equaling over 7,500 hours – reducing both maintenance and DOC. Figure 49 shows the integration of the IBF system on the MD 500 helicopter.

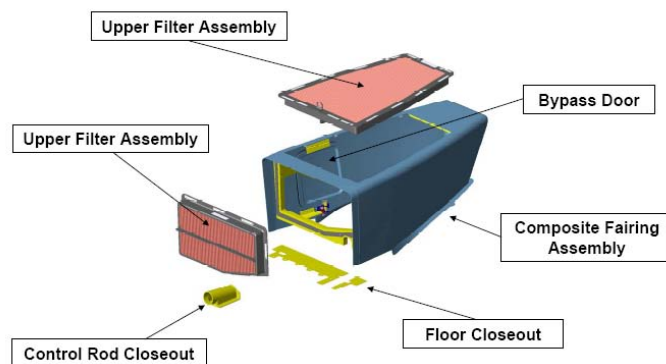


**Figure 49: Inlet Barrier Filter (IBF) System on the MD 500** <sup>30</sup>

The IBF system filters over 99% of the particles in the airflow in order to create a cleaner plenum chamber for the engine inlet – improving engine component protection from foreign object damage (FOD) and overall engine performance by increasing the temperature margin.<sup>30</sup> The only drawback of this system is that it requires the installation of a bypass door to allow unfiltered air to enter the engine in the event that a filter becomes completely blocked. However, the system is designed to provide the pilot with a cockpit indication of an impending bypass condition – allowing several flight hours to take corrective action before a full bypass would be required.

## 6.10 Transmission Design

See Diagram Sheet 4 for a complete drive train schematic.

### 6.10.1 Configuration Selection

Based on the relatively low horsepower output of the Rambler’s new engine, it was determined that a new transmission design would also be required in order to maintain design simplicity and to incorporate potential weight saving measures. For this transmission, a simplified split torque transmission design was selected which demonstrates several key advantages over a more conventional planetary gearbox design. The general configuration of this transmission followed the design presented by Mr. Thomas Hanson in his report, *A Designer Friendly Handbook of Helicopter Rotor Hubs*. The Hanson transmission provided an optimized integration of the hub configuration selected for this vehicle and its propulsion source by minimizing the design complexity and increasing the structural integrity of the overall drive system. The Hanson transmission design utilized a combination of only four main gears to achieve the required gear reduction between the engine and the rotor system and this reduction in parts directly translated to savings in both overall weight and cost. This design also offered a much lower dimensional profile than that of a conventional planetary system which minimized its drag profile and allowed much greater design flexibility in integrating the transmission with the airframe structure. Figure

50 depicts this simplified gearbox configuration and Figure 51 shows a Hanson transmission built as part of his light helicopter and auto-giro prototype projects.

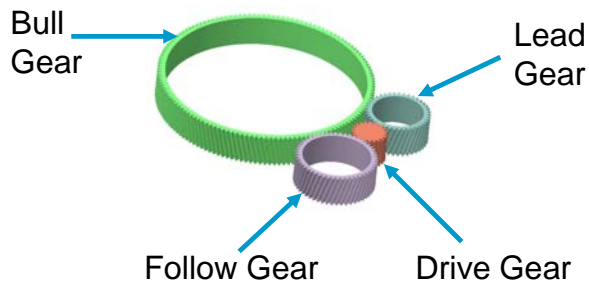


**Figure 50: Hanson Transmission Gears**

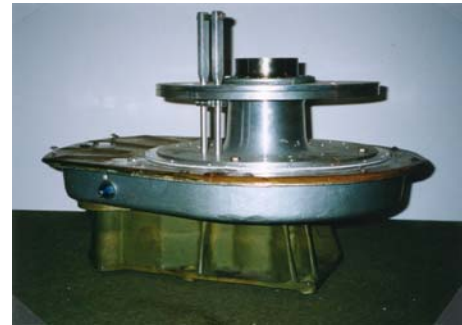


**Figure 51: Actual Hanson Transmission**

The Hanson transmission clearly offered the most robust solution in terms of structural redundancy by using the combination of a rotating and non-rotating mast to transmit loads between the rotor and the fuselage. The short length and large diameter of the rotating mast, which is attached directly to the bull gear, provides “the lightest way to carry the rotor drive torque to the hub.”<sup>1</sup> The non-rotating mast is located inside of the rotating mast with a connection at the base of the transmission housing. This second mast provides structural redundancy in the case of a main rotor shaft failure and protection for the aircraft’s flight controls which are located inside, thus increasing the overall safety of this design.

### 6.10.2 Sizing and Analysis

The Hanson transmission’s individual gears were assumed to be a standard spur gear configuration instead of a helical gear design. Although the helical gear design offers advantages in noise reduction and improved load sharing capacity, the spur gear configuration simplifies the overall design by eliminating the need for thrust bearings because spur gears do not generate axial loads or thrust.<sup>26</sup> Ultimately, this translates to a lighter gearbox with lower manufacturing cost. The reduced capability of spur gears is not a limiting factor because this transmission’s load requirements are relatively small. The following list of initial design conditions and assumptions was used to analyze the individual gear sizing and performance characteristics:

- Maximum transmission power rating  $\geq 200$  HP
- Main rotor rotational speed = 509 RPM
- Engine gearbox output speed = 6,000 RPM
- Transmission gearbox TBO = 3,500 hours

Using these initial conditions, each gear mesh was evaluated to determine the optimum pitch diameter and number of teeth. Table 12 shows the results of this study.

**Table 13: Transmission Gear Sizing**

	Drive Gear	Lead Gear	Follow Gear	Bull Gear	Units
<b>Pitch Diameter</b>	2	3.5	4	12	in
<b>Teeth</b>	16	28	32	96	
<b>Face Width</b>	2.5	2.5	2.5	1	in
<b>Material</b>	----- VASCO X2M Steel -----				

VASCO X2M Steel was selected as the material for these gears for the same reasons listed in the engine gearbox section – its high strength, hardness, and temperature capability relative to other steels. Based on these gear geometries, the contact stress and bending stress calculations were performed using the techniques and procedures presented in CPT Andrew Bellocchio Masters Thesis report.<sup>26</sup> Equations 5 and 6 were used to calculate the contact stress and bending stress for each gear.

$$s_c = C_p \sqrt{W_t K_o K_v K_s \frac{K_m}{dF} \frac{C_f}{I}}$$

**Equation 5: Actual Contact Stress**

Where:

$s_c$  = contact stress (lb/in<sup>2</sup>)  
 $C_p$  = elastic coefficient (lb/in<sup>2</sup>)<sup>0.5</sup>  
 $W_t$  = transmitted tangential load (lb)  
 $K_o$  = overload factor  
 $K_v$  = dynamic factor  
 $K_s$  = size factor  
 $K_m$  = load distribution factor  
 $C_f$  = surface condition factor (pitting resistance)  
 $F$  = net face width (in)  
 $I$  = geometry factor for pitting resistance  
 $d$  = operating pitch diameter of pinion (in)

$$s_t = W_t K_o K_v K_s \frac{P_d}{F} \frac{K_m K_B}{J}$$

**Equation 6: Actual Bending Stress**

Where:

$s_t$  = bending stress (lb/in<sup>2</sup>)  
 $K_B$  = rim thickness factor  
 $J$  = geometry factor for bending strength  
 $P_d$  = transverse diametral pitch (in<sup>-1</sup>)

Results were compared to the maximum working stress values using Equations 7 and 8, where “working” stress refers to the allowable stress corrected for stress cycles, reliability, and temperature effects.

$$s_c \leq \frac{s_{ac}}{S_H} \frac{Z_N}{K_T} \frac{C_H}{K_R}$$

**Equation 7: Working Contact Stress**

Where:

$s_{ac}$  = allowable contact stress (lb/in<sup>2</sup>)  
 $Z_N$  = stress cycle factor  
 $C_H$  = hardness ratio factor  
 $S_H$  = safety factor  
 $K_T$  = temperature factor  
 $K_R$  = reliability factor

$$s_t \leq \frac{s_{at} Y_N}{S_F K_T K_R}$$

**Equation 8: Working Bending Stress**

Where:

$s_{at}$  = allowable bending stress (lb/in<sup>2</sup>)  
 $Y_N$  = stress cycle factor  
 $S_F$  = safety factor  
 $K_T$  = temperature factor  
 $K_R$  = reliability factor

Based on the assumption of a 3,500 hour gear life, the stress cycles experienced by each gear mesh were on the order of magnitude of  $10^8$  total cycles. Therefore, the stress cycle factors,  $Z_N$  and  $Y_N$ , were used to more accurately estimate the effects of fatigue in the life of each gear. The TO power transmission limit was then established by iterating these equations until a limiting power relationship developed in which the actual stress equaled the maximum allowable working stress. As illustrated in Table 13, the lead-bull gear mesh was the limiting configuration with a maximum TO power rating of 203 HP. The maximum continuous transmission power was calculated to be 168 HP based on the assumption of a 10% buffer between the actual stress and the maximum allowable working stress.

**Table 14: Transmission Gear Stress (TO Power Rating)**

	Drive-Lead		Drive-Follow		Lead-Bull		Follow-Bull		Units
<b>Diametrical Pitch</b>	8		8		8		8		teeth / in
<b>Gear Ratio</b>	1.75		2		3.43		3		
<b>RPM</b>	3046 / 1743		3046 / 1523		1743 / 509		1523 / 509		RPM
	<b>Drive</b>	<b>Lead</b>	<b>Drive</b>	<b>Follow</b>	<b>Lead</b>	<b>Bull</b>	<b>Follow</b>	<b>Bull</b>	
<b>Contact Stress</b>	176,726	173,171	174,100	170,007	181,499	174,414	169,857	163,794	psi
<b>Allowable Contact Stress</b>	177,645	181,509	177,645	182,445	181,499	190,360	182,422	190,346	psi
<b>Bending Stress</b>	21,910	18,552	21,761	17,692	17,957	36,238	16,937	36,022	psi
<b>Allowable Bending Stress</b>	39,490	40,041	39,490	40,174	40,040	41,284	40,171	41,282	psi

### 6.10.3 Auxiliary Gearbox

There is a  $90^\circ$  direction change required between the engine's main output shaft and the transmission's drive gear; therefore, an auxiliary gearbox was installed which houses a single bevel gear connection. This gearbox has the following characteristics described in the Table 14.

**Table 15: Auxiliary Gearbox Stress (TO Power)**

	Engine Output	Transmission Input	Units
<b>Diametrical Pitch</b>	9		teeth / in
<b>Bevel Gear Ratio</b>	1.97		
<b>RPM</b>	6000	3046	RPM
<b>Pitch Diameter</b>	3.22	6.33	in
<b>Contact Stress</b>	152,410	152,410	psi
<b>Allowable Contact Stress</b>	225,445	234,805	psi
<b>Bending Stress</b>	21,679	25,109	psi
<b>Allowable Bending Stress</b>	38,832	27,641	psi

## 7 Structural Design

### 7.1 Structural Design Criteria

The structural design criteria were principally based on FAR Part 27. The load factor versus velocity diagram for the Rambler's structural limiting load envelope was constructed using FAR Part 27.337, which states that a rotorcraft must be designed for a limit maneuvering load factor ranging from a positive limit of 3.5 to a negative limit of 1.0. These requirements can be reduced to smaller range of positive 2.0 to negative 0.5, but only if higher loading conditions can be shown to be extremely remote. As a training helicopter likely to experience high loads as a result of poor flight techniques, the larger limit maneuvering load factor range was used for the Rambler. In calculating the critical airspeeds for the Rambler, the approach described in the *Engineering Design Handbook* was used.<sup>19</sup> The design maximum level flight speed,  $V_H$ , in forward flight was determined to be 118 knots as a result of performance analysis. The design limit flight speed,  $V_{DL}$ , was then calculated using a factor of 1.15 times  $V_H$ , a typical ratio for observation and training helicopters, which resulted in 136 knots. The never exceed speed,  $V_{NE}$ , was assumed to be equal to  $V_{DL}$  for preliminary design purposes. In developing the V-n diagram depicted in Figure 52, the following flight maneuvers were addressed in accordance with FAR Part 27: symmetric pull-up, 1-g dive ( $n=1.0$ ), level flight, takeoff and climb, hover, and rolling pull-up maneuver. A static analysis was also performed in NASTRAN/PATRAN. In Figure 53, a representative high positive 3 g load case is shown with the distributed transmission and engine loads included.

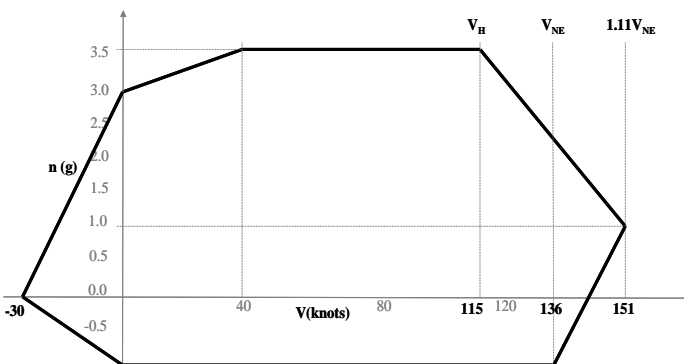


Figure 52: V-n Diagram

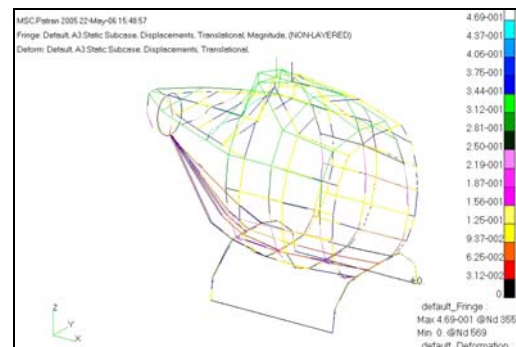


Figure 53: Static Analysis of Fuselage

### 7.2 Fuselage Design

#### 7.2.1 Configuration Selection

In determining the material structure that was best suited for the Rambler, consideration was given to the use of a traditional metal frame and sheet metal skin construction versus the use of a fully-composite fuselage design. Although the standard metal design traditionally offers significant savings in

production cost over composite construction, emerging technologies are quickly bridging this financial gap. Using the Bell Cost Model<sup>31</sup>, a material selection trade study indicated that a composite fuselage would only cost 7.8% more than metal – accounting for an overall increase of less than 1% of the vehicle’s total production cost. Despite this minor disadvantage, composite materials offer critical weight savings over metal construction and they are superior to metals in resistance to corrosion, reducing the overall maintenance requirements and direct operating cost. In a research effort conducted by NASA and the US Army Research Laboratory in 1999, a 1/5 scale composite fuselage – designed for light aircraft and rotorcraft applications – was shown both experimentally and analytically to achieve improved crashworthiness results.<sup>32</sup> The goal of this research program was “to demonstrate a new fuselage concept for improved crashworthiness, which can be fabricated using low-cost materials and manufacturing techniques.”<sup>32</sup> A similar composite design was selected for the Rambler to capitalize on cost and weight savings, improved reliability, and increased safety.

### 7.2.2 Composite Structure

The details of the Rambler’s composite fuselage design were largely based on the findings presented in the previously mentioned NASA Report. The characteristics and materials selected for this design are depicted in Figure 54. The exterior contour and dimensions were driven by human size factors and consideration of the ergonomics required to safely adjust the flight controls. From the crashworthy design perspective, the fuselage’s upper section was designed to be stiff, yet frangible enough to deform during a crash sequence, thus protecting the occupants by dissipating the energy in doing deformation work. Hence, a relatively low stiffness E glass/epoxy skin was chosen for the fuselage with a foam core sandwiched between the inner and outer walls to further absorb the energy. The floor section materials were selected in order to maintain high structural rigidity and minimize deformation upon impact; therefore, a hybrid laminate of graphite/epoxy and E glass/epoxy that exhibits high stiffness and excellent strength properties was used.

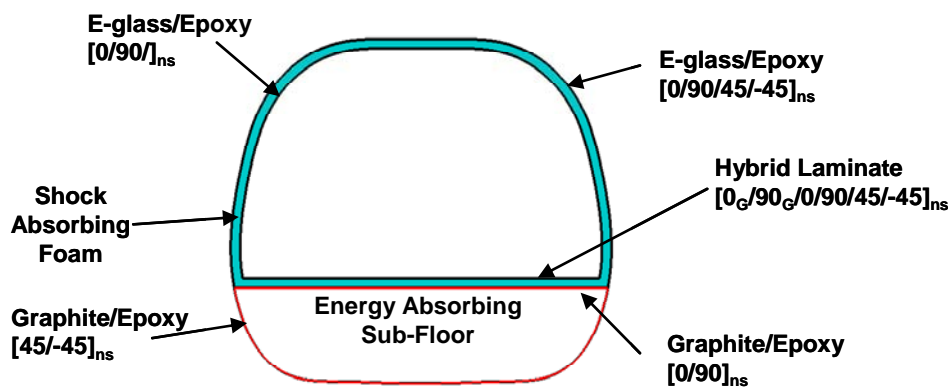


Figure 54: Composite Fuselage Design



The lower half of the fuselage was also designed to deform during a crash sequence and thus an E glass/epoxy was used for this area. Finally, a foam-filled, energy absorbing sub-floor was implemented to provide an additional source of energy dissipation. A structural redundancy in the form of a shear pin between the L section floor beams was provided. During a crash, the shear pin will fail and cause the disconnection of the lower L beam from the upper L beam, thus the energy would not be transferred to the floor where the pilot seats are mounted. Figure 55 shows a detailed view of this safety feature.

In order to effectively compensate for the vertical load paths required for any vertical takeoff and landing (VTOL) application, the Rambler's structural design also incorporates a series of composite stringers and ribs needed to take bending and shear loads. Specifically, this skeletal framework, directly attached and co-cured with the inner walls of the fuselage, incorporates load paths within the fuselage structure. In order to integrate their connection to the skid landing gear, a combination of two keel beams running through the sub-floor along the longitudinal axis of the aircraft was used. Figure 56 shows the primary structural load paths.

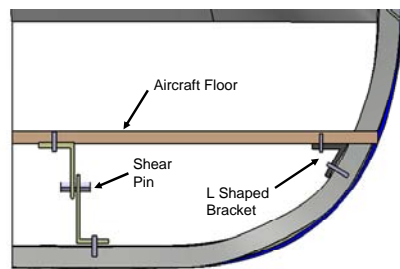


Figure 55: Keel Beam Detail

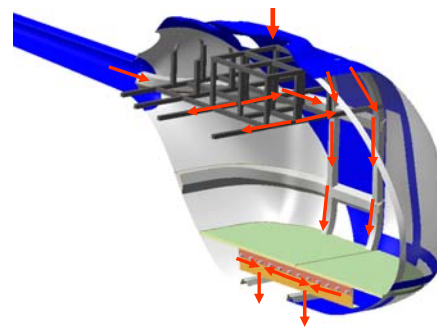


Figure 56: Primary Structural Load Paths

### 7.2.3 Manufacturing

The Rambler's fuselage manufacturing is based on the composite bonding of two halves similar to that used by the Adam Aircraft Corporation.<sup>33</sup> While the Adam Aircraft manufacturing methodology of eliminating all stringers, longerons, spars, and ribs by laying the fiber at the orientation at which the load path occurs is highly desired, such a composite fuselage without metal fittings has not been yet demonstrated for rotorcraft technology. Hence, the Rambler design incorporates a more conservative combination of metal fittings and composite cured and co-cured parts. An example is the Rambler's use of metal L shaped brackets along the inner wall of its composite fuselage over which the composite floor beam will be bolted (Figure 55). Programmable Powder Preform Process (P4), a new and cost-effective mold manufacturing technique, uses robotic choppers to spray short fibers onto glass to create the preform for the structure. This process is followed by the injection of resin and curing in a mold, thus creating the two fuselage outer and inner walls between which the foam will be glued. The upper and lower portions of the fuselage will be manufactured using this technique and then connected to the floor.

## **7.3 Landing Gear**

### **7.3.1 Configuration Selection**

As a training helicopter that will likely experience numerous hard landings, the design of the Rambler's landing gear was considered in detail to ensure the crashworthiness of its configuration. A standard skid landing gear configuration was selected for its overall design simplicity and robustness over more expensive and complicated wheeled systems that employ shock absorbing oleo struts, etc. Although these wheeled landing gears offer improved pilot and passenger comfort, in a training environment, the "unforgiving" characteristics of skid landing gears are beneficial in developing a pilot's control touch. Ultimately, the skid landing gear design is lightweight, less expensive, easy to maintain, and capable of withstanding high static and dynamic loads.

### **7.3.2 Dimensions and Materials**

Based on a paper written by Tho, C. et al,<sup>34</sup> the skid landing gear was designed using hollow circular skid tubes and hollow box-section cross beams. The cross sectional dimensions of the circular section had an outer diameter of 3 inches and an inner diameter of 2 inches; the rectangular cross section had a width of 2 inches and a height of 1.5 inches. A representative thickness of 0.5 inches was selected for both the circular skid tubes and the box-section cross beams. As depicted in Diagram Sheet 1, the length of the skid tubes, width of the cross beams, and height of the landing gear above the ground were finalized based on engineering judgment and fuselage design considerations.

Tungsten carbide was initially considered as the material for the landing gear in accordance with the paper previously mentioned; however, despite its high strength characteristics, it is a very expensive and dense material. Therefore, structural steel was selected as an alternative. With an ultimate tensile strength (UTS) of 94 ksi and yield strength of 45 ksi, structural steel demonstrated the necessary characteristics essential for a crashworthy design as shown in the next section of this report.

### **7.3.3 Crashworthiness Analysis**

In accordance with the FAR Part 27.725 Limit Drop Test for rotorcraft landing gears, a comprehensive analysis was performed in order to verify the crashworthiness of this landing gear design. Additionally, FAR 27.501 stipulates certain testing requirements that are specific to skid landing gear configurations, such as, the standard drop height of 13 inches must be increased by a factor of 1.5 with an initial velocity of 109.77 in/sec. For this proposal, however, even more stringent US Navy standards were used – a drop height of 25 inches and velocity of 122 in/sec – to ensure that federal crashworthiness standards were exceeded. A finite element model was developed using ABAQUS. Initially, the landing

gear configuration was modeled using solid tetrahedral elements and the ground as an analytical rigid surface (Figure 57). With a partitioned mesh, the model consisted of over 90,000 tetrahedral elements requiring 5-6 days of computational run-time. Using the paper by Tho et al,<sup>34</sup> a beam element model was created to expedite the computational process.

The beam element model utilized a three-dimensional wireframe for the skid tubes and the cross beams in which beam section circular pipe and rectangular box section profiles were assigned. The following material properties of isotropic steel were then applied to the model: stiffness of  $30 \times 10^6$  psi, density of  $0.283 \text{ lb/in}^3$ , and a plasticity stress-strain curve with yielding at 45 ksi and 1% plastic strain at 75 ksi. Beam section orientations were assigned, instances of the individual parts were created, and a mesh independent assembly instance was created using B32 beam elements in ABAQUS. The fuselage was represented as a rigid node with assigned mass and inertia properties and rigid beam connectors were used to connect the fuselage node to the cross beams. The ground was meshed using four node shell elements (S4R). Figure 58 shows the entire beam element model for the landing gear.

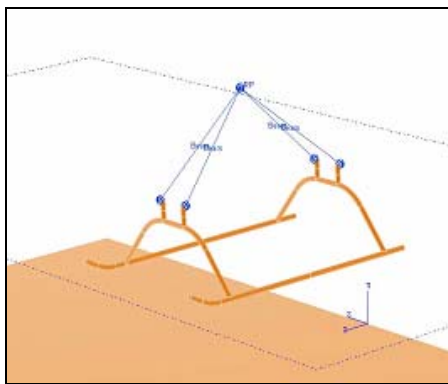


**Figure 57: Solid Model of Skid Landing Gear**

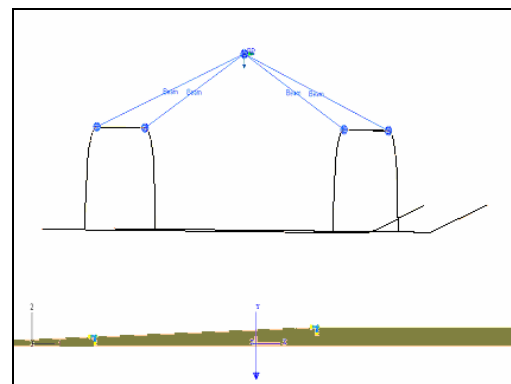


**Figure 58: Beam Element Model of Skid Landing Gear**

Using the beam element landing gear model, the total analysis time was reduced to 2-3 hours. The total time step varied from 155-200 milliseconds depending upon the landing condition being evaluated. In specifying the interaction properties between the landing gear and the ground, the following assumptions were used: a static coefficient of friction of 0.5, a dynamic coefficient of friction of 0.35, a decay coefficient of 0.05, and no ground separation after contact. A surface-to-surface master-slave contact interaction was specified in which the ground was specified as the master surface and the bottom of the skid tubes as the slave node region. In establishing the loads and boundary conditions, the ground was rigidly fixed by activating the Encastre boundary condition, thus constraining all six degrees of freedom, 1-g gravity load was activated over the entire landing gear model, and velocities along the appropriate directions were prescribed according to the landing scenario being simulated. In accordance

with FAR requirements, four landing scenarios were modeled as follows: level landing on two skids, pitch-down nose first landing, pitch-up aft first landing, and single skid rolling landing. Figures 59 and 60 show an example of the program output for the level landing and single skid landing conditions. Table 15 summarizes the results from all four landing modes analyzed using the beam element model.

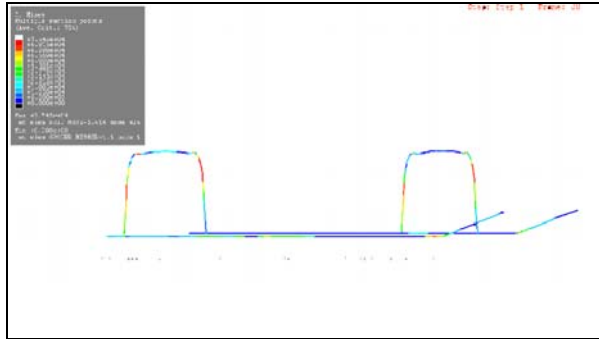


**Figure 59: Level Landing**

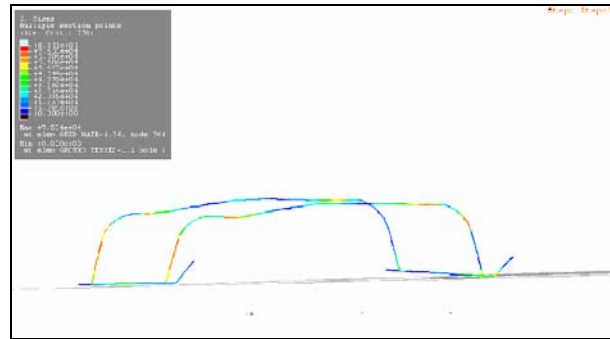


**Figure 60: Landing on One Skid**

**Table 16: Limit Drop Test Results**

<b>Landing Condition</b>	<b>Max Observed Stress [ksi]</b>	<b>Max Allowable Stress for Rupture [ksi]</b>
Level	75	94
Nose First	76	94
Aft First	78	94
Single Skid Rolling	81	94

The landing gear design of the Rambler exceeds the Federal requirements with the single skid rolling landing condition exhibiting the highest observed stress of 81 ksi – 13 ksi below the material rupture limit of isotropic steel. In each scenario, the landing gear experienced yielding without rupture, a key characteristic of crashworthy landing gear design. This margin of error is important for training helicopters where the probability of the aircraft sustaining a hard landing is dramatically increased.

### 7.3.4 Landing Gear Dampers

Based on the ground resonance phenomenon and the available lead-lag damping inherent in the Hanson rotor system, lead-lag dampers may not be required. However, dampers can be provided on the cross beam of the skid, if necessary. The Deutsch criterion would be used to determine the damping required by considering the product of the blade lag damping and the fixed system damping effective at the hub.<sup>35</sup>

## 8 Stability and Control Analysis

### 8.1 Flight Controls Layout

The Rambler’s flight control system is centered on simplicity. Low cost, traditional flight controls are used throughout the design, with the exception of the rotating and non-rotating swashplates which are mounted above the rotor system. The excellent handling qualities and safety features of the “ideal rotor” make this a practical design solution. Figure 61 shows a schematic diagram of the Hanson “spider” swashplate – the control linkages are made possible through the use of an inner non-rotating mast. Figure 62 depicts the Rambler’s flight control connectivity between the pilot controls and the rotating systems of both the main rotor and tail rotor, as modeled in CATIA. By eliminating the need for hydraulic boost and force feel systems, significant weight reduction and flight control simplicity is achieved, as well as, more realistic training benefit.

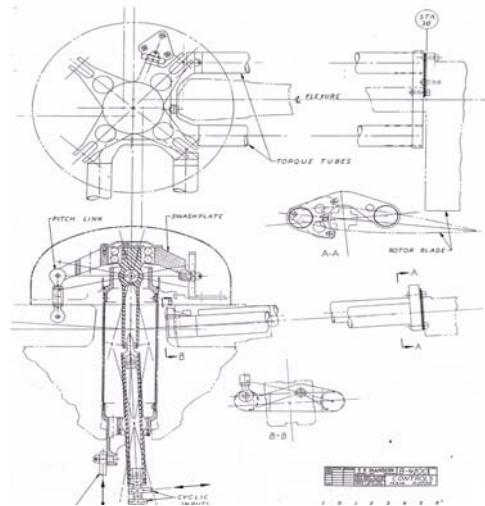


Figure 61: Hanson Swashplate Controls

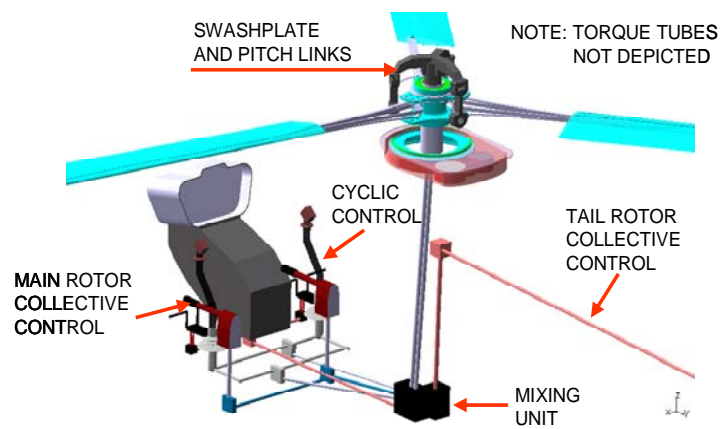
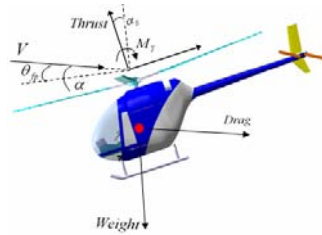


Figure 62: Rambler Flight Controls Connectivity

### 8.2 Flight Characteristics

#### 8.2.1 Helicopter Trim Solutions

A team developed computer program in MATLAB was used for trim analysis. Initial aircraft geometric variables from GTPDP were input to trim for flight speeds ranging from hover to 140 knots. Simplified propulsive trim equations from *Helicopter Stability and Control Course* at Georgia Tech were used for the algorithm.<sup>36</sup> Figures 63 and 64 show force and moment static free body diagrams (FBD’s). Figures 65-69 compare the results of this trim analysis for each control setting and pitch attitude for the Rambler and R-22.



**Figure 63: Longitudinal Forces and Moments**

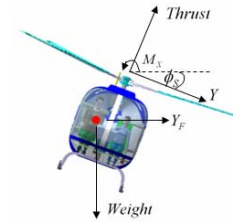
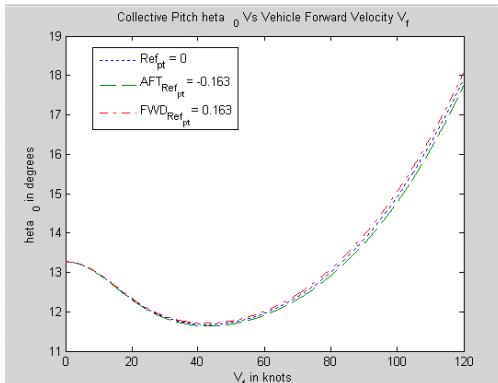
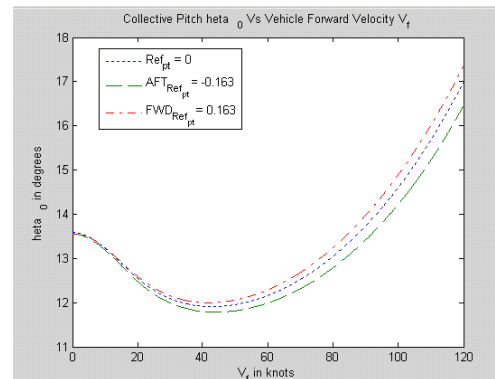


**Figure 64: Lateral Forces and Moments**

Main rotor collective decreases as velocity increases due to a decrease in induced drag. In high speed forward flight, collective will need to increase to compensate for parasite drag (the dominant drag force at high velocity). CG position requires an increase in collective as it moves aft. From the collective pitch plot, the Rambler demonstrates better control power than the R-22.<sup>37</sup>



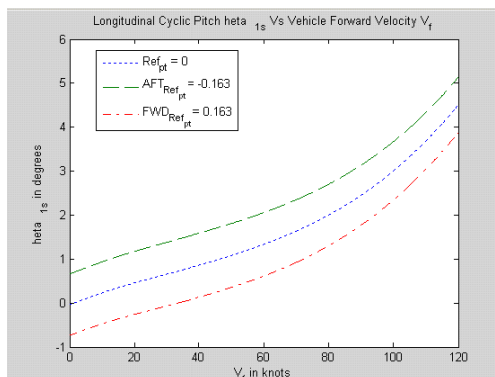
(a) Rambler



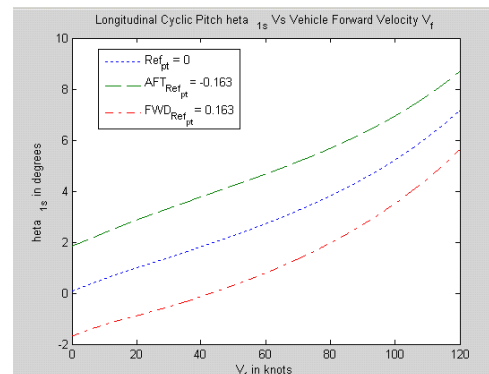
(b) Robinson R-22

**Figure 65: Collective Pitch ( $\theta_0$ ) Control Position Plots**

Longitudinal cyclic needs to increase in order to produce the required thrust in forward flight and it will also increase as CG moves aft to compensate for increasing pitch up movement. The Rambler clearly indicates a more sensitive control justifying that less input would yield better pitching motion.



(a) Rambler



(b) Robinson R-22

**Figure 66: Longitudinal Pitch ( $\theta_{1s}$ ) Control Position Plots**

A decrease in lateral cyclic or roll left to compensate for tail rotor and vertical tail side force is evident as velocity increases. As CG position moves aft, the angle will increase due to coupling effect of the hinge offset. The Rambler has 10% hinge offset and therefore shows better balancing of roll stability.

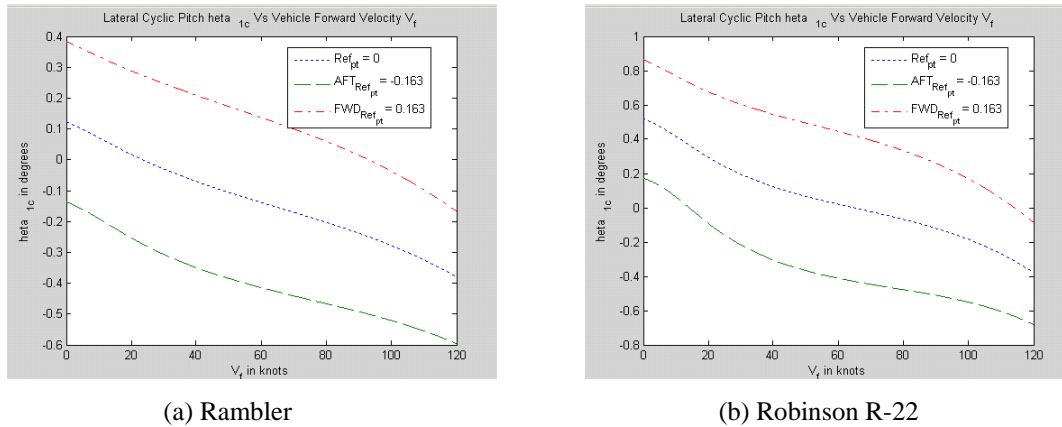


**Figure 67: Lateral Pitch ( $\theta_{1c}$ ) Control Position Plots**

The tail rotor collective will decrease as velocity increases due to an increase in the vertical stabilizer side force with velocity. The Rambler shows more efficient control sensitivity than R-22.

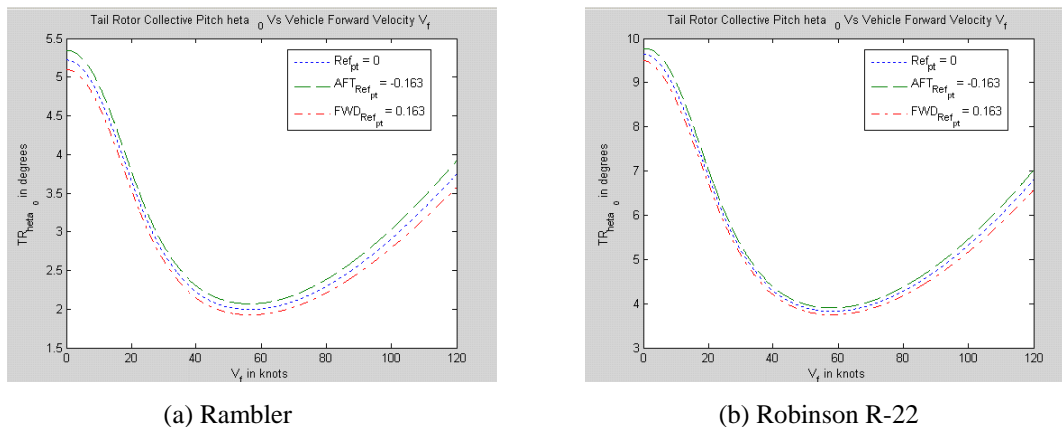


**Figure 68: Tail Rotor Collective ( $\theta_{tr0}$ ) Control Position Plots**

The pitch angle decreases or pitches down as the vehicle's speed increases. A forward CG will result in a smaller pitch angle relative to the pitch angle of the CG aligned with the hub. As the CG moves aft, the pitch angle will increase. The Rambler shows faster pitch attitude control in terms of control inputs at varying speeds which is indicative of better flying qualities and control maneuverability.

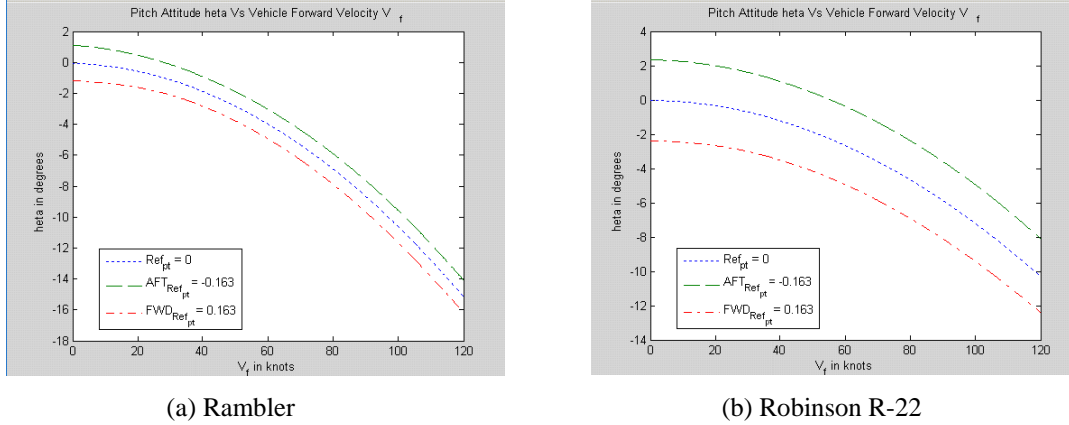


**Figure 69: Body Pitch Attitude ( $\theta$ ) Plots**

It is evident that the Rambler demonstrates better flight characteristics than the R-22 from initial assumptions by requiring smaller control inputs to achieve a trimmed solution across the entire flight speed and CG ranges.

## 8.2.2 Linear Control Root Locus Plots

The vehicle's dynamic responses to external perturbations were examined. External gust and control deflection responses were used to evaluate the comparative handling qualities of Rambler. Due to the complex nature of helicopters involving coupling effects between longitudinal and lateral responses, a linear model was used with stability derivatives at each trim point as shown in Equation 9:

$$\dot{X} = AX + Bu \quad \text{Equation 9}$$

where  $X$  is the state vector,  $u$  is the control input,  $A$  is the stability matrix, and  $B$  is the control matrix. A MATLAB code was developed to calculate the eigenvalues and eigenvectors of the response modes based on stability derivatives estimated from similar helicopters and the Rambler model in FlightLab. Various stability derivatives (forces and moments) were used for the purpose of this analysis – some important ones are listed below:

$X_u, X_w, X_q, X_{\delta_c, \delta_e}, Y_v, Y_{\delta_a}, Z_u, Z_w, M_u, M_w, M_q, M_{\delta_c, \delta_e}, L_v, L_p, L_{\delta_a}, N_v, N_r, N_{\delta_p}$ , etc. The MATLAB/C/C++ code uses the following individual matrices for decoupled and coupled cases with certain assumptions for ease in obtaining trim solutions and root locus plots:

Longitudinal (decoupled matrices):

$$A_{Long} = \begin{bmatrix} X_u/m & X_w/m & 0 & -g \cos \theta_0 \\ Z_u/m & Z_w/m & V_0 + Z_q/m & -g \sin \theta_0 \\ 0 & 0 & 1 & 0 \\ M_u'/I_y & M_w'/I_y & M_q'/I_y & -g M_w \sin \theta_0 / I_y \end{bmatrix} \quad B_{Long} = \begin{bmatrix} X_{\delta_c}/m & X_{\delta_e}/m \\ Z_{\delta_c}/m & Z_{\delta_e}/m \\ M_{\delta_c}'/I_y & M_{\delta_e}'/I_y \\ 0 & 0 \end{bmatrix}$$

where,  $M_u' = M_u + M_w Z_u/m$ ,  $M_w' = M_w + M_w Z_w/m$

and  $M_q' = M_q + M_w(V_0 + (Z_q/m))$

where,  $M_{\delta_c}' = M_{\delta_c} + M_w Z_{\delta_c}/m$

and  $M_{\delta_e}' = M_{\delta_e} + M_w Z_{\delta_e}/m$



Lateral (decoupled matrices):

$$A_{Lat} = \begin{bmatrix} Y_v/m & Y_p/m & Y_r/m - V_0 & g \cos \theta_0 \\ L_v/I_x' + I_{zx}'N_v & L_p/I_x' + I_{zx}'N_p & L_r/I_x' + I_{zx}'N_r & 0 \\ N_v/I_z' + I_{zx}'L_v & N_p/I_z' + I_{zx}'L_p & N_r/I_z' + I_{zx}'L_r & 0 \\ 0 & 1 & \tan \theta_0 & 0 \end{bmatrix} \quad B_{Lat} = \begin{bmatrix} Y_{\delta_a}/m & Y_{\delta_p}/m \\ L_{\delta_a}/I_x' + I_{zx}'N_{\delta_a} & L_{\delta_p}/I_x' + I_{zx}'N_{\delta_p} \\ N_{\delta_a}/I_z' + I_{zx}'L_{\delta_a} & N_{\delta_p}/I_z' + I_{zx}'L_{\delta_p} \\ 0 & 0 \end{bmatrix}$$

Coupled Dynamic Matrices:--

$A_{Coupled} =$

LONGITUDINAL				COUPLING			
$X_u/m$	0	$-u_0$	$-g \cos \theta_0$	0	0	0	$v_0$
$Z_u/m$	$Z_w/m$	$u_0$	$-g \cos \phi_0 \sin \theta_0$	0	$v_0$	$-g \sin \phi_0 \cos \theta_0$	0
$M_u/I_y$	$M_w/I_y$	$M_q/I_y$	0	$M_v/I_y$	$M_p/I_y$	0	$M_r/I_y$
0	0	$\cos \phi_0$	0	0	0	0	$-\sin \phi_0$
0	0	0	$-g \sin \phi_0 \sin \theta_0$	$Y_v/m$	$w_0$	$g \cos \phi_0 \cos \theta_0$	$-u_0$
0	0	$\frac{I_x L_u + I_{zx} N_u}{I_c}$	0	$\frac{I_x L_v + I_{zx} N_v}{I_c}$	$\frac{I_y L_p + I_{zx} N_p}{I_c}$	0	$\frac{I_x L_r + I_{zx} N_r}{I_c}$
0	0	$\sin \phi_0 \tan \theta_0$	0	0	1	0	$\cos \phi_0 \tan \theta_0$
0	0	$\frac{I_{xz} L_u + I_{zx} N_u}{I_c}$	0	$\frac{I_{xz} L_v + I_{zx} N_v}{I_c}$	$\frac{I_{xz} L_p + I_{zx} N_p}{I_c}$	0	$\frac{I_{xz} L_r + I_{zx} N_r}{I_c}$
COUPLING				LATERAL			

LONGITUDINAL		COUPLING	
$X_{\delta_a}/m$	0	0	0
$Z_{\delta_a}/m$	$Z_{\delta_z}/m$	0	$Z_{\delta_p}/m$
$M_{\delta_a}/I_y$	$M_{\delta_z}/I_y$	$M_{\delta_v}/I_y$	$M_{\delta_p}/I_y$
0	0	0	0
0	0	$Y_{\delta_a}/m$	$Y_{\delta_p}/m$
0	0	$\frac{I_x L_{\delta_a} + I_{zx} N_{\delta_a}}{I_c}$	$\frac{I_x L_{\delta_p} + I_{zx} N_{\delta_p}}{I_c}$
0	0	0	0
0	0	$\frac{I_{xz} L_{\delta_a} + I_{zx} N_{\delta_a}}{I_c}$	$\frac{I_{xz} L_{\delta_p} + I_{zx} N_{\delta_p}}{I_c}$
COUPLING		LATERAL	

All the different modes based on eigenvalues, half/double time, and period are outlined in Figures 70-72.

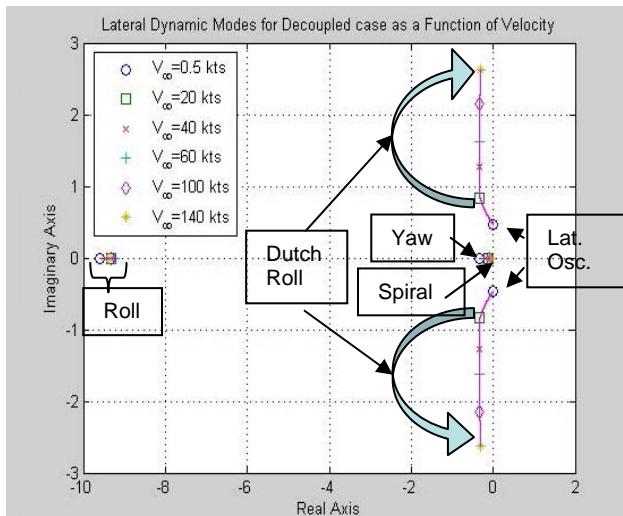


Figure 70: Lateral Modes (Decoupled)

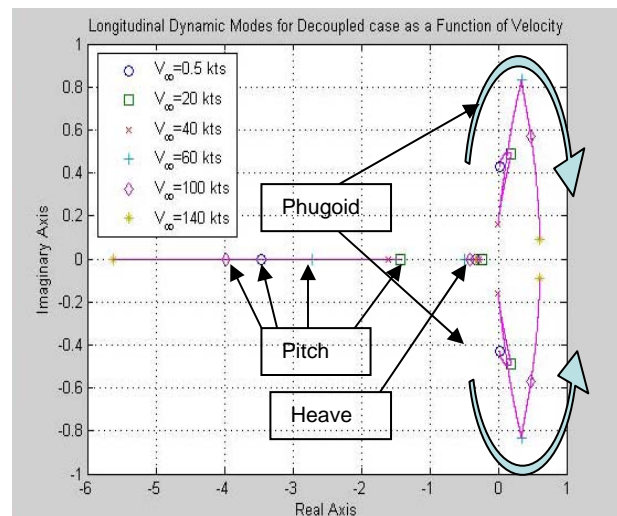


Figure 71: Longitudinal Modes (Decoupled)

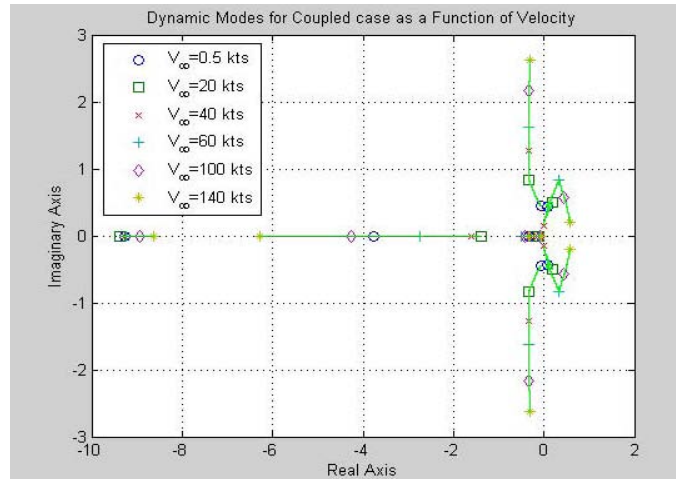


Figure 72: Dynamic Modes (Coupled)

### 8.2.3 FlightLab<sup>13</sup> Modeling

Using FlightLab, an industry-standard program, further trim analysis was done and linear models around trimmed flight conditions for the Rambler and Robinson R-22 were established. Both models were customized using the model editor feature. The Rambler was configured with a representative Hanson hub by utilizing a 3-bladed, fully-articulated rotor with 10% hinge offset, and later with a conventional hingeless rotor hub, rigid fuselage, Bailey tail rotor model, horizontal and vertical stabilizers, and an ideal engine. The R-22 model captured the dynamics of a teetering rotor hub with the difference of a 2-bladed NACA airfoil in contrast to VR-7 used in our design. Using the speed sweep function, the aircraft models were trimmed at speeds from hover to 140 knots. Figure 73 and 74 show the results of the parameter sweeps. Some spikes in the R-22 plots resulted from the trim solution not converging while Rambler trimmed for even higher speeds and supported Hanson’s “ideal rotor” claims.

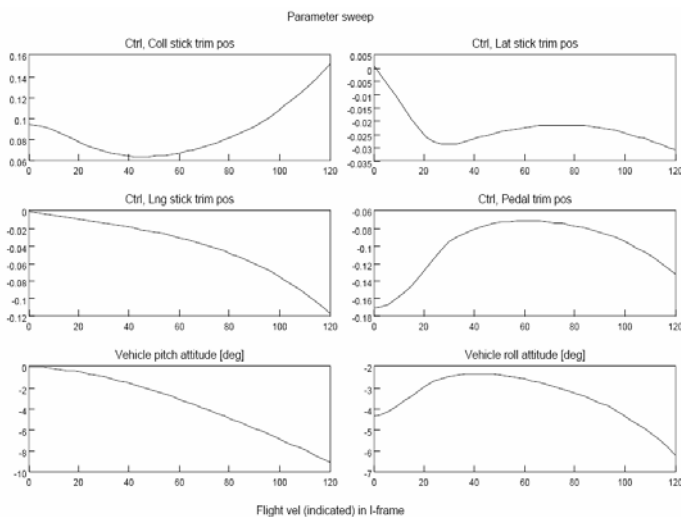


Figure 73: Rambler Parameter Sweep Results

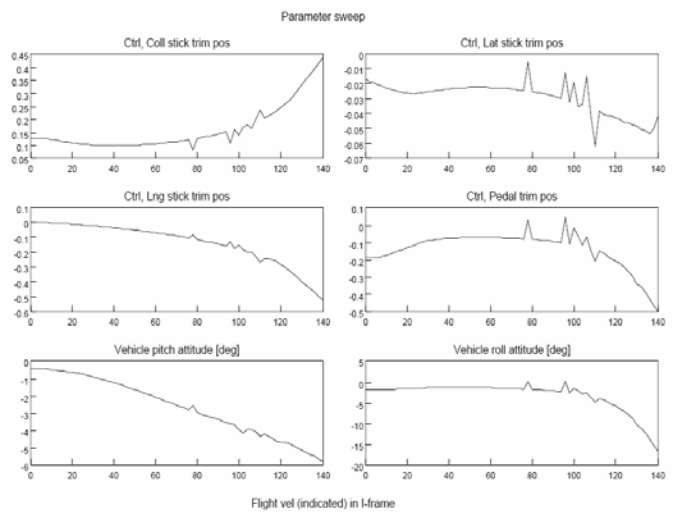
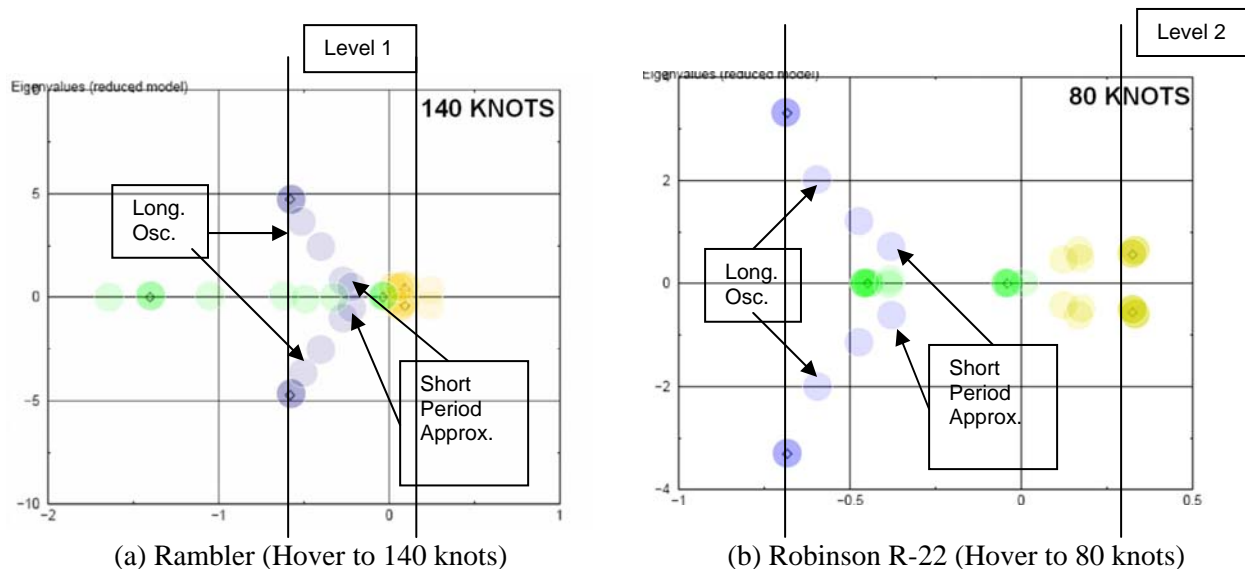


Figure 74: Robinson R-22 Parameter Sweep Results

A linear version of the nonlinear model was generated around each trim point after the parameter sweep was accomplished to study root locus plots and validate the MATLAB code results shown previously. Dynamic characteristics of the trim point could be analyzed with classical stability and control theory. Using a reduced-order linear model, the local behavior of the vehicle at a given flight condition was also observed. Figure 75 depicts the root locus plots generated using this reduced-order linearization model for the Rambler (hover to 140 knots) and R-22 (hover to 80 knots), respectively. From the theory of hingeless rotors (offset-hinge articulated rotor) and Hanson's hub design handbook, the major factor introduced by an increase in flap frequency greater than 1/rev is the hub moment produced by tip-path-plane tilt, which greatly increases the capability of the rotor to produce moments about the helicopter CG. This was validated by studying the sensitivity of the controls for CG travel with varying forward speeds. The individual plots and coupled dynamics also show increased coupling of the lateral and longitudinal motions. Figure 75 demonstrates that as the R-22 approaches higher speeds of 80 knots, it starts to exhibit instability and at greater speeds it was observed to move into Level 2 handling qualities. The Rambler, however, with 10% hinge-offset exhibited damped longitudinal oscillations at higher speeds and good short-period approximations at low-speeds staying well within Level 1 handling qualities.<sup>35</sup>



**Figure 75: Linearized Eigenvalues for Reduced Aircraft Models**

Flap hinge offset of an articulated rotor does not radically alter the character of the helicopter flight dynamics, although there is an important quantitative improvement of the handling qualities due to hub moment capability. For a hingeless rotor, the flap frequency is large enough to have a major impact on the dynamics. The force derivatives vary little with flap frequency, but it is the pitch moments that

dominate the longitudinal dynamics. The moment derivatives are roughly doubled by using flap hinge offset. For a typical hingeless rotor, the control derivative  $M_{\theta}$  and speed stability  $M_u$  are increased by a factor of 3-4 compared to articulated rotor case (no flap hinge-offset). The pitch damping  $M_q$  is increased even more, because of the force component that reduces the damping produced by thrust vector tilt. Thus, Hanson’s “ideal rotor” will certainly have larger pitch damping and a less unstable oscillatory mode than the articulated or teetering rotor. With larger control power, as well, the task of controlling the helicopter becomes easier as shown by the sensitivity of our control input plots. Although some might interpret the Rambler’s increased control sensitivity as a training detriment, a responsive vehicle with standard control rigging can help a pilot develop better flight control techniques by minimizing unnecessary inputs.

### 8.3 Handling Qualities

One of the key characteristics of the “ideal rotor” design is the improved handling qualities in hover and low speed flight that it exhibits as a result of high control power and damping about the pitch and roll axes. In Figure 76 and 77, a control power versus damping comparison is shown between the Rambler and the R-22 in the pitch, roll, and yaw axes during hovering flight. The desired areas were used in the Army AHIP Program specification to provide industry with a standard for measuring the low speed agility capability for scout helicopters. In pitch and roll, the Rambler outperforms the R-22 by demonstrating a greater tendency to stay within the desired control bounds. In the yaw axis at reduced airspeeds, the Rambler shows desirable control sensitivity, but slightly less than desirable directional damping. Therefore, a simple Stability and Control Augmentation System (SCAS) will be incorporated into the Rambler’s flight control design to provide the necessary rate damping required for improved flight stability in the yaw axis.

Symbol Convention: ☆ - Rambler  
○ - Robinson R-22

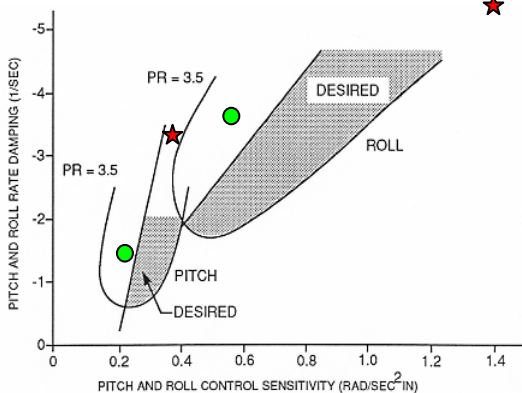


**Figure 76: Pitch and Roll Damping versus Pitch and Roll Control Sensitivity at Hover**

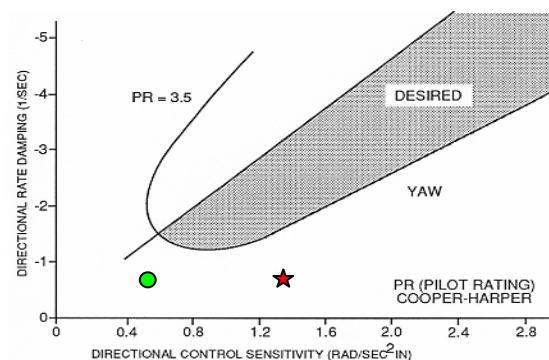


**Figure 77: Yaw Damping versus Yaw Control Sensitivity at Hover**

Tactical military flight and day-visual civil flight tend toward a desire for angular rate response, rather than the acceleration response common to teetering rotors without hub springs or hinge offset. As the visual cue environment degrades and flight path precision requirements increase as with civil instrument flight rules (IFR), the need for tighter attitude control emerges. Figure 78 and 79 show the handling qualities from hover to 140 knots, demonstrating that the Rambler has desirable pitch damping, but needs improvement in the coupled roll and yaw axes – justifying the use of an affordable off-the-shelf SCAS.<sup>38</sup>

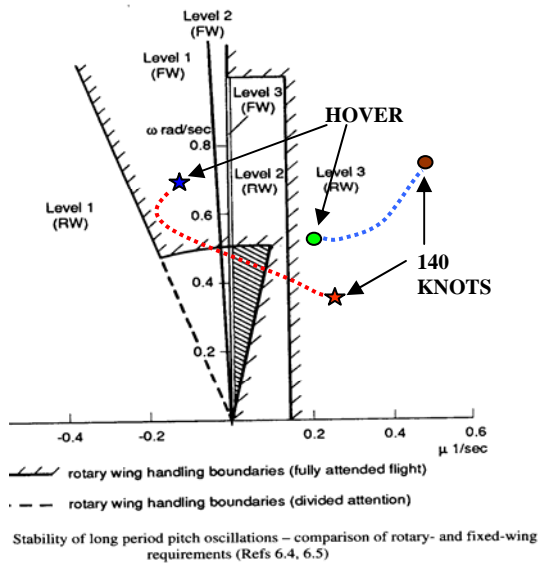


**Figure 78: Longitudinal Long Term Oscillation**

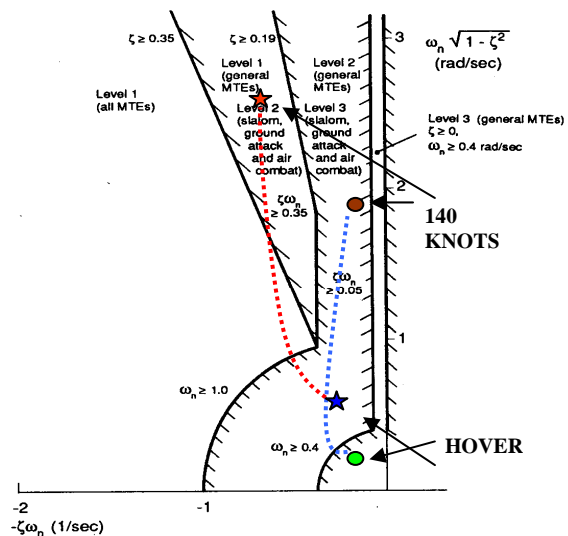


**Figure 79: Lateral Long Term Oscillation**

Codified for the military in ADS-33, and recommended by the bulk of vertical flight aircraft handling qualities studies, this leads to a need for attitude stabilization as well as attitude control for precise hovering and low speed flight in poor visibility conditions. Attitude command in pitch, roll, and yaw (heading) are recommended for poor visibility hover control. As speed increases, the need for more roll maneuverability emerges, leading to a relaxation of roll control to a rate response type. Similarly the desired control in yaw axis changes from heading command to yaw rate control with turn coordination. Figure 80 shows that the Rambler has good stability in the pitch axis, better than the R-22 in the same weight class.

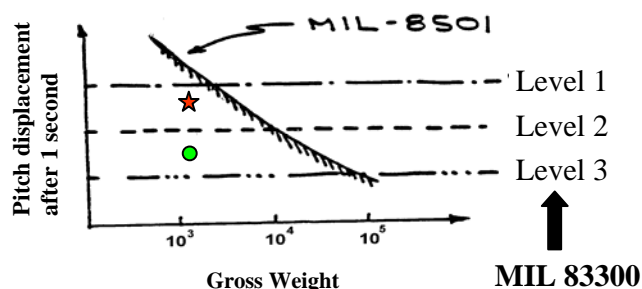


**Figure 80: Pitch Control Analysis Corresponding to MIL-8501 and MIL 83300**

## 8.4 Federal Aviation Regulations (FAR) Requirements

Table 17: Stability and Control FAR Requirements

27.151		<b>Flight Controls</b>
	a	Longitudinal, lateral, directional, and collective controls may not exhibit excessive breakout force, friction or preload.
	b	Control system forces and free play may not inhibit a smooth, direct rotorcraft response to control system input.
27.161		<b>Trim Control</b>
	a,b	Must trim any steady longitudinal, lateral, and collective control forces to zero in level flight at any appropriate speed; and may not introduce any undesired discontinuities in control force gradient.
27.171		<b>Stability</b>
	a	The rotorcraft must be able to be flown, without undue pilot fatigue or strain, in any normal maneuver for a period of time as long as that expected in normal operation.
27.175		<b>Static Longitudinal Stability</b>
		Climb, critical weight, critical center of gravity, maximum power, trimmed at $V_y$ , autorotation and other important constraints in synch with takeoff and landings.

## 8.5 Georgia Tech Unified Simulation Tool (GUST)

GUST, used at Georgia Tech for UAV research and development, under the supervision of Dr. Eric N. Johnson, has been designed to take input parameters from rotor dynamics, aerodynamics, gear dynamics, and flight controls with sensors – enabling it to monitor flight characteristics and perform missions using trajectories in real-life scenarios. The code was largely written in C/C++ using OpenGL as a graphics interface. The wide range of flight dynamics coupled with a variety of desired control response characteristics can be studied with adaptive flight control laws. Two common types of control augmentation for aircraft are *Rate Command Attitude Hold (RCAH)* and *Attitude Command Attitude Hold (ACAH)*. The Robinson R-22 was modeled and tested using this simulator under a DARPA funded initiative and was used as a baseline for comparison with the Rambler. By replicating the Rambler’s CATIA model in an OpenGL model, a comparison between the two could be performed in a non-linear, sensor-integrated environment. Using pilot rotary-wing flight experience, each aircraft model could be flown through a series of training flight scenarios providing real-time analytical feedback.<sup>39, 40</sup>

The *NTSB Special Investigation Report – 96/03*, previously discussed in Section 2.2, recommended the use of simulation to aid in aircraft certification and training. The GUST model provides such a capability and could be an instrumental tool in the pilot developmental process – especially for small helicopter training companies that cannot develop a simulator on their own. New

pilots could be trained on the aircraft’s handling qualities for each maneuver in a simulated environment – increasing their familiarity and proficiency during “real world” flight applications. The use of flight simulation provides an efficient means of maximizing the safety and effectiveness of every training flight.

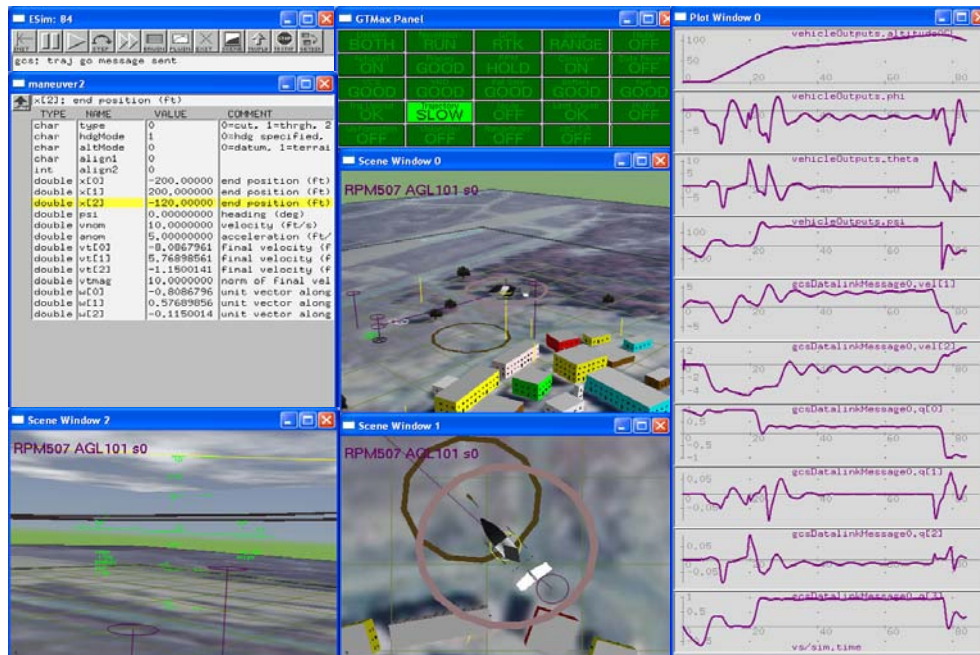


Figure 81: GUST Model Simulator Panel

## 9 Cockpit Layout

### 9.1 Human Size and Visibility Considerations

5<sup>th</sup> percentile Asian female and 95<sup>th</sup> percentile American male were used for ergonomic design limits. The cockpit was designed to ensure safe pilot operation of controls and console equipment from each seat as per FAR Part 27. Visibility from both stations must be unobstructed and undistorted. The CATIA model was used to verify these requirements (Figures 82-84).



Figure 82: Left Seat Reach



Figure 83: Right Seat Reach

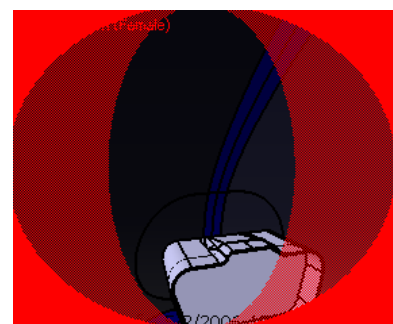


Figure 84: Visibility Plot

## 9.2 Air Crew Seat Design

Each seat was positioned on a fore-aft adjustable track. Height can be adjusted using a lever at the front right of the seat bucket. For safety restraint, each seat was equipped with a combination lap belt and double-shoulder harness with a common buckle assembly. For seat sizing and its cockpit position, 50<sup>th</sup> percentile of the female population was selected as the neutral position. Seat adjustments range from the 5<sup>th</sup> female to 95<sup>th</sup> male percentile. Seats consist of a 14”x18” rectangle with an 18”x31” backrest inclined at 10° to the vertical. Seats adjust 5” vertically and 4.5” fore and aft in increments of ½”.

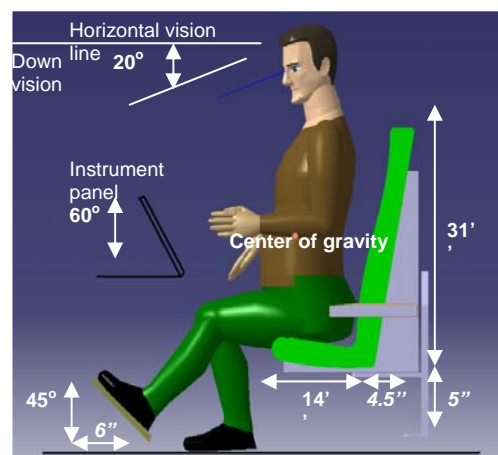


Figure 85: Cockpit Seat Configuration

## 9.3 Console Configuration

An off-the-shelf Electronic Flight Information System (EFIS) was selected for the Rambler as a low-cost, lightweight, and self-contained cockpit display system. It was recently selected for the FH1100 helicopter, an updated version of the Hiller 1100 model. Its capabilities include an attitude and direction indicator (ADI), electronic horizontal situation indicator (EHSI), moving map navigation, and engine monitor capabilities.<sup>41</sup> Figures 86 and 87 show the Rambler’s two console configurations – a single screen EFIS for VFR-only training and a dual-screen for advanced IFR training.

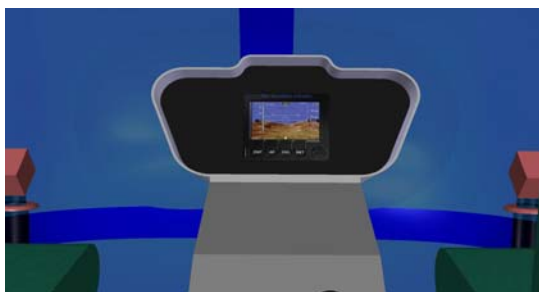


Figure 86: Single Screen EFIS (VFR Only)



Figure 87: Dual Screen EFIS (IFR)



## 10 Manufacturing and Cost Analysis

### 10.1 Product Lifecycle Management (PLM)

As mentioned in the introduction, the success of this design effort relies on the effective synthesis of product and process development. A Product Lifecycle Management (PLM) approach was used to achieve this goal. PLM utilizes software technology to create a virtual setting in which the time, resources, and capital typically needed to develop a new product can be greatly reduced. The DELMIA solution portfolio, a suite of state-of-the-art computer aided manufacturing (CAM) software, provided the digital environment necessary to balance the product, process, and resource requirements of this design. Figure 88 shows a diagram depicting the capabilities of this software package in which a combination of three tools – Process Engineer (in green), V5 Process Simulation (in blue), and Quest (in red) – integrate with CATIA to allow simultaneous product and process development.

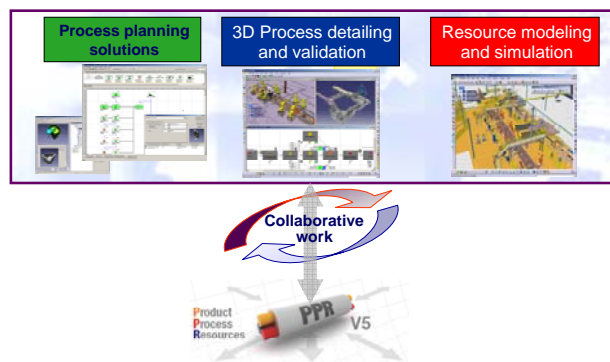


**Figure 88: DELMIA Software Portfolio**<sup>42</sup>

Process Engineer is used by a manufacturing engineer to plan the processes and resources needed to build the design in accordance with the overall production rate and cost requirements. This plan, based only on theory and static analysis, is exported to the V5 Process Simulation tool for validation in a dynamic environment. The design engineer can optimize the product assembly process by conducting trade studies using a virtual workbench to identify component integration problems in terms of contact, collision, or clearance between parts. The resource requirements, identified in the Process Engineer plan, are exported to Quest for 3D factory analysis. This provides the capability of factory layout optimization aimed at maintaining production line balance. Critical product assembly steps that cause bottle-necks in the manufacturing flow can be identified and avoided. This factory analysis is used to update the original Process Engineer plan – thus creating an integrated product and process design loop.

The benefits of incorporating this optimized design approach are many. An independent study in 2003 indicated that, on average, it reduces the time to market for a given product by 30% and the number

of design changes by 65%.<sup>43</sup> This can be attributed to the early detection of assembly problems through simulation and the reduced need for physical prototypes. Additionally, time and financial savings are realized in the reduction of tool design cost, optimized factory layout, and better utilization of labor. Communication and collaboration, both internally and externally, are improved as product and process engineers can immediately visualize the effects of their design decisions across multiple disciplines and suppliers can better understand product requirements. Digital manufacturing also allows “proven” processes to be categorized and re-used in future applications, reducing process planning time.

### 10.1.1 Virtual Engine Gearbox Assembly

For a limited trade study, the integrated DELMIA software capabilities were applied to the Rambler’s engine gearbox design to examine its assembly process. Figure 89 depicts the virtual assembly function which allowed the team to identify potential manufacturing problem areas before any “real” prototype would ever be created. Specifically for the engine gearbox, the CAM software helped to identify the need for bearing configuration changes and a new two-piece casting format for the gearbox housing.

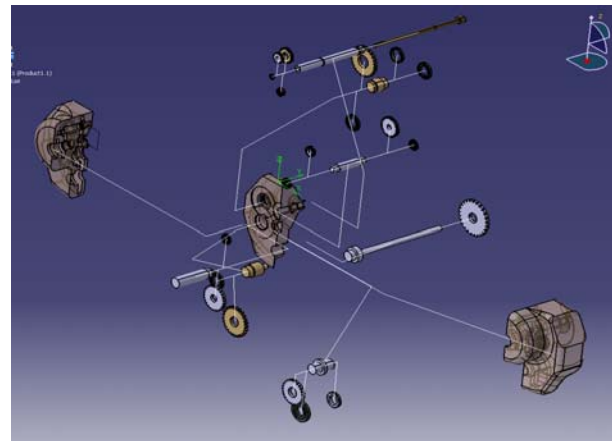


**Figure 89: Engine Gearbox Assembly Process**

## 10.2 Cost Analysis

### 10.2.1 Engine Cost Model

The Price H Cost Estimation software package was used to develop an engine cost model that provided component level manufacturing flexibility. The Price H engine model was generated using engine component weights, volumes, machining tolerances, and material properties to calculate their relative manufacturing complexities. An estimated timeline was created using the assumptions of 3 prototypes, traditional manufacturing methods, and a production rate of 300 units per year for 10 years, as follows:

- |                                       |          |
|---------------------------------------|----------|
| ▪ Project Start Date                  | JAN 2006 |
| ▪ Production Start Date               | JUN 2010 |
| ▪ Production First Available Delivery | JAN 2011 |
| ▪ Production End Date                 | JAN 2021 |

Based on this information, the total average cost per engine in \$60,200 (\$2006).

A trade study was conducted to determine the benefits of increasing the engine’s marketability and decreasing its production timeline. Using the modular engine gearbox design previously mentioned in Section 6.4.5, the engine will be capable of fixed-wing, turboprop applications in addition to its turboshaft configuration. This increased demand for production was conservatively estimated at 300% -- generating a new production rate of 900 units per year. By incorporating the PLM approach through the use of an integrated CAD-CAM environment, the number of required prototypes is reduced to 2 and the time to market is reduced by 30% -- resulting in a first available delivery date of JUN 2009. Based on these assumptions, the total average cost per engine is \$42,530 – a 29% reduction over tradition manufacturing methods.

### 10.2.2 Recurring Cost

The Bell Cost Model was used to examine the Rambler’s estimated recurring cost. This model predicts the cost of each aircraft subsystem by dividing it into three separate cost categories: sub-contract, labor, and materials. It uses the vehicle empty weight to predict the total cost breakdown. A change in empty weight resulted in a change in the cost of each system – with each system cost varying at a different rate. To identify the real cost drivers, a weight-cost factor was calculated using Equation 10:

$$\text{Weight-Cost Factor} = \Delta \text{Weight}_{\text{System}} \cdot \Delta \text{Cost}_{\text{System}} \quad \text{Equation 10}$$

By varying the empty weight by 10% and deriving the Weight-Cost Factors for each subsystem, the following five areas were identified as the most influential: powerplant, fuselage, flight controls, drive system, and rotor. Figure 90 shows these subsystems with their sub-contract, labor, and material categories allocated by percentage. This diagram demonstrates the strong influence of material selection for the fuselage, flight controls, drive system, and rotor – accounting for over 50% of the total vehicle production cost – it underscores the importance of the material design decisions discussed previously in this proposal.

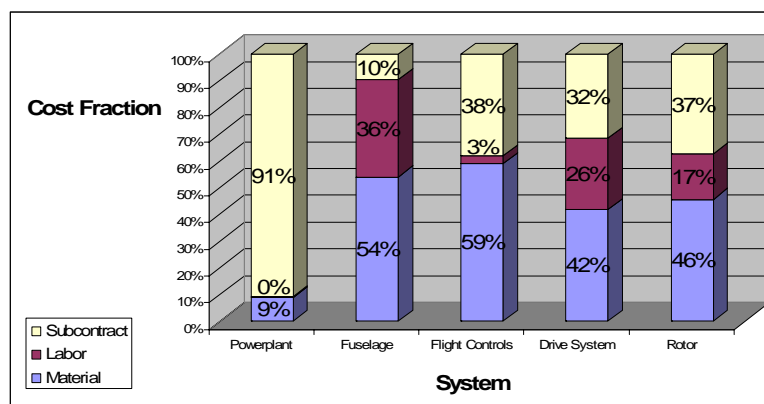


Figure 90: Cost Structure of Cost Driving Systems

Using the Bell Cost Model, a recurring cost breakdown was generated for the Rambler in its final design configuration using US Department of Labor inflation calculator to adjust the values to 2006 dollars.<sup>44</sup> The Price H engine model was also incorporated into the recurring cost breakdown to reflect the modular gearbox design. Appendix B shows the complete recurring cost breakdown, resulting in an average total cost for the Rambler of \$200,576. The current suggested price of a Robinson R-22 Beta II with similar options of the Rambler is \$215,450. It must be noted that this price reflects both recurring and non-recurring cost, as well as, a profit margin. Although the Rambler’s acquisition price will be greater than that of the R-22 once a profit margin is established, it still reflects an extremely competitive result given the high demand for turbine engine flight experience. The owner of Air Atlanta Helicopters stated that a price of \$300,000 would be the competitive threshold for a two-place turbine training helicopter in today’s market.

### 10.2.3 Direct Operating Cost (DOC)

Using the Bell Operating and Support Cost Model, the Rambler’s direct operating cost was estimated. The price of fuel was estimated at \$3 per gallon and the hourly maintenance labor rate at \$55. In order to determine the airframe and powerplant maintenance requirements, four different aircraft DOC tables were used – Robinson R-22, Schweizer 300, Schweizer 333, and Bell 206. The selection of two low cost piston training helicopters and two turbine helicopters helped balance the estimations required for the Rambler. Table 17 shows the DOC breakdown for the Rambler where MH is maintenance hour and FH is flight hour.

	<u><b>COST / FH</b></u>
<b><u>FUEL AND LUBRICANTS</u></b>	
Fuel (8.6 gal/FH @ \$3 per gallon)	25.89
Lubricants (3% of fuel cost)	0.78
	<u><b>26.67</b></u>
<b><u>AIRFRAME MAINTENANCE</u></b>	
Labor (@ \$55 per hour):	
- Scheduled (0.29 MH/FH)	15.95
- Unscheduled (0.12 MH/FH)	6.60
- Overhaul (0.02 MH/FH)	1.10
Parts:	
- Life-limited	1.78
- Unscheduled	3.00
- Overhaul	9.00
	<u><b>37.43</b></u>
<b><u>POWERPLANT MAINTENANCE</u></b>	
Overhaul	26.63
Labor	2.75
	<u><b>29.38</b></u>
<b>TOTAL DIRECT OPERATING COST</b>	<u><u><b>93.48</b></u></u>

This estimate shows that Rambler is competitive with piston training helicopters while offering the performance advantages inherent with turbine engines. Based on the previous assumptions for fuel and maintenance prices, Table 18 shows the relative DOC for each helicopter used in this analysis. Although the Rambler is 22% higher than the R-22, it is a direct result of the increased cost associated

with turbine engine maintenance. However, the Rambler does offer exceptional DOC reduction when compared to the other turbine aircraft, largely due to the higher fuel consumption and maintenance cost associated with the Rolls-Royce Model 250 turbine engine.

**Table 19: DOC Comparison (\$2006)**

	<b>DOC / FH</b>
Robinson R-22 (Beta II)	76.48
Rambler	93.48
Schweizer 300	100.88
Schweizer 333	172.62
Bell 206-B3	281.74

### 10.2.4 Indirect Operating Cost

Insurance is another key cost consideration that falls into the indirect operating expense category. The Rambler’s superior safety features and improved handling qualities will result in fewer accidents over time, thus reducing the insurance premiums associated with ownership. At *Air Atlanta Helicopters*, the owner spends approximately \$21,000 per year to insure a new R-22 and \$16,000 per year for an older model. These high prices are a direct result of the R-22’s poor safety record as a training helicopter.

## 11 Safety Analysis and Aircraft Certification

In order to validate the Rambler’s preliminary design characteristics, consideration must be given to the vehicle’s overall safety rating and the certification requirements that it must satisfy. A safety analysis of the Rambler was conducted and a certification timeline was developed to demonstrate how this design proposal will show compliance with the Federal Aviation Regulations (FAR).

### 11.1 Safety Analysis

The first step in conducting a safety analysis is to develop an understanding of the system being analyzed and the mission it performs. This proposal represents the Rambler’s system description and Section 2, in particular, describes the mission requirements of a training helicopter. With this information established, a functional decomposition can be conducted.

#### 11.1.1 Functional Analysis

The purpose of functional analysis is to “transform the functional, performance, interface, and other requirements that were identified through requirements analysis into a coherent description of system functions.”<sup>45</sup> In Section 2.1, two training mission profiles are depicted which identify several functions the Rambler must perform. These functions were then decomposed through the use of a functional flow block diagram (FFBD). This analysis tool defines task sequences and relationships – identifying functional interactions within the system. The following figure shows a three-level functional decomposition for the Rambler.

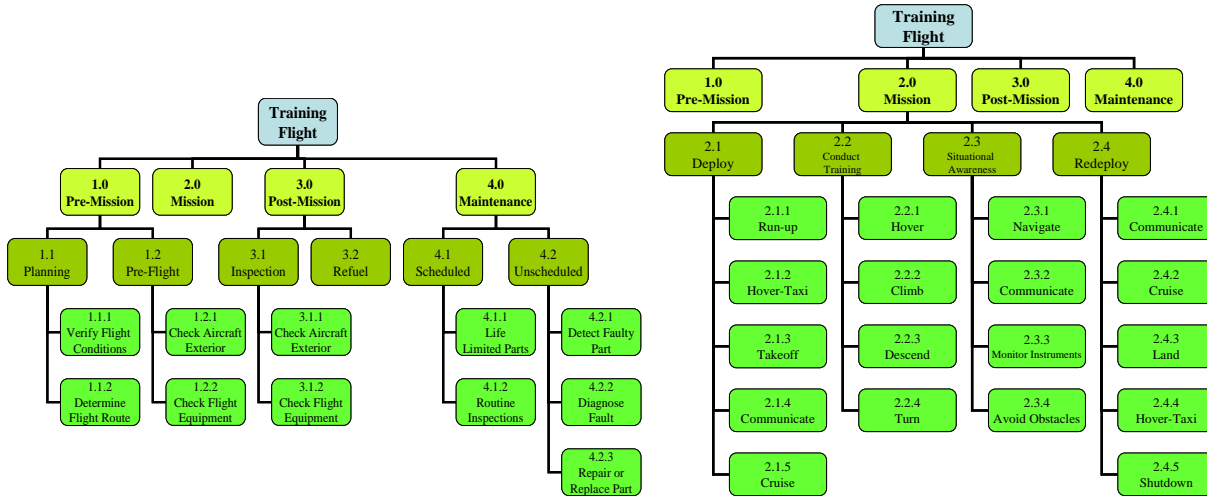


Figure 91: Functional Flow Block Diagrams

### 11.1.2 Functional Hazard Assessment

The Functional Hazard Assessment (FHA) is a systematic, comprehensive examination of functions to identify failure conditions and organize them according to their importance. It is a qualitative process which demonstrates each possible failure mode of the system and its corresponding effect on the aircraft, crew, and passengers. The objective of the Rambler’s FHA was to consider the potential failure modes associated with the airframe, powerplant, and human interaction functions and to classify the severity of their malfunctioning conditions as catastrophic, severe major, major, minor, or no safety effect. Figure 92 shows the catastrophic category for the Rambler’s FHA.

Failure Category	Failure Event	Flight Phase	FAA Safety Requirement
Airframe Catastrophic Failure	Loss of Flight Control	Take Off	FAILURE RATE LESS THAN 1.0E-10
		Cruise	
	Landing		
	Loss of Tail Rotor	Cruise	
Powerplant Catastrophic Failure	Engine Failure	Take Off	
		Landing	
	Transmission Failure	Take Off	
		Landing	
Human Interaction Catastrophic Failure	Failure to React to Engine Failure	Take Off	
		Landing	

Figure 92: Rambler FHA (Catastrophic)

### 11.1.3 Preliminary System Safety Assessment (PSSA)

A Preliminary System Safety Assessment (PSSA) is conducted in order to achieve compliance with FAA safety requirements. The inputs for this process are the failure modes identified in the FHA during the previous step. The objective of this step is to quantitatively determine the probabilities of

failure for primary aircraft systems according to the failure rates of each subsystem and component. The PSSA is generated through the use of various quantitative analytic tools, such as Fault Tree Analysis (FTA), Reliability Block Diagrams (RBD), Markov Analysis (MA), and Stochastic Petri Nets (SPN). Although FTA was conducted as part of the Rambler’s hub selection trade study, a detailed failure rate analysis for the entire vehicle design was beyond the scope of this proposal.

## ***11.2 Certification Plan***

The certification plan provides the necessary documentation to the Federal Aviation Administration (FAA) that a given design demonstrates compliance with all applicable regulations. The typical certification process involves five phases: conceptual design, requirements definition, compliance planning, implementation, and post certification. Common throughout this entire process is the Partnership for Safety Plan (PSP) - representing an “umbrella” agreement between the applicant and the FAA aimed at establishing the standard operating procedures and expectations of the certification process. In the first three stages of the process, the applicant then formulates a Project Specific Certification Plan (PSCP) that follows the guidelines of the PSP in order to address the unique certification characteristics of a particular new design. In the implementation and post certification phases, the required tests and evaluations are completed – providing the basis for continued airworthiness activities.<sup>46</sup>

The development of a complete Project Specific Certification Plan (PSCP) was beyond the scope of this project; however, a proposed certification timeline was created to identify the critical certification issues in the Rambler’s design. Two specific areas of this design proposal, the powerplant and the Hanson rotor system, were highlighted because they will require additional testing and evaluation in the certification process. Both design areas are required to meet the provisions of FAR Part 27, while the powerplant must also meet the standards presented in FAR Part 33. The following two lists provide an example of some of the major rotorcraft and powerplant tests conducted during certification:

<b>Rotorcraft Requirements</b>		<b>Engine Requirements</b>	
FAR 27.681	Limit load static tests	FAR 33.83	Vibration test
FAR 27.683	Operation tests	FAR 33.85	Calibration tests
FAR 27.723	Shock absorption tests	FAR 33.87	Endurance test
FAR 27.725	Limit drop tests	FAR 33.88	Engine over-temperature test
FAR 27.923	Rotor drive system and control tests	FAR 33.89	Operation test
FAR 27.965	Fuel tank tests	FAR 33.93	Teardown inspection
FAR 27.1015	Oil tank tests	FAR 33.94	Blade containment tests
FAR 27.1045	Cooling tests	FAR 33.99	General conduct of block tests

Based on the additional powerplant certification requirements, the new turbine engine design for the Rambler will precede the aircraft certification by approximately one year. The ground testing of Hanson rotor system can be conducted concurrently with the engine. Therefore, the two critical certification systems will be ready for installation tests on the Rambler after one year and a typical

rotorcraft certification timeline of three years will ensue. See Appendix B for the proposed certification timelines for the powerplant and rotorcraft, respectively.

## 12 Conclusion

Without question, there is a demand in today's aviation training market for an affordable two-place turbine helicopter and the Rambler satisfies this growing need. Through a commitment to simplicity in every aspect of the design, the Rambler demonstrates superior flight performance and improved safety characteristics at a very competitive price.

- At its “core” is the **Hanson “Ideal Rotor” System** which capitalizes on the use of composite materials to achieve unprecedented simplification in both form and function. The structural redundancy of its flexure design improves safety and reliability while eliminating the need for blade dampers and hydraulic augmentation. With 10% effective hinge offset, the Rambler also performs with much better handling qualities than those of a typical teetering hub system – giving both student and instructor pilots greater controllability in all modes of flight.
- A **new, low-cost turbine engine** provides the benefits of improved reliability and performance throughout a greater range of altitude and temperature conditions for a price aimed at bridging the financial gap between piston and turbine engines in today's market. The turboshaft/turboprop modular gearbox design drastically increases the unit's marketability by satisfying both fixed-wing and rotary-wing applications, and ultimately reduces production cost to a competitive level.
- The Rambler's **composite fuselage** offers the advantages of weight savings and reduced maintenance cost while achieving improved crashworthiness over traditional aluminum airframes.
- In addition to these product capabilities, the Rambler's design also integrated the use of **state-of-the-art CAD/CAM software** to better optimize the processes involved in vehicle development. By using simulation techniques to “prove out” manufacturing processes in a virtual environment without requiring the use of “real” equipment and personnel, tremendous savings can be realized in terms of time, capital, and resource efficiency.

Ultimately, this integrated approach of concurrent product and process development translates to greater customer satisfaction by simultaneously increasing product quality and reducing product cost. Every aspect of the Rambler's design is intended to achieve this goal – turbine engine performance at a piston engine price.



## APPENDIX A – Group Weight Statement

The MIL-STD-1374 Group Weight Statement is presented below. This is the complete estimated weight breakdown of the final configuration of the preliminary design.

**Table 20: MIL-STD-1374 Group Weight Statement**

MIL-STD-1374 PART 1-TAB		GROUP WEIGHT STATEMENT				PAGE	1
NAME: GA TECH		WEIGHT EMPTY				MODEL	RAMBLER
DATE: MAY 2006						REPORT	
1	ROTOR GROUP						101.4
2	BLADE MASS					68.0	
3	HUB AND HINGE					33.4	
4							
5	TAIL ROTOR GROUP						9.8
6	TAIL ROTOR					4.5	
7	HORIZONTAL STABILIZER					1.7	
8	VERTICAL STABILIZER					3.6	
9							
10	FUSELAGE						198.5
11							
12	LANDING GEAR						103.5
13							
14	PROPULSION GROUP					158.0	
15	ENGINE INSTALLATION						120.0
16	PROPULSION SUBSYSTEM						33.7
17	FUEL SYSTEM						4.3
18							
19	DRIVE SYSTEM						85.0
20							
21	FLIGHT CONTROL GROUP					53.1	
22	COCKPIT CONTROL						13.0
23	SYSTEM CONTROL						10.2
24	AVIONICS						30.0
25							
26	INSTRUMENT GROUP						5.2
27							
28	ELECTRICAL						60.0
29							
30							
31	FURNISHINGS & EQUIPMENT GROUP					19.7	
32	FURNISHINGS AND EQUIPMENT						8.9
33	AIR COND. & ANTI-ICE						10.8
34							
35	MANUFACTURING VARIATION						5.4
36							
37	<b>TOTAL WEIGHT EMPTY</b>						<b>799.7</b>
38	CREW (NO. 1)						170.0
39	PASSENGER (NO. 1)						170.0
40	FUEL						114.0
41	UNUSABLE FUEL					1.5	
42	AVAILABLE MISSION FUEL					112.5	
43	BAGGAGE						100.0
44							
45	TOTAL USEFUL LOAD						554.0
46							
47	<b>GROSS WEIGHT</b>						<b>1353.7</b>

## APPENDIX B – Recurring Cost Breakdown

Table 21: Rambler Recurring Cost Breakdown (\$2006)

Total Average Cost by System				
	Labor	Material	Subcontract	Total
<b>Main Rotor</b>	<b>\$4,100</b>	<b>\$11,359</b>	<b>\$9,288</b>	<b>\$24,747</b>
Hub	\$1,436	\$1,584	\$6,376	\$9,395
Blades	\$2,665	\$9,775	\$2,912	\$15,352
<b>Tail Rotor</b>	<b>\$778</b>	<b>\$1,414</b>	<b>\$1,113</b>	<b>\$3,305</b>
Vertical Stabilizer	\$321	\$304	\$98	\$723
Horizontal Stabilizer	\$149	\$291	\$0	\$440
Blades	\$308	\$819	\$1,015	\$2,142
<b>Fuselage</b>	<b>\$7,442</b>	<b>\$11,080</b>	<b>\$1,922</b>	<b>\$20,444</b>
Basic Structure	\$6,426	\$10,196	\$1,922	\$18,544
Tailboom	\$1,017	\$884	\$0	\$1,900
<b>Landing Gear</b>	<b>\$1,168</b>	<b>\$960</b>	<b>\$792</b>	<b>\$2,920</b>
<b>Nacelles</b>	<b>\$1,620</b>	<b>\$1,989</b>	<b>\$102</b>	<b>\$3,711</b>
Firewall	\$355	\$490	\$67	\$912
Cowling	\$1,134	\$1,173	\$20	\$2,327
Engine Mounts	\$131	\$326	\$15	\$471
<b>Air Induction</b>	<b>\$92</b>	<b>\$232</b>	<b>\$617</b>	<b>\$941</b>
Air Inlet	\$44	\$28	\$8	\$80
Air Filtration	\$48	\$204	\$610	\$862
<b>Powerplant</b>	<b>\$171</b>	<b>\$7,475</b>	<b>\$77,478</b>	<b>\$56,735</b>
Engine	\$0	\$0	\$70,920	\$42,530
Engine Installation	\$77	\$1,648	\$5,212	\$6,937
Lubrication System	\$46	\$1,612	\$357	\$2,015
Fuel System	\$48	\$4,215	\$990	\$5,252
<b>Drive System</b>	<b>\$4,712</b>	<b>\$8,502</b>	<b>\$10,004</b>	<b>\$23,218</b>
Main Transmission	\$1,712	\$4,594	\$3,484	\$9,790
Tailrotor Gearbox	\$645	\$322	\$1,245	\$2,212
Freewheeling Unit	\$497	\$1,140	\$527	\$2,165
Engine Input Shaft	\$944	\$105	\$219	\$1,268
Tailrotor Driveshaft	\$421	\$1,534	\$294	\$2,249
Accessory Gearbox	\$492	\$807	\$4,235	\$5,534
<b>Flight Controls</b>	<b>\$439</b>	<b>\$9,011</b>	<b>\$5,626</b>	<b>\$15,076</b>
Cockpit controls	\$132	\$3,693	\$4,401	\$8,226
Non-rotating	\$92	\$3,836	\$419	\$4,346
Rotating - main rotor	\$80	\$1,383	\$605	\$2,068
Rotating - tail rotor	\$135	\$99	\$202	\$435
<b>Instruments</b>	<b>\$189</b>	<b>\$31</b>	<b>\$8,606</b>	<b>\$8,826</b>
<b>Electrical</b>	<b>\$723</b>	<b>\$1,909</b>	<b>\$3,278</b>	<b>\$5,910</b>
<b>Avionics</b>	<b>\$598</b>	<b>\$195</b>	<b>\$7,788</b>	<b>\$8,581</b>
<b>Furnishings and Equipment</b>	<b>\$827</b>	<b>\$3,313</b>	<b>\$826</b>	<b>\$4,965</b>
Crew Seats	\$336	\$476	\$300	\$1,112
Fire Extinguishing	\$34	\$564	\$176	\$774
Soundproofing	\$0	\$0	\$294	\$294
Misc Furnishings	\$457	\$2,273	\$56	\$2,786
<b>Anti-icing</b>	<b>\$11</b>	<b>\$0</b>	<b>\$17,971</b>	<b>\$17,982</b>
<b>Load and Handling</b>	<b>\$10</b>	<b>\$996</b>	<b>\$0</b>	<b>\$1,006</b>
<b>Final Assembly</b>	<b>\$2,208</b>	<b>\$0</b>	<b>\$0</b>	<b>\$2,208</b>
<b>Totals</b>	<b>\$25,088</b>	<b>\$58,466</b>	<b>\$145,412</b>	<b>\$200,576</b>

# APPENDIX C – Certification Timeline

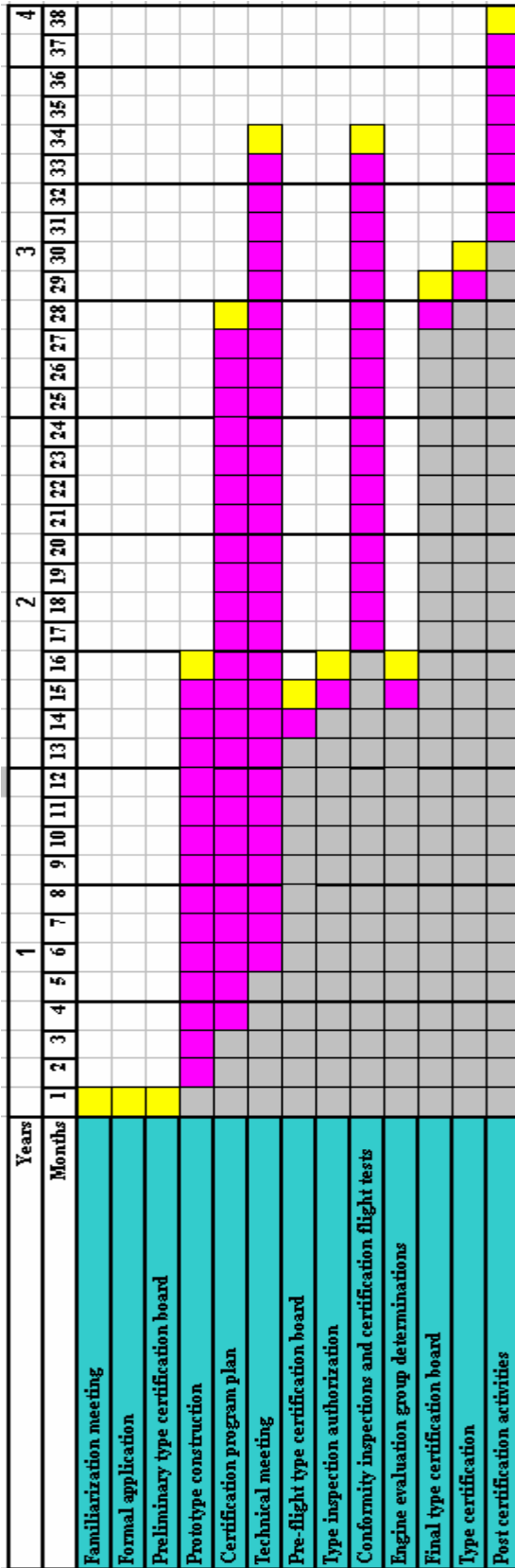


Figure 93: Powerplant Certification Schedule

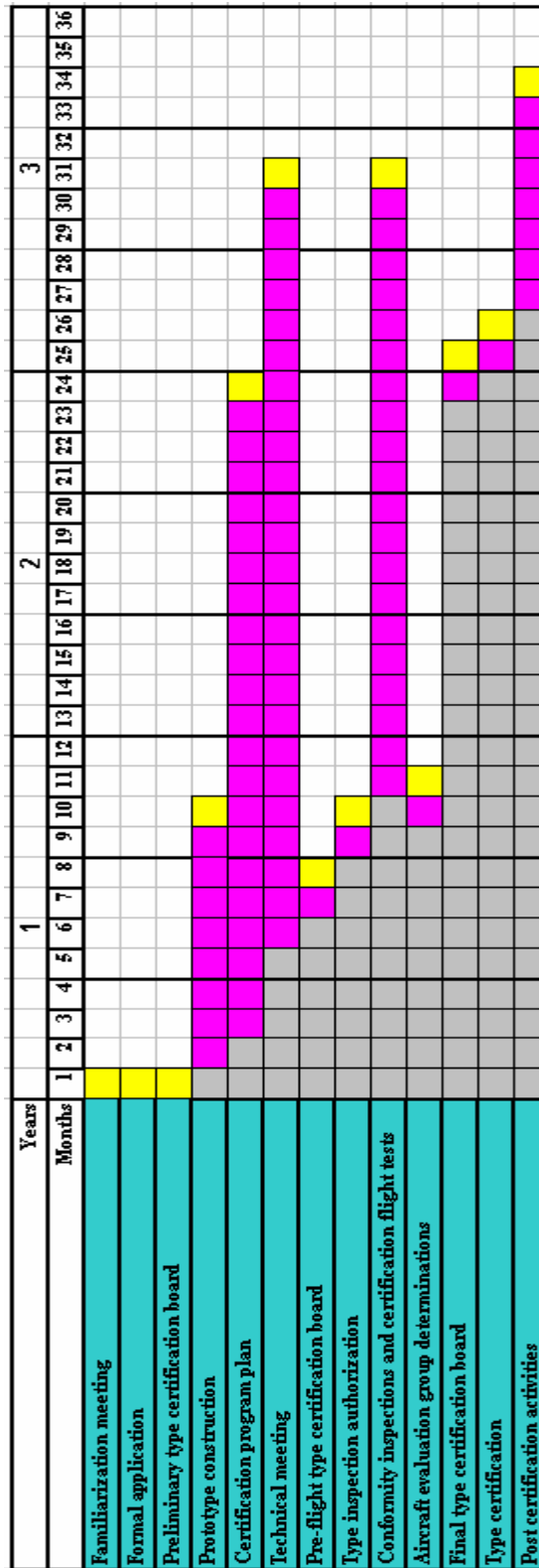


Figure 94: Aircraft Certification Schedule



---

## References

---

- <sup>1</sup> Hanson, Thomas F. *A Designer Friendly Handbook of Helicopter Rotor Hubs*, 1998.
- <sup>2</sup> Schrage, Daniel P. *Istanbul Technical University-Light Commercial Helicopter Dynamic Analysis of Rotor System Using Dymore*. Georgia Institute of Technology, 2006.
- <sup>3</sup> Schrage, Daniel P., *AE6333 Rotorcraft Design I: Individual and Team Projects*, 2005.
- <sup>4</sup> Kundu, A. K. et al., "Aircraft Component Manufacture Case Studies and Operating Cost Reduction Benefit," AIAA 2003-6829, 2003.
- <sup>5</sup> 23<sup>rd</sup> Annual Student Design Competition, Request for Proposals, "2-Place Turbine Training Helicopter", sponsored by AHS International, Inc. and Bell Helicopter, Inc., 2006.
- <sup>6</sup> Interview conducted with Mr. Blake Moore, Air Atlanta Helicopters, Inc. March 2006.
- <sup>7</sup> Schrage, Daniel P., "Extension of RF Method to VTOL Aircraft Conceptual and Preliminary Design", *AE6333 Rotorcraft Design I Course Notes*, Georgia Institute of Technology, Fall Semester, 2005.
- <sup>8</sup> Prouty, Raymond W. *Helicopter Performance, Stability and Control*. FL: Kreiger, 1995.
- <sup>9</sup> *JVX Technology Assessment*, Appendix D – General Parasite Drag Methodology, 1984.
- <sup>10</sup> PC Based Development, *Recurring Production and Operating and Support Cost Model User's Guide*, 2001.
- <sup>11</sup> Leishman, J. Gordon., *Principles of Helicopter Aerodynamics*, Cambridge University Press, New York, 2000.
- <sup>12</sup> <http://www.flightlab.com>.
- <sup>13</sup> Tapavicza, M. and Och, F., "Application of Damage Tolerance Concepts for MBB Helicopters", AGARD Conference Proceedings No. 297.
- <sup>14</sup> Hanson, Thomas F., "The Auto-Trim Rotor Stability System," AHS Annual Forum, 1997.
- <sup>15</sup> Leyes, Richard A., and Fleming, William A., *The History of North American Small Gas Turbine Aircraft Engines*. Virginia: AIAA, 1999.
- <sup>16</sup> Benstein, Eli H., "Small Flying Engines Are Different," *American Institute of Aeronautics and Astronautics Paper 74-1185*, 1974.
- <sup>17</sup> *Aviation Week and Space Technology*, (January 17, 2005).
- <sup>18</sup> Mattingly, Jack D., Heiser, William H., and Pratt, Daniel T., *Aircraft Engine Design*. 2<sup>nd</sup> ed. Virginia: AIAA, 2002.
- <sup>19</sup> *AMCP 706-201 Engineering Design Handbook*, "Helicopter Engineering: Part One – Preliminary Design," US Army Materiel Command, 1974.
- <sup>20</sup> Gauntner, James W., "Algorithm for Calculating Turbine Cooling Flow and the Resulting Decrease in Turbine Efficiency," *NASA Technical Memorandum 81453*, (Cleveland, OH: Lewis Research Center, 1980).
- <sup>21</sup> Clifford, R.J. "Rotating Heat Transfer Investigations on a Multipass Cooling Geometry," *AGARD CP 390*, 1985.
- <sup>22</sup> NEPP User's Manual, 1997.
- <sup>23</sup> Japikse, David, and Baines, N.C., *Introduction to Turbomachinery*. Norwich, VT: Concepts ETI, 1994.
- <sup>24</sup> "NASA Extended Parametric Representation of Compressor Fans and Turbines," *NASA CR-174646*, Vol. II, General Electric: Cincinnati, OH, 1984.
- <sup>25</sup> Agrawal, M. D. and Bharani, S.. "Performance Evaluation of a Reverse-Flow Gas Turbine Combustor Using Modified Hydraulic Analogy," *IE Journal*. Vol. 85. 2004.
- <sup>26</sup> Bellocchio, Andrew T. "Drive System Design for a Single Main Rotor Heavy Lift Helicopter," *Masters Thesis Submitted at Georgia Institute of Technology*, 2005.
- <sup>27</sup> <http://www.navygouge.com>
- <sup>28</sup> Langston, Lee S., "Crown Jewels," *Mechanical Engineering Magazine*, 2006.
- <sup>29</sup> Donaldson, Peter. "Power is Control," *Helicopter World* (February 1998).
- <sup>30</sup> <http://www.afsfilters.com>.

- 
- <sup>31</sup> PC Based Development, *Recurring Production and Operating and Support Cost Model User's Guide*, 2001.
- <sup>32</sup> Jackson, K. and Fasnaella, E., “*Crashworthy Evaluation of a 1/5 Scale Model Composite Fuselage Section*”, NASA/TM-1999-209132 ARL-MR-441, Vehicle Technology Center, Langley Research Center (LARC), Hampton, VA, 1999.
- <sup>33</sup> Olcott, Dennis D., “Adam Aircraft A500 and A700 Development,” *AIAA Presentation*, Atlanta, GA, 2006.
- <sup>34</sup> Tho, C., Sparks C, Smith, Sareen A., and Johnson, C., “*Efficient Helicopter Skid Landing Gear Dynamic Drop Simulation Using LS-DYNA*,” Bell Helicopter Textron and NAVAIR, American Helicopter Society (AHS) 59th Annual Forum, Phoenix, AZ, May 6-8, 2003.
- <sup>35</sup> Johnson, Wayne. *Helicopter Theory*. New York: Dover, 1980.
- <sup>36</sup> *AE 6503 Helicopter Stability and Control Course Notes*, Georgia Institute of Technology, Spring Semester, 2006.
- <sup>37</sup> *AE 6070 Rotary Wing Aerodynamics Course Notes*, Georgia Institute of Technology, Fall Semester, 2005.
- <sup>38</sup> Rysdyk, Rolf T. and Calise, Anthony J., “Nonlinear Adaptive Flight Control Using Neural Networks,” *IEEE Controls Systems Magazine*, 18 (6):14-25, December 1998.
- <sup>39</sup> Johnson, E.N. and Mishra, S.S., Flight Simulation for the Development of an Experimental UAV, Proceedings of the AIAA Modeling and Simulation Technologies Conference, 2002.
- <sup>40</sup> Schrage, Daniel P. et al., “Application of Software Enabled Control Technologies to a Full-Scale Unmanned Helicopter,” AIAA Atmospheric Flight Mechanics Conference and Exhibit, San Francisco, CA, 15-18 August 2005.
- <sup>41</sup> <http://www.bluemountainavionics.com/>
- <sup>42</sup> “Power to Plan is Power to Build” Presentation, Dassault Systemes, 2006.
- <sup>43</sup> CIMdata, “The Benefits of Digital Engineering,” 2003.
- <sup>44</sup> US Department of Labor, Bureau of Labor Statistics, *Inflation Calculator*, <http://data.bls.gov/cgi-bin/cpicalc.pl>
- <sup>45</sup> *Systems Engineering Fundamentals*, Defense Acquisition University, Fort Belvoir, VA, January 2001.
- <sup>46</sup> *The FAA and Industry Guide to Product Certification*, 2nd Ed, 2004.